



**ROTATIONAL TEMPERATURE AND NUMBER DENSITY MEASUREMENTS  
OF  $N_2$ ,  $O_2$ , CO, AND  $CO_2$  IN A HYPERSONIC FLOW  
FIELD USING LASER-RAMAN SPECTROSCOPY**

**VON KÁRMÁN GAS DYNAMICS FACILITY  
ARNOLD ENGINEERING DEVELOPMENT CENTER  
AIR FORCE SYSTEMS COMMAND  
ARNOLD AIR FORCE STATION, TENNESSEE 37389**

**July 1975**

**Final Report for Period May 1 — November 1, 1973**

Approved for public release; distribution unlimited.

**PROPERTY OF U.S. AIR FORCE  
AEDC TECHNICAL LIBRARY  
ARNOLD AFB, TN 37339**

**Prepared for**

**DIRECTORATE OF TECHNOLOGY  
ARNOLD ENGINEERING DEVELOPMENT CENTER  
ARNOLD AIR FORCE STATION, TENNESSEE 37389**

## NOTICES

When U. S. Government drawings specifications, or other data are used for any purpose other than a definitely related Government procurement operation, the Government thereby incurs no responsibility nor any obligation whatsoever, and the fact that the Government may have formulated, furnished, or in any way supplied the said drawings, specifications, or other data, is not to be regarded by implication or otherwise, or in any manner licensing the holder or any other person or corporation, or conveying any rights or permission to manufacture, use, or sell any patented invention that may in any way be related thereto.

Qualified users may obtain copies of this report from the Defense Documentation Center.

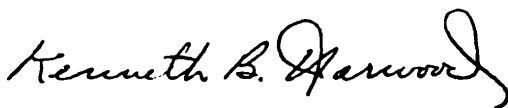
References to named commercial products in this report are not to be considered in any sense as an endorsement of the product by the United States Air Force or the Government.

This report has been reviewed by the Information Office (OI) and is releasable to the National Technical Information Service (NTIS). At NTIS, it will be available to the general public, including foreign nations.

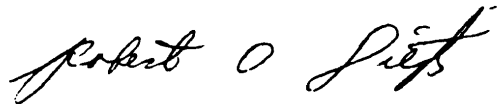
## APPROVAL STATEMENT

This technical report has been reviewed and is approved for publication.

FOR THE COMMANDER



KENNETH B. HARWOOD  
Captain, CF  
Research & Development  
Division  
Directorate of Technology



ROBERT O. DIETZ  
Director of Technology

# UNCLASSIFIED

REPORT DOCUMENTATION PAGE		READ INSTRUCTIONS BEFORE COMPLETING FORM
1. REPORT NUMBER <b>AEDC-TR-75-37</b>	2. GOVT ACCESSION NO.	3. RECIPIENT'S CATALOG NUMBER
4. TITLE (and Subtitle) <b>ROTATIONAL TEMPERATURE AND NUMBER DENSITY MEASUREMENTS OF N<sub>2</sub>, O<sub>2</sub>, CO, AND CO<sub>2</sub> IN A HYPERSONIC FLOW FIELD USING LASER-RAMAN SPECTROSCOPY</b>	5. TYPE OF REPORT & PERIOD COVERED <b>Final Report - May 1 to November 1, 1973</b>	
	6. PERFORMING ORG. REPORT NUMBER	
7. AUTHOR(s) <b>W. D. Williams and J. W. L. Lewis, ARO, Inc.</b>	8. CONTRACT OR GRANT NUMBER(s)	
9. PERFORMING ORGANIZATION NAME AND ADDRESS <b>Arnold Engineering Development Center (DY) Arnold Air Force Station, Tennessee 37389</b>	10. PROGRAM ELEMENT, PROJECT, TASK AREA & WORK UNIT NUMBERS <b>Program Element 65802F</b>	
11. CONTROLLING OFFICE NAME AND ADDRESS <b>Arnold Engineering Development Center (DYFS) Arnold Air Force Station Tennessee 37389</b>	12. REPORT DATE <b>July 1975</b>	
	13. NUMBER OF PAGES <b>89</b>	
14. MONITORING AGENCY NAME & ADDRESS (if different from Controlling Office)	15. SECURITY CLASS. (of this report)  <b>UNCLASSIFIED</b>	
	15a. DECLASSIFICATION DOWNGRADING SCHEDULE <b>N/A</b>	
16. DISTRIBUTION STATEMENT (of this Report)  <b>Approved for public release; distribution unlimited.</b>		
17. DISTRIBUTION STATEMENT (of the abstract entered in Block 20, if different from Report)		
18. SUPPLEMENTARY NOTES  <b>Available in DDC</b>		
19. KEY WORDS (Continue on reverse side if necessary and identify by block number) <div style="display: flex; justify-content: space-between;"> <div> condensation Raman scattering numerical analysis orifice flow </div> <div> rotational temperature number density conical nozzle measurement </div> <div> laser gases </div> </div>		
20. ABSTRACT (Continue on reverse side if necessary and identify by block number) <p>After successful laboratory measurements of the rotational temperature <math>T_R</math> of N<sub>2</sub>, O<sub>2</sub>, CO, and CO<sub>2</sub> at atmospheric pressure and room temperature and of N<sub>2</sub> at 296, 215, and 163 K at an equivalent room temperature pressure of 10 torr, measurements of the rotational temperature of these gases were made in the hypersonic flow field produced by either a sonic orifice or a conical nozzle expansion. The throat diameter of the source was varied between</p>		

# UNCLASSIFIED

## UNCLASSIFIED

### ABSTRACT (Continued)

1.04 and 1.325 mm. Axial variation of  $T_R$  was determined for both flow generators over a range of reservoir pressures (0.7 to 10 atm) with a nominal reservoir temperature of 285 K. Agreement with the Ashkenas-Sherman (Ref. 8) calculations of free-stream temperature of  $N_2$ ,  $O_2$ , and CO for a sonic orifice expansion was excellent as was the agreement with method of characteristics (MOC) calculations for the nozzle flow field. Radial profile measurements of  $T_R$  were performed at two axial positions for the  $N_2$  nozzle flow field at a reservoir pressure of 10 atm. The sonic orifice expansion results for rotational temperature of  $CO_2$  for the axial region  $X/D < 4$  displayed no agreement with the Ashkenas-Sherman (Ref. 8) results for  $\gamma = 7/5$  and  $5/3$ , and no theory exists in this region for  $\gamma = 9/7$ . Agreement was obtained with the electron beam results of Beylich (Ref. 11) using appropriate reservoir scaling laws. The axial variation of  $N_2$  number density was determined for the nozzle source over a range of reservoir pressures (3.3 to 10 atm), and radial profiles at two axial locations were determined for the 10-atm condition. Agreement with the MOC calculations was excellent. The minimum number densities at which measurements were made were  $2.31 \times 10^{16} \text{ cm}^{-3}$  for  $N_2$ ,  $4.54 \times 10^{16} \text{ cm}^{-3}$  for  $O_2$ ,  $1.34 \times 10^{17} \text{ cm}^{-3}$  for CO, and  $7.97 \times 10^{16} \text{ cm}^{-3}$  for  $CO_2$ . With improvements in the optical system and increased laser power, these limits could be decreased by nearly three orders of magnitude.

UNCLASSIFIED

## PREFACE

The work reported herein was conducted by the Arnold Engineering Development Center (AEDC), Air Force Systems Command (AFSC), Arnold Air Force Station, Tennessee, under Program Element 65802F. This project was monitored by Major Maurice Clermont. The results were obtained by ARO, Inc. (a subsidiary of Sverdrup & Parcel and Associates, Inc.), contract operator of AEDC, AFSC. The work was done under ARO Projects No. VF452 and V32S-37A. The authors of this report were W. D. Williams and J. W. L. Lewis, ARO, Inc. The manuscript (ARO Control No. ARO-VKF-TR-74-93) was submitted for publication on September 30, 1974.

## CONTENTS

	<u>Page</u>
1.0 INTRODUCTION	
1.1 Free-Stream Diagnostics . . . . .	9
1.2 Intensity Equations . . . . .	12
2.0 EXPERIMENTAL APPARATUS	
2.1 Laboratory System . . . . .	22
2.2 Research Chamber System . . . . .	26
3.0 MEASUREMENTS	
3.1 Laboratory Measurements . . . . .	30
3.2 Flow-Field Measurements . . . . .	38
4.0 ANALYSIS AND DISCUSSION	
4.1 Molecular Partition Functions . . . . .	56
4.2 Condensation, Relaxation, and Their Effects . . . . .	60
5.0 SUMMARY AND RECOMMENDATIONS FOR FUTURE WORK	
5.1 Review of Measurements . . . . .	71
5.2 Systems Improvements . . . . .	72
5.3 Future Work . . . . .	73
REFERENCES . . . . .	74

## ILLUSTRATIONS

### Figure

1. Partial Rotational Energy Level Diagram Depicting Transitions Resulting in the Pure Rotational Raman Spectra and the Rayleigh Line . . . . .	10
2. Calculated Pure Rotational Raman Spectra of Nitrogen at a Temperature of 300 K . . . . .	11
3. Calculated Stokes Band Pure Rotational Raman Spectra of Nitrogen and Oxygen in Air at a Temperature of 50 K . . . . .	11
4. Schematic of Laboratory Experimental Arrangement . . . . .	23
5. Schematic of Collection and Spectrometer Optics . . . . .	24
6. Spectral Response Curve of EMI-9502B Photomultiplier. . . . .	25

<u>Figure</u>	<u>Page</u>
7. Voltage Divider Network of EMI-9502B Photo-multiplier . . . . .	25
8. Block Diagram of Photon Counting System . . . . .	26
9. Schematic of 4- by 10-ft Research Chamber Experimental Arrangement . . . . .	27
10. Schematic of 4- by 10-ft Research Chamber . . . . .	27
11. Schematic of Sonic Orifice . . . . .	28
12. Schematic of Conical Nozzle . . . . .	28
13. Schematic of 4- by 10-ft Research Chamber Gas Inbleed System . . . . .	29
14. Pure Rotational Raman Spectrum of Nitrogen at Atmospheric Pressure and Room Temperature . . . . .	31
15. Boltzmann Plot of Pure Rotational Raman Line Intensities from Fig. 14 . . . . .	31
16. Pure Rotational Raman Spectrum of Nitrogen at Atmospheric Pressure and Room Temperature . . . . .	32
17. Boltzmann Plot of Pure Rotational Raman Line Intensities from Fig. 16 . . . . .	32
18. Pure Rotational Raman Spectrum of Nitrogen at 10-torr Pressure and Room Temperature . . . . .	33
19. Boltzmann Plot of Pure Rotational Raman Line Intensities from Fig. 18 . . . . .	33
20. Pure Rotational Raman Spectrum of Nitrogen at an Equivalent Room Temperature Pressure of 10 torr and a Temperature of 163 K . . . . .	34
21. Boltzmann Plot of Pure Rotational Raman Line Intensities from Fig. 20 . . . . .	34
22. Pure Rotational Raman Spectrum of Oxygen at Atmospheric Pressure and Room Temperature . . . . .	35
23. Boltzmann Plot of Pure Rotational Raman Line Intensities from Fig. 22 . . . . .	35

<u>Figure</u>	<u>Page</u>
24. Pure Rotational Raman Spectrum of Carbon Dioxide at Atmospheric Pressure and Room Temperature . . . . .	36
25. Boltzmann Plot of Pure Rotational Raman Line Intensities from Fig. 24 . . . . .	36
26. Pure Rotational Raman Spectrum of Carbon Monoxide at Atmospheric Pressure and Room Temperature . . . . .	37
27. Boltzmann Plot of Pure Rotational Raman Line Intensities from Fig. 26 . . . . .	37
28. Typical Low Temperature Pure Rotational Raman Spectrum of Nitrogen in a Hypersonic Flow . . . . .	39
29. Boltzmann Plot of Pure Rotational Raman Line Intensities from Fig. 28 . . . . .	39
30. Axial Variation of $T_R/T_O$ for a Free-Jet Nitrogen Flow with $P_O = 2.79$ atm . . . . .	40
31. Axial Variation of $T_R/T_O$ for a Free-Jet Nitrogen Flow with $P_O = 3.72$ atm . . . . .	41
32. Axial Variation of $T_R/T_O$ for a Free-Jet Nitrogen Flow with $P_O = 5.58$ atm . . . . .	42
33. Axial Variation of $T_R/T_O$ for a Free-Jet Nitrogen Flow with $P_O = 7.44$ atm . . . . .	43
34. Typical Low Temperature Pure Rotational Raman Spectrum of Carbon Monoxide in a Hypersonic Flow . . . . .	45
35. Typical Low Temperature Pure Rotational Raman Spectrum of Oxygen in a Hypersonic Flow . . . . .	45
36. Axial Variation of $T_R/T_O$ for a Free-Jet Carbon Monoxide Flow with $P_O = 3.72$ atm . . . . .	46
37. Axial Variation of $T_R/T_O$ for a Free-Jet Oxygen Flow with $P_O = 3.72$ atm . . . . .	46
38. Typical Low Temperature Pure Rotational Raman Spectrum of Carbon Dioxide in a Hypersonic Flow . . . . .	47
39. Boltzmann Plot of Pure Rotational Raman Line Intensities from Fig. 38 . . . . .	47



<u>Figure</u>	<u>Page</u>
40. Axial Variation of $T_R/T_O$ for a Free-Jet Carbon Dioxide Flow with $P_O = 0.70$ atm . . . . .	48
41. Axial Variation of $T_R/T_O$ for a Conical Nozzle Nitrogen Flow with $P_O = 3.40$ atm . . . . .	49
42. Axial Variation of $\rho/\rho_O$ for a Conical Nozzle Nitrogen Flow with $P_O = 3.40$ atm . . . . .	50
43. Axial Variation of $T_R/T_O$ for a Conical Nozzle Nitrogen Flow with $P_O = 6.80$ atm . . . . .	51
44. Axial Variation of $\rho/\rho_O$ for a Conical Nozzle Nitrogen Flow with $P_O = 6.80$ atm . . . . .	52
45. Axial Variation of $T_R/T_O$ for a Conical Nozzle Nitrogen Flow with $P_O = 10.2$ atm . . . . .	53
46. Axial Variation of $\rho/\rho_O$ for a Conical Nozzle Nitrogen Flow with $P_O = 10.2$ atm . . . . .	54
47. Radial Variation of $T_R/T_O$ at $X_t/D_t = 19.79$ for a Conical Nozzle Nitrogen Flow with $P_O = 10.2$ atm . . . . .	54
48. Radial Variation of $\rho/\rho_O$ at $X_t/D_t = 19.79$ for a Conical Nozzle Nitrogen Flow with $P_O = 10.2$ atm . . . . .	55
49. Radial Variation of $T_R/T_O$ at $X_t/D_t = 12.47$ for a Conical Nozzle Nitrogen Flow with $P_O = 10.2$ atm . . . . .	55
50. Radial Variation of $\rho/\rho_O$ at $X_t/D_t = 12.47$ for a Conical Nozzle Nitrogen Flow with $P_O = 10.2$ atm . . . . .	55
51. Temperature Variation of the Ratio $Q_{EO}$ . . . . .	59
52. Diagram of Expansion Process in P-T Plane . . . . .	60
53. CO <sub>2</sub> Rayleigh Scattering in the N-T Plane, $\gamma = 1.44$ . . . . .	62
54. Axial Variation of Mach Number for CO <sub>2</sub> . . . . .	63
55. Variation of $\gamma$ with Temperature for CO <sub>2</sub> . . . . .	64
56. Axial Variation of Number Density for $\gamma = 1.4$ (N <sub>2</sub> ) . . . . .	66
57. Axial Variation of Mach Number for $\gamma = 1.4$ (N <sub>2</sub> ) . . . . .	66
58. Axial Variation of Collision Number Integrand, $I_M$ , and Accumulative Collision Number Function, $\bar{Z}_T(12)$ , $\gamma = 1.4$ (N <sub>2</sub> ). . . . .	67

<u>Figure</u>	<u>Page</u>
59. Two-Dimensional Axial-Radial Locus of the Expansion Characteristic . . . . .	69
60. Ratio of the Unit Length Reynolds Number ( $Re_x$ ) and Mach Number (M) as a Function of Radial Position . . .	70
61. Optical System Improvements	
a. Modification One . . . . .	73
b. Modification Two . . . . .	73

### TABLES

1. Molecular Spectroscopic Values . . . . .	14
2. PROGRAM RATROT . . . . .	15
3. PROGRAM NUMRHO . . . . .	20
4. Summary of Measurements . . . . .	71

### APPENDIXES

A. DETAILS OF TEMPERATURE DETERMINATION . . . . .	77
B. OPTIMUM ILLUMINATION GEOMETRY FOR RAMAN SCATTERING MEASUREMENTS . . . . .	83
NOMENCLATURE . . . . .	86

## 1.0 INTRODUCTION

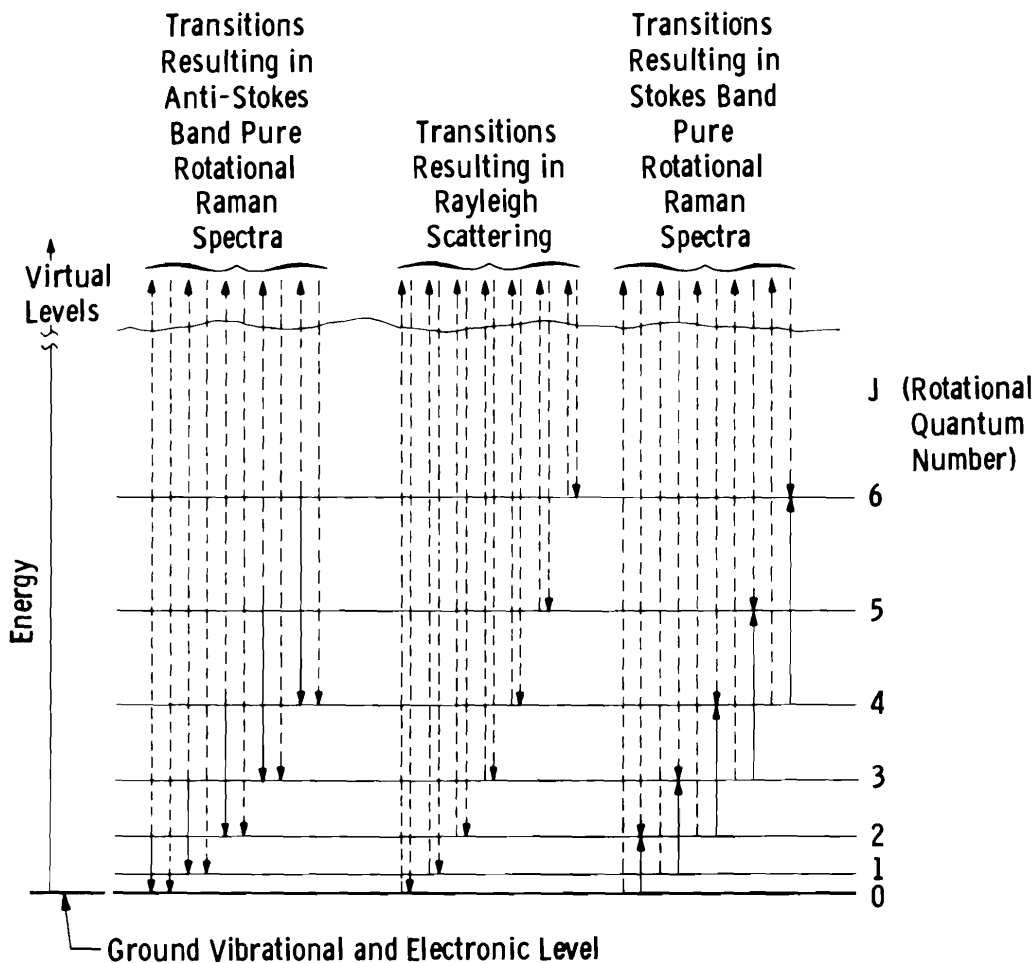
### 1.1 FREE-STREAM DIAGNOSTICS

There is a continuing need for the noninterfering measurement of both static gas temperature and number density in the high-speed flow fields associated with aerospace ground test facilities. Specifically, there are immediate applications for static temperature and density measurements in free-stream tunnel flows, for the studies of shock structure, boundary layers, wakes, turbulent flow fields, condensation phenomena, and for rocket exhaust plume diagnostics.

The well-known electron beam fluorescence technique, which is capable of determining these parameters (Ref. 1), has a density domain of applicability of approximately  $10^{13}$  to  $10^{17}$  molecules/cm<sup>3</sup>. The electron beam technique is density limited for the following reasons: (1) collisional quenching effects on the measurements increase with density, (2) the spatial resolution of the measurement decreases with increasing density, and (3) the secondary electron effects on the measurements increase with increasing density; all of which result in a decrease in accuracy of the measurement with increasing density. Therefore, for flow fields with densities greater than  $10^{17}$  molecules/cm<sup>3</sup>, static gas temperature and density measurements are most difficult. Laser-Raman spectroscopy, however, provides a technique for static temperature and density measurements which is similar to the electron beam technique in that the measurement is local and nonperturbing and possesses molecular specificity. However, Raman spectroscopy is not susceptible to the density limitations because the intermolecular collision time typically exceeds the photon-molecule scattering interaction time by several orders of magnitude.

Complete reviews of Raman scattering theory may be found in Refs. 2 through 5, and consequently, only a brief general discussion of Raman scattering will be undertaken here. Consider an incident laser beam to consist of photons of energy  $h\nu_0$ . On collision with a molecule, the photons may be elastically scattered, a process which results in no change in the molecular internal energy states, and the scattered radiation is designated as Rayleigh scattering. Inelastic collisions, however, may cause the molecule to undergo a quantum transition to a higher internal mode energy level, with the result that the photon loses energy and is scattered with lower frequency (longer wavelength). The encounter with the photon may also cause the molecule to undergo a transition to a

lower internal mode energy level, in which case the photon is scattered with increased frequency (shorter wavelength). Figure 1 schematically depicts the transitions occurring in a molecule for Rayleigh and pure rotational Raman scattering, and Figs. 2 and 3 depict a typical scattered light spectrum that might be observed as a result of the depicted transitions. The displacements of lower frequency have historically been referred to as the "Stokes lines," while the displacements of higher frequency have been called the "anti-Stokes lines."



Solid Vertical Lines Indicate Actual Rotational Level Transition

Figure 1. Partial rotational energy level diagram depicting transitions resulting in the pure rotational Raman spectra and the Rayleigh line.

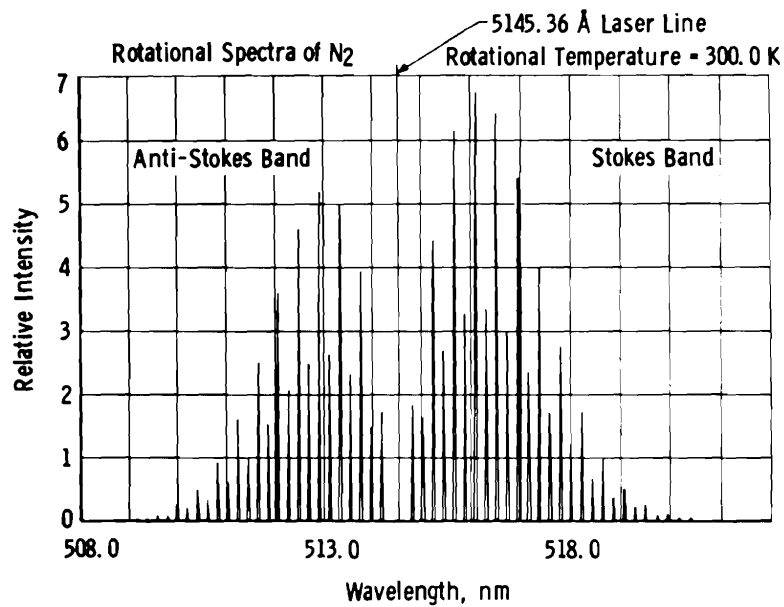


**Figure 2.** Calculated pure rotational Raman spectra of nitrogen at a temperature of 300 K.

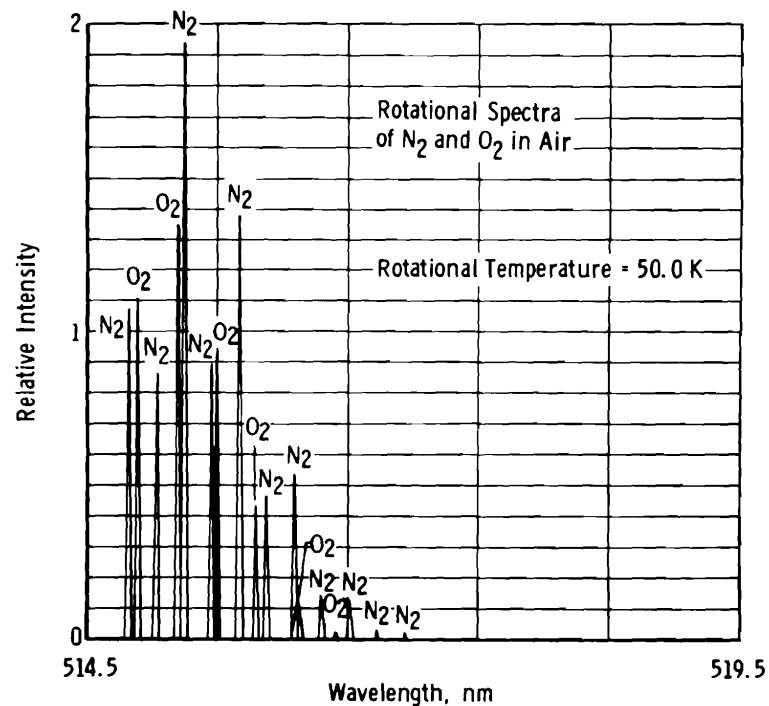


**Figure 3. Calculated Stokes band pure rotational Raman spectra of nitrogen and oxygen in air at a temperature of 50 K.**

These scattering processes may be visualized as the perturbation of the molecular eigenfunctions by the electric field associated with the incident photon, inducing transitions via intermediate or virtual levels, and the process occurs with characteristic times on the order of  $10^{-14}$  to  $10^{-12}$  sec. It is the shortness of this characteristic time ( $\tau_S$ ) which precludes the existence of gas collisional effects at reasonable densities; i. e., if the molecular collision time ( $\tau_C$ ) is such that  $\tau_S/\tau_C \ll 1$ , a collision is unlikely during the scattering event, and no collisional effects are to be expected. For a  $\tau_C$  value of  $10^{-12}$  sec, the gas density will be on the order of 100 amagats, and for  $\tau_C$  on the order of  $10^{-14}$  sec, the density will be on the order of  $10^4$  amagats. Consequently, no collisional effects are to be expected for gas density values less than approximately  $10^2$  to  $10^4$  amagats. This is to be contrasted with fluorescence techniques for which the electronic radiative decay processes exhibit characteristic times ( $\tau_F$ ) on the order of  $10^{-8}$  to  $10^{-7}$  sec. Consequently, collisional effects become important for total gas density values on the order of  $10^{-2}$  to  $10^{-3}$  amagat, or lower, depending on the intermolecular collision potential.

For diatomic and polyatomic molecules, the relative intensity distribution of the pure rotational Raman displacements is related to the rotational temperature which, except at very low density, is equal to the translational or static gas temperature. Therefore, by injecting an intense, monochromatic laser beam into a gas flow field and spectroscopically analyzing the pure rotational Raman spectrum, the rotational temperature of the gas may be determined. Moreover, this measurement (1) will be independent of the gas flow velocity due to the extremely short scattering time, (2) will be unaffected by gas collision processes, (3) will have a "point" spatial resolution that decreases very little with increasing density and requires no inversion techniques common to absorption measurements, (4) will not be affected by secondary particles since there will be no ionization process, and (5) the accuracy will increase with increasing gas density.

## 1.2 INTENSITY EQUATIONS

The observed intensity of a pure rotational Raman line of a diatomic or linear polyatomic gas is known to be, for Stokes scattering,

$$I_J \left( \frac{\text{photons}}{\text{sec}} \right) = \sigma_{RRJ} N_g V \Omega' I_o' T_r(J) g_J \frac{(2J+1)}{q_r} \exp[-B_o J(J+1)hc/kT_R] \quad (1)$$

where

$\sigma_{RRJ}$  = the rotational Raman cross section,  $\text{cm}^2/\text{ster}$

$N_g$  = molecular species number density,  $\text{cm}^{-3}$

$V$  = observed scattering volume

$\Omega'$  = the solid angle subtended by the collecting optics

$I'_0$  = the laser beam intensity, photons/sec  $\text{cm}^2$ , at wavelength ( $\lambda_0$ )

$T_r(J)$  = sensitivity factor of optics, spectrometer, and detector

$g_J$  = nuclear spin statistics weighing factor

$J$  = rotational quantum number

$q_r$  = molecular rotational partition function

$B_0$  = rotational constant of the ground vibrational level

$h$  = Planck's constant

$c$  = speed of light

$k$  = Boltzmann's constant

$T_R$  = rotational temperature

The  $J$ -dependent portion of the cross section may be separated from  $\sigma_{RRJ}$ ; i. e.,

$$\sigma_{RRJ} = \frac{C_{RR} S_J}{\lambda_J^4} \quad (2)$$

where the line strength factor ( $S_J$ ) is given by

$$S_J = 3(J + 1)(J + 2)/[2(2J + 1)(2J + 3)] \quad (3)$$

the wavelength  $\lambda_J$  of the rotational Raman line is given by

$$\lambda_J = 1/[\bar{\nu}_0 - 4B_0(J + 3/2)] \quad (4)$$

and  $\bar{\nu}_0$  is the laser line wavenumber and  $C_{RR}(\text{cm}^6)$  of Eq. (2) is a constant.

If one defines a constant C as

$$C = C_{RR} N_g V \Omega' I_o' \quad (5)$$

Eq. (1) may be written as

$$I_J = \frac{C T_r(J) g_J}{\lambda_J^4 q_r} \left[ \left( \frac{3}{2} \right) \frac{(J+1)(J+2)}{(2J+3)} \right] \exp [-B_o J(J+1) hc/k T_R] \quad (6)$$

Since the characteristic rotational temperatures  $B_o hc/k$  for the molecular species investigated in this study, as shown in Table 1, are much less than the kinetic temperatures of the flow fields studied, one may make the following approximation for the rotational partition function:

$$q_r \approx T_R / (\sigma B_o hc/k) \quad (7)$$

where  $\sigma = 2$  for homonuclear species and  $\sigma = 1$  otherwise. This approximation is discussed in a later section.

Table 1. Molecular Spectroscopic Values

Gas	J	$g_J$	$B_o, \text{cm}^{-1}$	$B_o hc/k, \text{K}$
N <sub>2</sub>	0, 1, 2, 3, ...	1: even 2: odd	2.001	2.87
O <sub>2</sub>	1, 3, 5, 7, ...	1	1.438	2.07
CO	0, 1, 2, 3, ...	1	1.923	2.77
CO <sub>2</sub>	0, 2, 4, 6, ...	1	0.3895	0.561

From Eqs. (4) and (6), we find

$$\ell_n \left\{ \frac{I_J (k T_R / \sigma B_o hc)}{[\bar{\nu}_o - 4 B_o (J + 3/2)]^4 T_r(J) g_J \left[ \frac{3}{2} \frac{(J+1)(J+2)}{(2J+3)} \right]} \right\} = \ell_n C - \left( \frac{B_o hc}{k T_R} \right) J(J+1) \quad (8)$$



Written more conveniently in terms of relative intensities,

$$\ln \left\{ \frac{I_J^{\text{rel}} T_R}{\left[ \frac{\bar{\nu}_o - 4B_o(J + 3/2)}{\bar{\nu}_o} \right]^4 g_J \left[ \frac{3}{2} \frac{(J + 1)(J + 2)}{(2J + 3)} \right]} \right\} = \ln C - \left( \frac{B_o h c}{k T_R} \right) J(J + 1) \quad (9)$$

Equation (9) may be solved by iterative computer calculation to find  $T_R$  using measured values of  $I_J^{\text{rel}}$ . The nitrogen  $T_R$  program (PROGRAM RATROT) for the CDC-1604B computer is shown in Table 2.

Table 2. PROGRAM RATROT

```

      TYPE REAL NU,NUNORM,NSUMXY,NSUMXSQ
      TYPE INTEGER VU,vL
      DIMENSION I(24),G(24),XY(24),XSQ(24),DELTAY(24),YI(24),
      *X(24),PEX(24),WAVF(24),TRR(10,25),SIGMATA(10,25),
      *
      *      Tw(100), SIG(100), S(100), SS(100), Y(100),
      1 YY(100), Z(100), W(100), WY(100), ID(10), E(31), O(31) ,
      1SZ(25), TRA(25) ,
      1WB(40),WBB(40),St(40)
300  REAL 333, TWW, LILY
      IF (EOF,50) 331,332
331  STOP
332  LULL=0
      DO 334 L=1,25
        Tw(L) = TWW
334  CONTINUE
      M = 0
      1  REAL 200,RUN
        LULL= LULL + 1
        N= 0
        M = M + 1
        PRINT 100
        PRINT 103,RUN
        PRINT 104
        REAL 201,KMAX
        KKK = KMAX
        DO 3 K=1,KMAX
          REAL 202,I(K)
          IF ((K+1)/2.EQ. K/2) 9999,3
9999 I(K)=2*I(K)
      3  CONTINUE
        TRG=200.
      4  SUMX=0.
        SUMY=0.
        SUMXY=0.
        SUMXSQ=0.
        SUMW=0.
C      WAVELENGTH CALCULATION

```

```

C      DELU = +2  ROTATIONAL RAMAN CALCULATION
      WU=5.145E-05
      WB0=1./WU
      HL=2.001
      DO 5 K=1,KMAX
      JJ=K-1
      WB(K)=WB0-4.*BL*(JJ+1.5)
      WAVE(K)=(1./WB(K))*1.E08
      WBB(K)=(WB0/WB(K))**3.
      SF(K) = (3.*(JJ+1)*(JJ+2))/(2.*(2*JJ+3))
      G(K)=SF(K)/TRG
      Y(K)=LOGF(I(K)*WBB(K)/G(K))
      X(K) = 1.*JJ*(JJ+1)
      XY(K)=X(K)*Y(K)
      XSQ(K)=X(K)*X(K)
      W(K)=I(K)**1
      SUMX=SUMX+(I(K)**1)*X(K)
      SUMY=SUMY+(I(K)**1)*Y(K)
      SUMXY=SUMXY+(I(K)**1)*XY(K)
      SUMXSQ=SUMXSQ+(I(K)**1)*XSQ(K)
5     SUMW=SUMW+W(K)
      SQSUMX=SUMX*SUMX
      PRODSUM=SUMX*SUMY
      SLOPE=(SUMW*SUMXY-PRODSUM)/(SUMW*SUMXSQ-SQSUMX)
      URDCEP=(SUMXSQ*SUMY-SUMX*SUMXY)/(SUMW*SUMXSQ-SQSUMX)
      TR=-2.879/SLOPE
      SUMDELSQ=0.
      SUMWSQ=0.
      SUMWXSQ=0.
      SUMWSQX=0.
      DO 6 K=1,KMAX
      YI(K)=SLOPE*X(K)+URDCEP
      DELTAY(K)=Y(K)-YI(K)
      PER(K)=100.*DELTAY(K)/YT(K)
      SQSLMW=SUMW*SUMW
      SUMWXSQ=SUMWXSQ+(I(K)**2)*XSQ(K)
      SUMWSQX=SUMWSQX+(I(K)**2)*X(K)
      SUMWSQ=SUMWSQ+I(K)**2
6     SUMDELSQ=SUMDELSQ+DELTAY(K)*DELTAY(K)
      SIGMAY=(SUMDELSQ/(KMAX-2.))**.5
      SIGMAT=(2.879*SIGMAY/(SLOPE*SLOPE))*((SQSUMW*SUMWXSQ-2.*SUMW*
      *SUMX*SUMWSQX+SQSUMX*SUMWSQ)**.5)/(SUMW*SUMXSQ-SQSLMW)
      TESTTR=ABSF(TR-TRG)/TR
      IF (TESTTR.LT.1.E-04) 8,7
7     TRG=TR
      GO TO 4
8     N=N+1
      IF (N.GT.1) 11,9
9     DO 10 K = 1, KMAX
      JJ=K-1
10    PRINT 105,JJ,I(K),G(K),Y(K),X(K),WAVE(K),PER(K)
      PRINT 106
      PRINT 107,PRODSUM,NSUMXY,SQSUMX,NSUMXSQ
      PRINT 108,SLOPE,URDCEP
      PRINT 109
      PRINT 110,KMAX,TR,SIGMAT
      TRR(M*KMAX) = TR

```

```

    SIGMATA(M, KMAX) = SIGMAT
    KMAX=KMAX-1
    GO TO 4
11 PRINT 111,KMAX,TH,SIGMAT
    TRR(M*KMAX) = TR
    SIGMATA(M, KMAX) = SIGMAT
    KMAX=KMAX-1
    IF (KMAX.GT.1) 4,400
400 IF (LULU.LT.LILY) 1,12
12 CONTINUE
    KMAX = KKK
    PHINT 65
65 FORMAT (1F1)
19 CONTINUE
    IF (KMAX.GT.1) 18,990
18 CONTINUE
    PRINT 70

    DO 13 J = 1, M
    PHINT 80, TRR(J,KMAX), TW(J), SIGMATA(J, KMAX)
13 CONTINUE
    DO 14 J = 1, M
    Y(J) = TRR(J, KMAX)/TW(J)
    S(J) = SIGMATA(J, KMAX)/TW(J)
    SS(J) = S(J)**2.
    YY(J) = Y(J)/SS(J)
    Z(J) = 1./SS(J)
    W(J) = SS(1)/SS(J)
14 WY(J) = W(J) * W(J) * SS(J)
    SUM1 = 0.0 $ SUM2 = 0.0 $ SUM3 = 0.0 $ SUM4 = 0.0
    DO 15 J = 1, M
    SUM1 = SUM1 + YY(J)
    SUM2 = SUM2 + Z(J)
    SUM3 = SUM3 + WY(J)
15 SUM4 = SUM4 + W(J)
    TRBAR = SUM1/SUM2
    SIGBAR = (SUM3/(SUM4 * SUM4)) ** 0.5
    PHINT 30, TRBAR, SIGBAR
    PHINT 210, KMAX, M
    SSS = SIGBAR * TWW
    SZ(KMAX) = 1. / (SSS*SSS)
    TRA(KMAX) = TRBAR*TWW*SZ(KMAX)
C
    KMAX = KMAX - 1
    PHINT 23
23 FORMAT (1F0, ///)
    GO TO 19
990 CONTINUE
    PHINT 23
    IF (KKK.GT.4) 991,993
991 CONTINUE
    PHINT 1000
    PHINT 1003
    DO 992 JM = 4, KKK
    S1 = 0.0
    S2 = 0.0
    DO 994 J = 3, JM
    S1 = S1 + TRA(J)

```

```

994 S2 = S2 + S2(J)
      TRABS = S1/S2
      SIGABS = (1./S2)**0.5
      SIGABS = 2.*SIGABS
C     THE 2 SIGMA ERROR IS QUOTED
992 PRINT 1001,JM,TRABS,SIGABS
      GO TO 300
993 PRINT 1002
      GO TO 300
1000 FORMAT(1H ,10X,30HWEIGHTED AVERAGE T CALCULATION//)
1001 FORMAT(1H ,5X,15,5X,F10.2,5X,F10.2//)
1002 FORMAT(1H ,3X,26HFOUR LINE VALUE IS AVERAGE/)
1003 FORMAT(1H ,5X,8HNO. LINES,5X,10HAVE. TEMP.,5X,9HNO SIGMA/)
210 FORMAT (1H0, 5X, 5HUSING, 13, 18H LINES, AVERAGE OF, 12, 5H RUNS
30 FORMAT (1H0,15HAVERAGE TEMP = , F15.9, 5X, 16HAVERAGE SIGMA = ,
1F10.5)
70 FORMAT (1H , 20HMEASURED TEMPERATURE, 5X, 16HWALL TEMPERATURE,
*10X, 18HSTANDARD DEVIATION //)
80 FORMAT (1H , 3X, F15.9, 7X, F15.9, 13X, F10.5)
100 FORMAT (1H1,/,47X,25HROTATIONAL BOLZMANN PLOT)
101 FORMAT (1H ,/,57X,5HUSING)
102 FORMAT (1H ,/,52X,14HMUNITZ G-FACTOR)
103 FORMAT(1H ,//,21X,12HRUN NUMBER =,1X,A8)
104 FORMAT (1H ,//,6X,1HK,7X,4HI(K),11X,4HG(K),15X,4HY(K),15X,4HX(K),
*13X,10HWAVELENGTH,9X,27H(DELTA Y(K))/YT(K), PERCENT)
105 FORMAT (1H ,4X,12,6X,15,8X,E11.4,8X,E11.4,8X,E11.4,8X,E11.4,
*12X,E11.4)
106 FORMAT (1H ,//,5X,13HSUM(X)*SUM(Y),6X,9HN*SUM(XY),8X,
*13HSUM(X)*SUM(X),6X,10HN*SUM(X*X))
107 FORMAT (1H ,5X,E11.4,6X,E11.4,7X,E11.4,7X,E11.4)
108 FORMAT (1H ,//,21X,7HSLOPE =,1X,E11.4,10X,11HINTERCEPT =,1X,E11.4
109 FORMAT (1H ,//)
110 FORMAT (1H ,15X,12,6H-LINES,5X,24HROTATIONAL TEMPERATURE =,
*E11.4,5X,26HSTANDARD DEVIATION OF TR =,E11.4)
111 FORMAT (1H ,15X,12,6H-LINES,5X,24H
*,E11.4,5X,26H
*,E11.4)
200 FORMAT(A8)
201 FORMAT (I2)
202 FORMAT (I5)
333 FORMAT (F10.3, I2)
      END TROT

```

The program essentially performs a least-squares fit of the data points to a straight line, and the slope of that line is used to calculate the rotational temperature  $T_R$ . The iteration process continues to calculate a temperature until consecutive calculated values are within 0.01 percent. It should be noted that, in the least-squares fit, the line intensity values ( $I_j^{\text{rel}}$ ) are weighed according to the reciprocal of the square

of the fractional standard deviation of the relative line intensity. Therefore, the more intense and, thereby, more precise lines of the spectrum are directly given more weight in the temperature determination process. For details of the temperature determination, see Appendix A.

From Eq. (1) the total observed intensity of the pure rotational Raman Stokes lines is

$$I_T \left( \frac{\text{photons}}{\text{sec}} \right) = \frac{N_g V \Omega' I_o'}{q_r} \sum_{J=0}^{\infty} \sigma_{RRJ} T_r(J) g_J (2J + 1) \exp [-B_o J(J + 1) hc / k T_R] \quad (10)$$

To avoid the measurement of absolute intensities, it is noted that, if  $I_T^{\text{rel}}$  is measured for a known static gas density and temperature, a calibration factor ( $C_F$ ) can be determined such that the number density ( $N_g$ ) of a gas flow can be determined from

$$N = \frac{C_F I_T^{\text{rel}} \sum_{J=0}^{J_{\max}} g_J (2J + 1) \exp [-B_o J(J + 1) hc / k T_R]}{\sum_{J=0}^{J_{\max}} g_J \left[ \frac{(J + 1)(J + 2)}{(2J + 3)} \right] \left\{ \exp [-B_o J(J + 1) hc / k T_R] \right\}} \quad (11)$$

in which

$J_{\max}$  = rotational quantum number corresponding to the largest wavelength change which is detectable

$I_T^{\text{rel}}$  = total relative intensity of the pure rotational Raman Stokes lines

$T_R$  = the measured rotational temperature

$$q_r = \sum_{J=0}^{J_{\max}} g_J (2J + 1) \exp [-B_o J(J + 1) hc / k T_R]$$

$$C_F = \frac{N_c \sum_{J=0}^{J_{\max}} g_J \left[ \frac{(J + 1)(J + 2)}{(2J + 3)} \right] \left\{ \exp [-B_o J(J + 1) hc / k T_c] \right\}}{I_{T_c}^{\text{rel}} \sum_{J=0}^{J_{\max}} g_J (2J + 1) \exp [-B_o J(J + 1) hc / k T_c]} \quad (12)$$

In Eq. (12),  $N_C$  and  $T_C$  are the known static gas density and temperature, respectively, and  $I_{T_C}^{rel}$  = calibration value of the total relative intensity of the pure rotational Raman Stokes' lines. The calculations indicated in Eqs. (11) and (12) are performed by PROGRAM NUMRHO as shown in Table 3.

Table 3. PROGRAM NUMRHO

```

*PROGRAM LS,60
11  DIMENSION KI(25),KT(25),KN(25)
21  REAL IO,NO
31  READ(105,7)M
41  7 FORMAT(12)
51  111 READ(105,1)(IO,T0,NO
61  1 FORMAT(3E10,3)
71  READ(105,2)KMAX
81  2 FORMAT(12)
91  READ(105,3)(KI(K),KT(K),K=1,KMAX)
101 3 FORMAT(2E10,3)
111 CF=NO/IO
121 KA1=2.0/3.0
131 RB1=1.0
141 DO 101 J=1,23,2
151 RJ=J
161 KA1=KA1+((RJ+1.)*(RJ+2.)/(2.0*RJ+3.)*EXP(-2.879*RJ*(RJ+1.)/T0))/2.0
171 RB1=RB1+((2.0*RJ+1.)*EXP(-2.879*RJ*(RJ+1.)/T0))/2.0
181 101 CONTINUE
191 DO 105 J=2,24,2
201 RJ=J
211 KA1=KA1+(RJ+1.)*(RJ+2.)/(2.0*RJ+3.)*EXP(-2.879*RJ*(RJ+1.)/T0)
221 RB1=RB1+(2.0*RJ+1.)*EXP(-2.879*RJ*(RJ+1.)/T0)
231 105 CONTINUE
241 CF=CF*KA1/RB1
251 WRITE(108,112)KA1,RB1,CF
261 112 FORMAT(1H1,8KA1 =$,1PE13.6,5X,8RB1 =$,1PE13.6,5X,8C( =$,1PE13.6)
271 DO 102 K=1,KMAX
281 KB=2.0/3.0
291 RA=1.0
301 DO 103 J=1,23,2
311 RJ=J
321 KA=KA+((2.0*RJ+1.)*EXP(-2.879*RJ*(RJ+1.)/KT(K)))/2.0
331 KB=KB+((RJ+1.)*(RJ+2.)/(2.0*RJ+3.)*EXP(-2.879*RJ*(RJ+1.)/KT(K)))/2.0
341 103 CONTINUE
351 DO 104 J=2,24,2
361 RJ=J
371 KA=KA+(2.0*RJ+1.)*EXP(-2.879*RJ*(RJ+1.)/KT(K))
381 KB=KB+(RJ+1.)*(RJ+2.)/(2.0*RJ+3.)*EXP(-2.879*RJ*(RJ+1.)/KT(K))
391 104 CONTINUE
401 KN(K)=CF*KI(K)*KA/KB
411 WRITE(108,114)K
421 114 FORMAT(1H0,8K =$,12)
431 WRITE(108,113)KA,KB
441 113 FORMAT(1H0,8KA =$,1PE13.6,5X,8KB =$,1PE13.6)
451 102 CONTINUE

```

```

46:      WRITE(108,6)ID,T0,N0
47:      6 FORMAT(1H1,5I0,5$,1PE13.6,5X,$T0,5$,1PE13.6,5X,$N0,5$,1PE13.6)
48:      WRITE(108,5)
49:      5 FORMAT(1H0,5K$,10X,$I(K)$,14X,$T(K)$,14X,$N(K)$)
50:      WRITE(108,4)(K,R1(K),RT(K),RN(K),K=1,KMAX)
51:      4 FORMAT(1H0,12,5X,1PE13.6,5X,1PE13.6,5X,1PE13.6)
52:      M=M+1
53:      IF(M.EQ.0) GO TO 110
54:      GO TO 111
55: 110 STOP
56:      END

```

Carbon dioxide ( $\text{CO}_2$ ), although a polyatomic species, in its ground electronic and vibrational state may be treated as a linear molecule with no electronic angular momentum. Unlike  $\text{N}_2$ ,  $\text{O}_2$ , and  $\text{CO}$ , at room temperature the twofold degenerate deformation vibrational mode has approximately 8 percent of the  $\text{CO}_2$  molecules in the first vibrational level, and consequently, Eqs. (4), (6), et seq. to be rigorously correct should explicitly indicate that  $B_0$  and  $B_1$  are required. However, in light of the spectral resolution employed in this study, differences in the rotational constant  $B_v$  due to rotation-vibration coupling are not observed and will henceforth be neglected.

The pure rotational Raman spectrum of  $\text{O}_2$  is more complex than that of  $\text{N}_2$  or  $\text{CO}$ , for example. The ground electronic states of  $\text{N}_2$  and  $\text{CO}$  are both  $^1\Sigma$ , i. e., singlet states, but the ground electronic state of  $\text{O}_2$  is a  $^3\Sigma$ , or triplet state. This difference manifests itself as additional structure of the rotational energy levels and hence of the rotational Raman spectra as two satellite components adjacent to primary Raman lines. As will be seen later, however, with moderate spectral resolution, the satellite lines are not resolved, i. e., the intensities of the satellite lines and primary line are approximately summed together. Since the sum of the line strengths for the satellites and primary line are the same as the line strength for the rotational Raman line of a molecule with a  $^1\Sigma$  ground electronic state, we are, therefore, justified in cases of moderate spectral resolution in treating  $\text{O}_2$  as a molecule with a  $^1\Sigma$  ground electronic state.

Spectroscopic constants and statistical weights for use in Eqs. (9) and (11) for the molecular species studied are given in Table 1.

## 2.0 EXPERIMENTAL APPARATUS

### 2.1 LABORATORY SYSTEM

For laboratory verification studies, the experimental arrangement shown in Fig. 4 was used. The laser source was a Coherent Radiation Model 52-B argon ion laser nominally operated at a power level of 1.5 watts at either a 488.0- or 514.5-nm wavelength. As shown in Fig. 4, the laser beam was deflected 90 deg by a front surface mirror and focused by a 50.8-mm-diam fused-silica lens of 250-mm focal length into the center of the scattering chamber. By using the relations of Schwiesow (Ref. 6), which are given in Appendix B, the diameter of the observed scattering volume was  $220.5 \mu\text{m}$ . The scattering cell was designed similarly to that of Gerry and Rose (Ref. 7), and it was made of black anodized aluminum. The laser beam entered the scattering chamber through a fused-silica window, and from the focal point within the chamber, the beam expanded and entered a laser dump. This dump consisted of an offset 5-deg cone of 72-cm-length black anodized aluminum fitted inside a closed end piece of black anodized aluminum tubing which was bolted to the scattering cell. The focal region of the laser beam was observed at 90 deg through a fused-silica window. Directly across the cell from the observation port was a viewing dump that consisted of a black anodized 15-deg cone of 25.4-cm length housed in a closed-end piece of black anodized aluminum tubing which was bolted to the scattering cell. This viewing dump provided a dark background for the observation of the laser beam.

The entire scattering chamber was evacuable to  $10^{-5}$  torr and was essentially leak-free. Gases of interest were leaked into the chamber through a Matheson Model G134 filter and through a series of valves including a needle valve which were connected to the high-pressure gas bottles. Pressures in the scattering chamber were measured with a calibrated Wallace and Tiernan gage, and chamber temperature was measured with a copper-constantan thermocouple connected to an L & N temperature indicator. The chamber temperature could be lowered by flowing  $\text{LN}_2$  through insulated copper coils wrapped around the scattering cell.



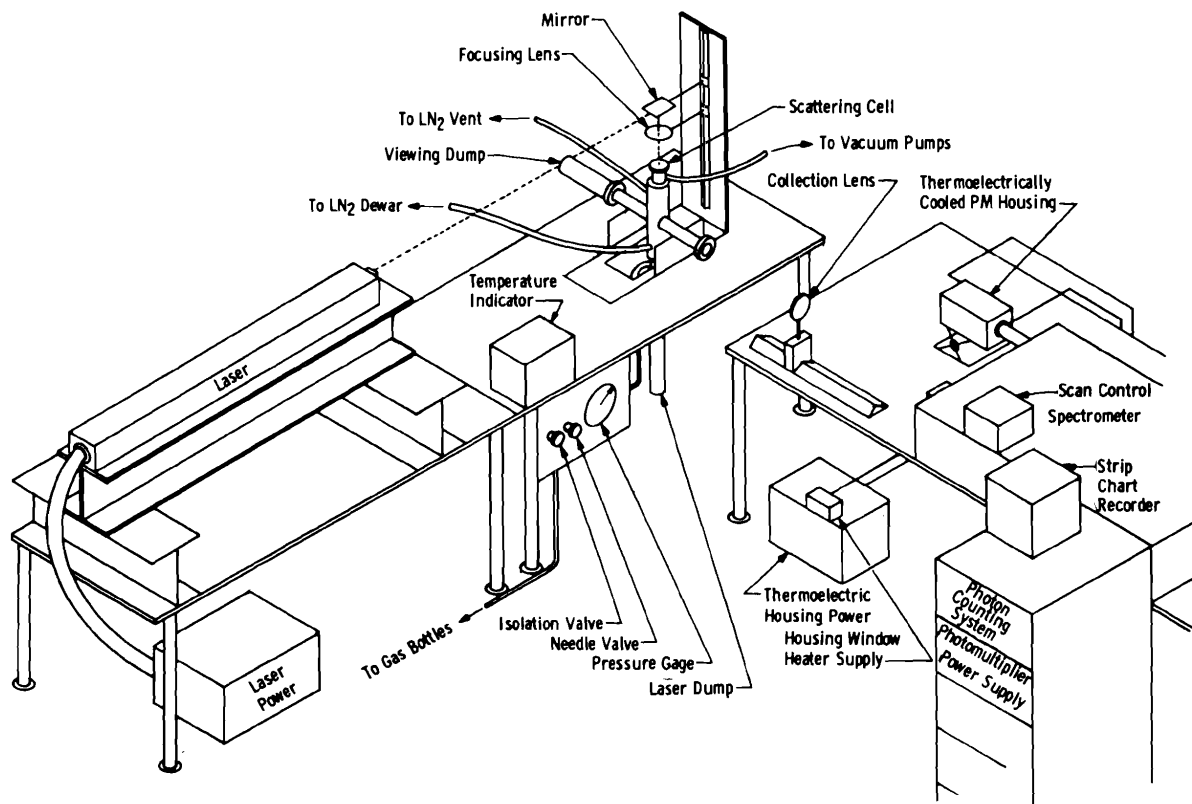


**Figure 4. Schematic of laboratory experimental arrangement.**

The focal volume of the laser beam was 61-cm from the 7.6-cm diam, 30.5-cm focal length, fused-silica collection lens. Collected light was focused onto the entrance slit of the spectroscopic element located 61 cm from the collection lens. A magnification of one was thus achieved. The spectroscopic element was a Spex 1402 double spectrometer with a Czerny-Turner mount. The two ganged 102- by 102-mm gratings with 1200 grooves/mm were blazed at 5000 Å with an efficiency of approximately 70 percent, and silvered mirrors provided maximum throughput. The focal length was 0.85 meters, and the reciprocal linear dispersion was approximately 0.44 nm/mm. The aperture was approximately  $f/8$  and was, therefore, matched to the collection optics. The spectrometer could be either synchronously scanned at rates of from 0.2 to 100 nm/min or digitally (incrementally) scanned at rates of from 0.005 to 125 nm/min. Radiation passing through the exit slit was collected by a 47.6-mm-diam, 25.4-mm focal length glass lens and focused onto the photocathode of the photomultiplier. A schematic of the collection and spectrometer optics is shown in Fig. 5.

The photomultiplier tube was an EMI-9502B with an S-11 spectral response (see Fig. 6) and a 10-mm-diam photocathode, and the tube was contained in a thermoelectrically cooled Products for Research, Inc., Model TE-104 housing. The housing could operate continuously at  $-26^{\circ}\text{C}$ , which provided a reduction in dark current by approximately a factor of 45 from the room temperature value. The schematic of the Products for Research, Inc., photomultiplier voltage divider network is shown in Fig. 7. Power to the photomultiplier was supplied by a well-regulated, highly stable Fluke 405B power supply.

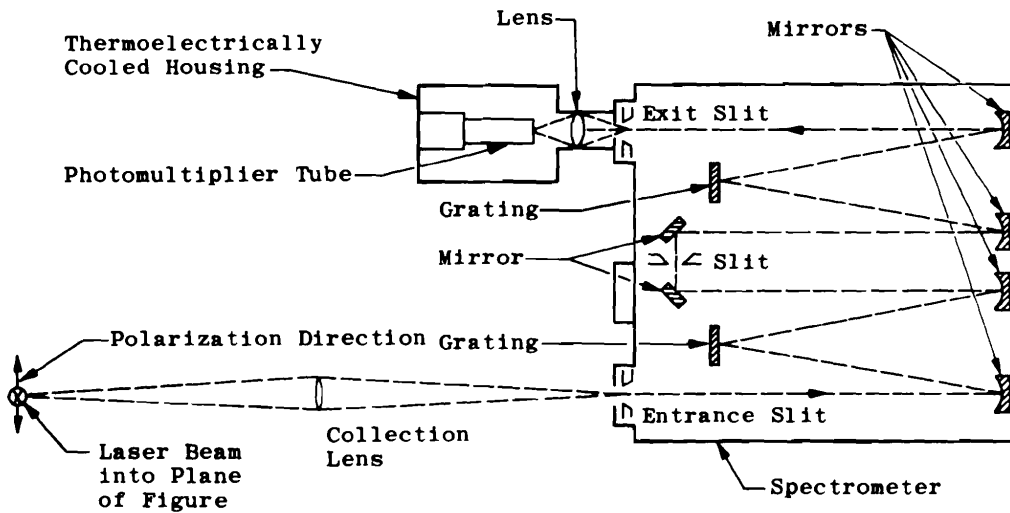


Figure 5. Schematic of collection and spectrometer optics.

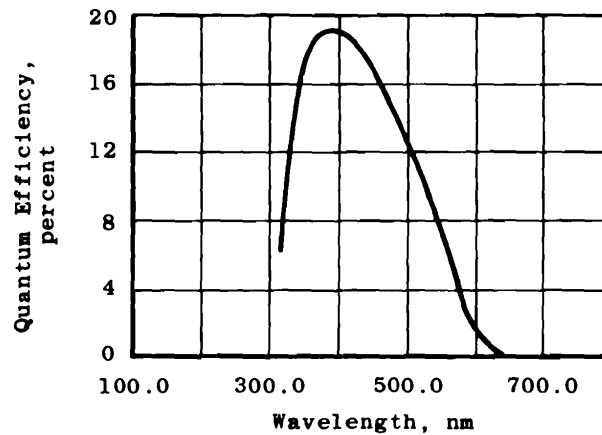


Figure 6. Spectral response curve of EMI-9502B photomultiplier.

Unless Otherwise  
Specified:

Resistors 220 K, 2%, 1 w

Capacitors 0.01  $\mu$ f, 1 kv

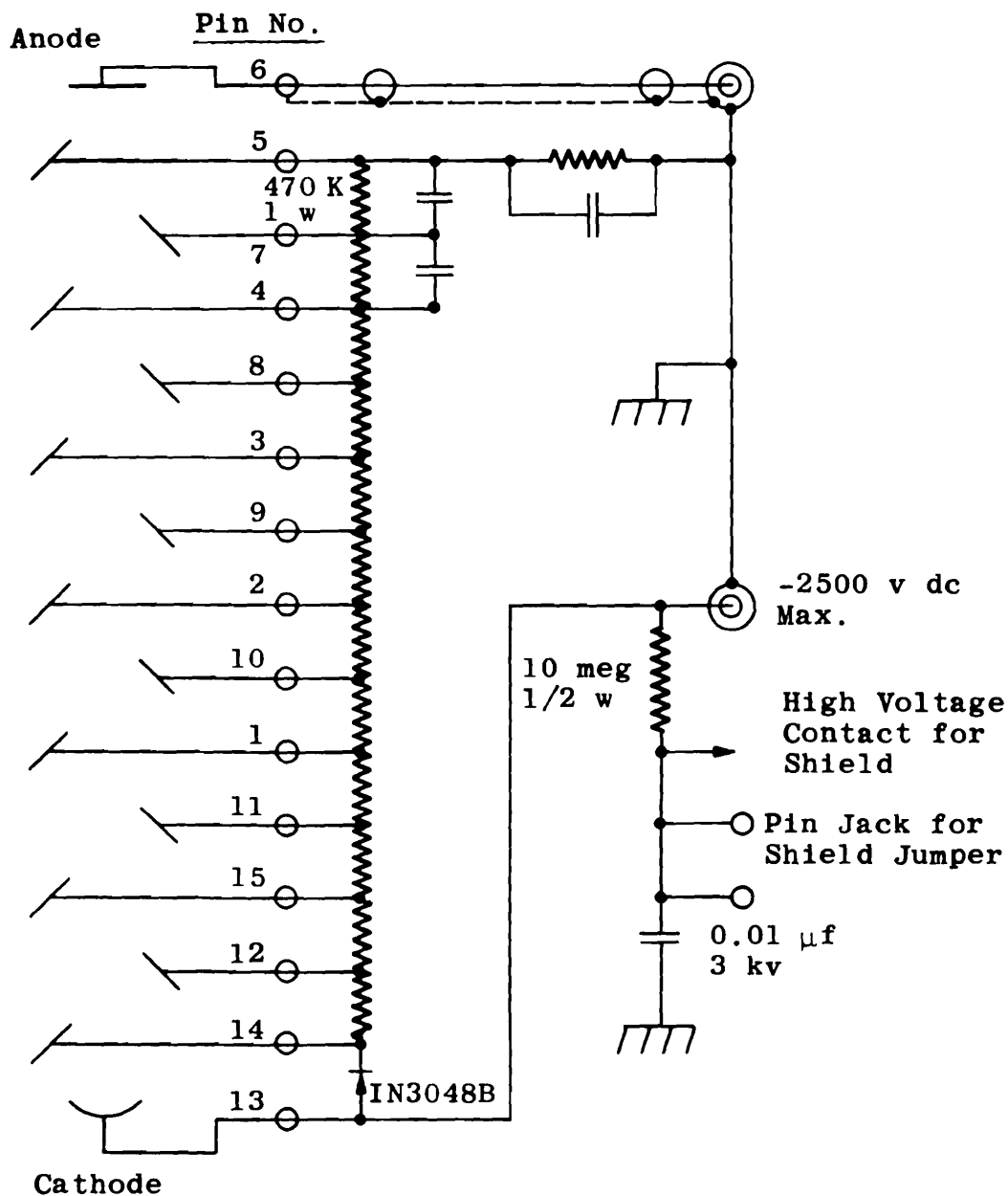


Figure 7. Voltage divider network of EMI-9502B photomultiplier.

The output of the photomultiplier tube was processed by an ORTEC photon counting system which is shown in the block diagram of Fig. 8. The coaxial output cable from the photomultiplier tube was terminated with a 50-ohm resistor at the Model 454 amplifier input. The amplified pulses were then passed through a Model 436 discriminator to both a Model 715 dual counter/timer and a Model 441 ratemeter. The rate-meter output was displayed by either a Clevite Brush Mark 250 or a Honeywell Electronik 19 strip-chart recorder.

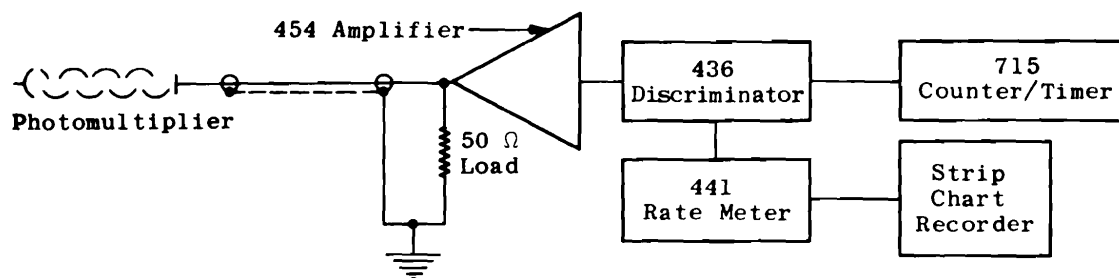


Figure 8. Block diagram of photon counting system.

## 2.2 RESEARCH CHAMBER SYSTEM

For the flow measurements in the von Kármán Facility 4- by 10-ft Research Chamber, the experimental arrangement shown in Fig. 9 was used. The vacuum chamber was a cylindrical stainless steel vessel 4 ft in diameter and approximately 10 ft long and is shown in Fig. 10. Initial pumping capabilities were provided by an 8500 liter/min mechanical pump for rough pumping and 15-cm oil diffusion pump for intermediate pumping. Final pumping was provided by both 77 K liquid N<sub>2</sub> and 20 K gaseous He liners inside the chamber. With no gas flow, an ultimate pressure of  $10^{-7}$  torr was achieved, and with mass flow rates exceeding 1 gm/sec, background pressures less than  $2 \times 10^{-3}$  torr could be maintained. Both ionization and alphasatron gages monitored the chamber pressure. The gas sources used were either a sonic orifice of exit diameter of 1.325 mm or a conical nozzle of 1.04-mm throat diameter, exit plane area ratio of 13.4, and half-angle of approximately 14.5 deg. Schematics of these sources are shown in Figs. 11 and 12.

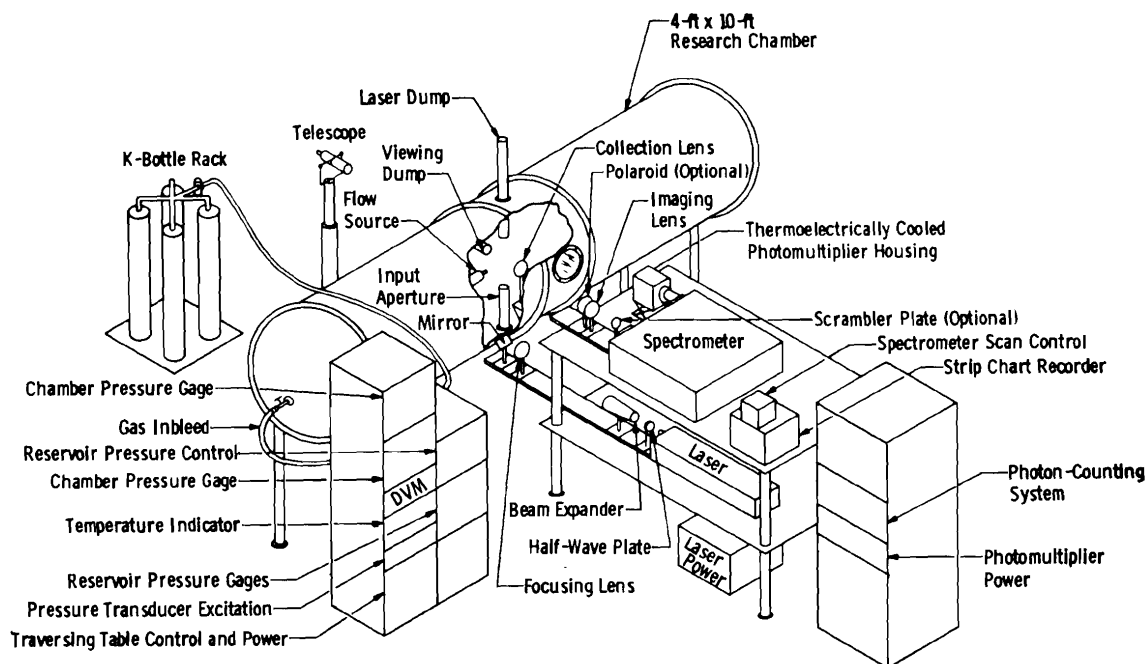


Figure 9. Schematic of 4- by 10-ft Research Chamber experimental arrangement.

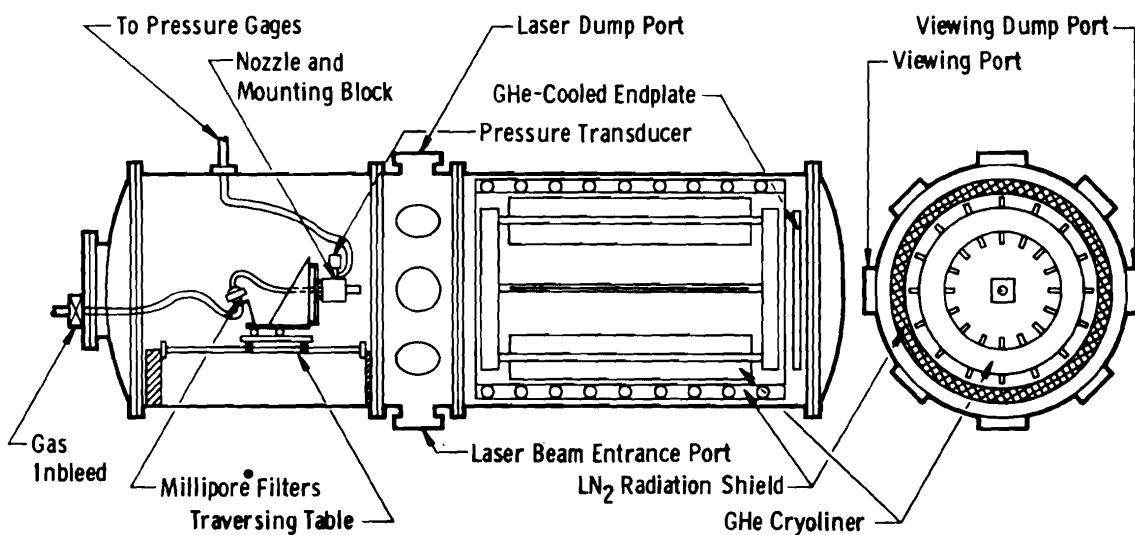


Figure 10. Schematic of 4- by 10-ft Research Chamber.

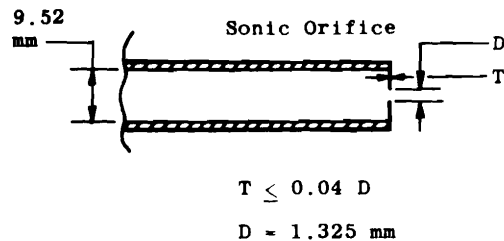


Figure 11. Schematic of sonic orifice.

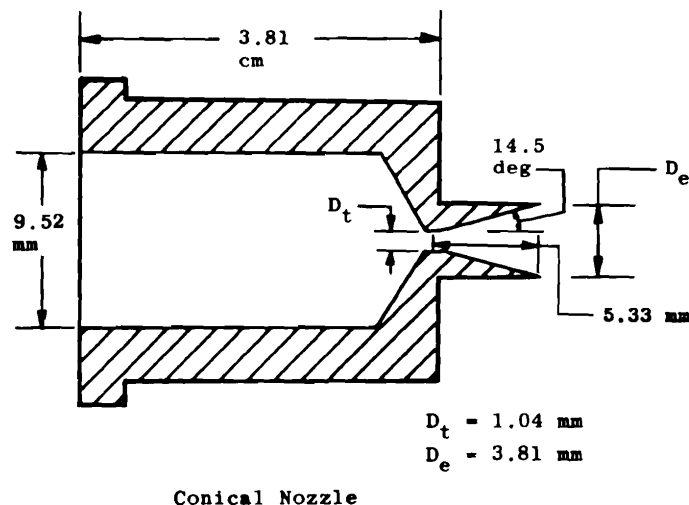


Figure 12. Schematic of conical nozzle.

The sources were mounted on an x-y-z motor-driven traversing mechanism to provide flow field profile studies with fixed optical instrumentation. Imprecision of the axial movement was 0.013 cm. Reservoir temperatures were determined with copper-constantan thermocouples, and reservoir pressures were obtained with either an absolute pressure transducer or gage. Gases were supplied to the flow generators from a high-pressure K-bottle through a series of valves and a needle valve to provide fine control of the reservoir pressure. The gases and purity grades used were as follows: N<sub>2</sub>, prepurified, 99.998-percent purity; O<sub>2</sub>, industrial grade, 99.95-percent purity; CO, C-P grade, 99.5-percent purity; CO<sub>2</sub>, Coleman grade, 99.99-percent purity. To minimize effects of dust and particulate matter from the bottles and lines, two Millipore filters were installed in parallel upstream of the flow generators. These filters removed particles of diameters of 0.025  $\mu\text{m}$  and larger. A schematic of the gas inbleed system is shown in Fig. 13.

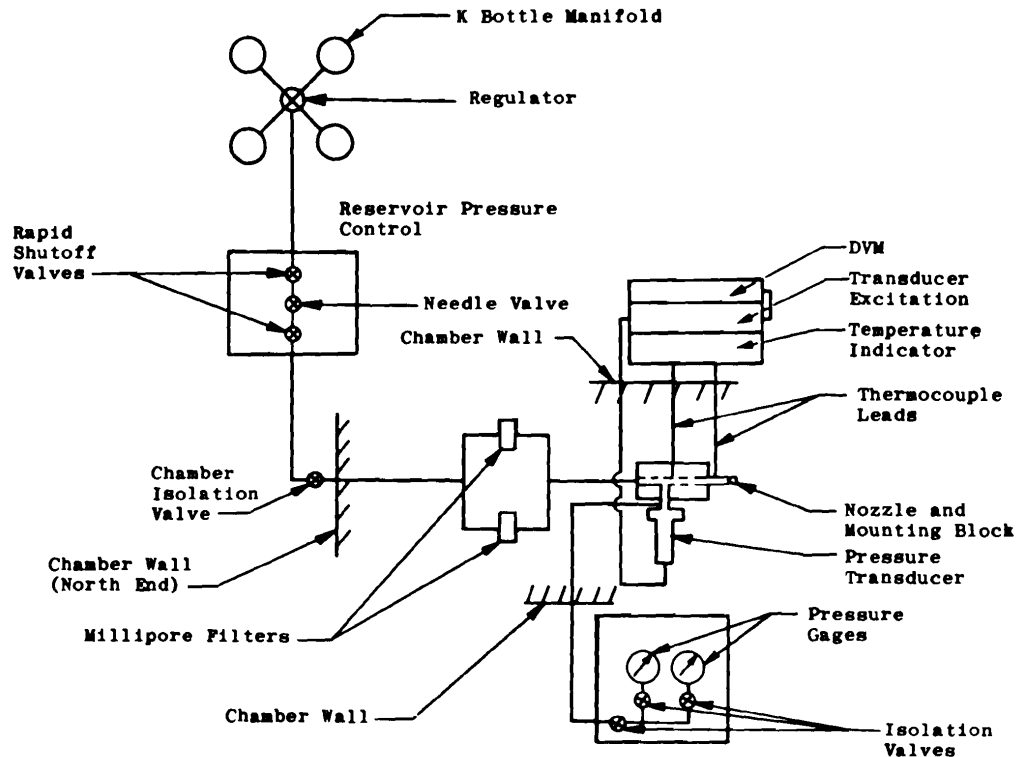


Figure 13. Schematic of 4-by 10-ft Research Chamber gas inbleed system.

Once again, the argon ion laser was the light source. The normal vertical polarization of the laser beam was rotated 90 deg by a half-wave plate, and the 1.4-mm-diam laser beam was directed into a 28X beam expander. The resulting 39.2-mm-diam beam was focused by a 50.8-mm-diam, 1000-mm focal length, fused-silica lens and deflected upward through a fused-silica window into the center of the test chamber by a front surface mirror as shown in Fig. 9. By using the relations given in Appendix B, the diameter of the scattering volume was  $31.5 \mu\text{m}$ . As the laser beam defocused, it entered a laser dump, the entrance of which was a black cardboard tube which extended into the chamber to within 22.5 cm of the chamber centerline. The latter stage of the dump was a black anodized aluminum tube capped with a black anodized conical section.

The focal region of the laser was located at the focal point of the collection optics system which was oriented at 90 deg with respect to both the flow-field axis and laser beam. A 76.2-mm-diam, 152.4-mm focal length quartz lens located inside the chamber collected and collimated the scattered radiation and transmitted it through a glass port to

a 101.6-mm-diam, 304.8-mm focal length glass lens. This lens focused the scattering volume onto the entrance slit of the Spex double spectrometer with a magnification of two. The collection optics system external to the chamber was shrouded with layers of green felt. For further reduction of stray light, a collection optics viewing dump, consisting of a piece of closed-end black cardboard tubing, was located on the side of the test chamber collinear with the scattering volume and the center of the collection lens. All optically accessible surfaces inside the test chamber were painted with a flat black coating.

The signal detection and processing system was the same for the flow field measurements as the laboratory studies.

### 3.0 MEASUREMENTS

#### 3.1 LABORATORY MEASUREMENTS

Prior to laboratory measurements, a careful alignment of the scattering volume with the spectrometer slit had to be accomplished. With the laser operating at very low power, a visual alignment of the laser beam with the scattering chamber centerline was completed, the chamber was sealed, and noninhaled cigarette smoke was orally blown into the chamber. With the laser now operating at a moderate power level, the resulting intense scattered light allowed easy alignment of the image of the scattering volume with the entrance slit of the spectrometer. Fine adjustment was accomplished by using the Model 1450 Periscope Viewer accessory for the Spex double spectrometer. With the periscope down, the image of the scattering volume framed by the entrance slit was projected onto a viewing screen. By lateral adjustment of the collection optics lens and slight adjustment of the spectrometer legs, the scattering volume image was centered precisely in the entrance slit, and the periscope was simply retracted.

After evacuation of the chamber to  $10^{-5}$  torr, the gases of interest were then slowly inbled into the chamber until the desired pressure was obtained. The Stokes lines of the pure rotational Raman spectra of  $N_2$  were scanned at atmospheric pressure and room temperature (see Figs. 14 and 16) and at an equivalent room temperature pressure of 10 torr and temperatures of 296, 215, 163, and 104 K. The 298 and 163 K scans are shown in Figs. 18 and 20, respectively. The nitrogen Boltzmann plots, i. e., the plots of Eq. (9), are shown in Figs. 15, 17,



19, and 21. The measured rotational temperatures determined from slopes of the straight lines are all within  $\pm 2$  percent of the measured gas temperature. Scans of room temperature and atmospheric pressure  $O_2$  (Fig. 22),  $CO_2$  (Fig. 24), and  $CO$  (Fig. 26) were made, and the respective Boltzmann plots are shown in Figs. 23, 25, and 27. Again the rotational temperatures agreed to within  $\pm 2$  percent of the measured gas temperatures.

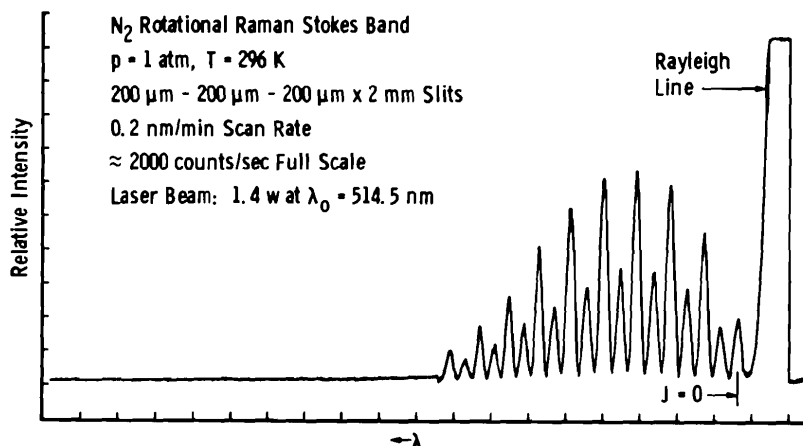


Figure 14. Pure rotational Raman spectrum of nitrogen at atmospheric pressure and room temperature.

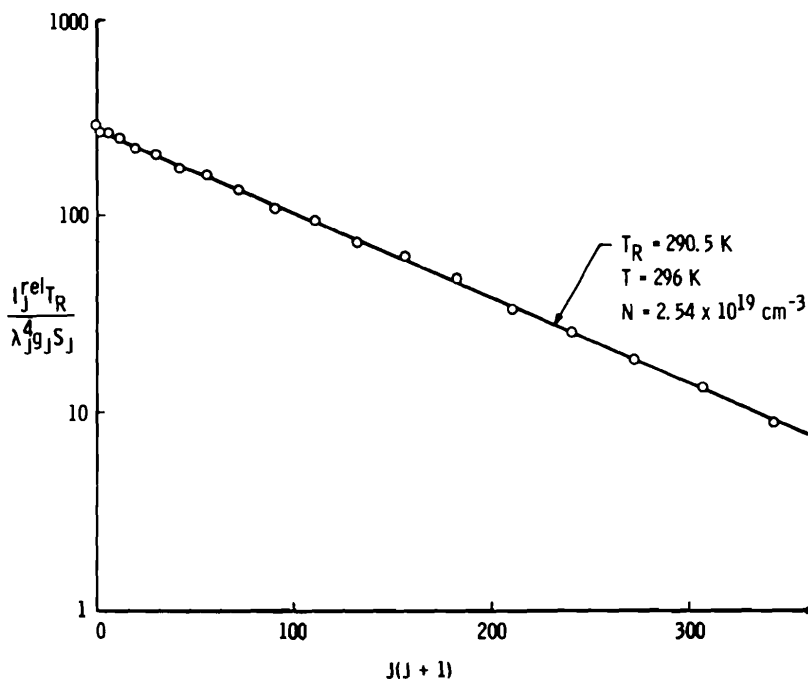


Figure 15. Boltzmann plot of pure rotational Raman line intensities from Fig. 14.

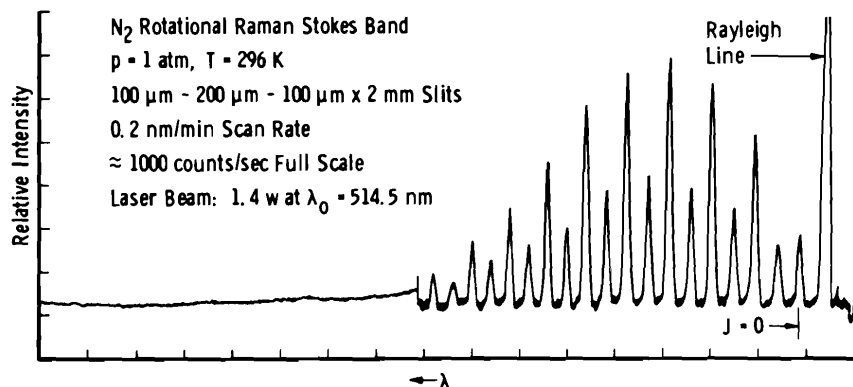


Figure 16. Pure rotational Raman spectrum of nitrogen at atmospheric pressure and room temperature.

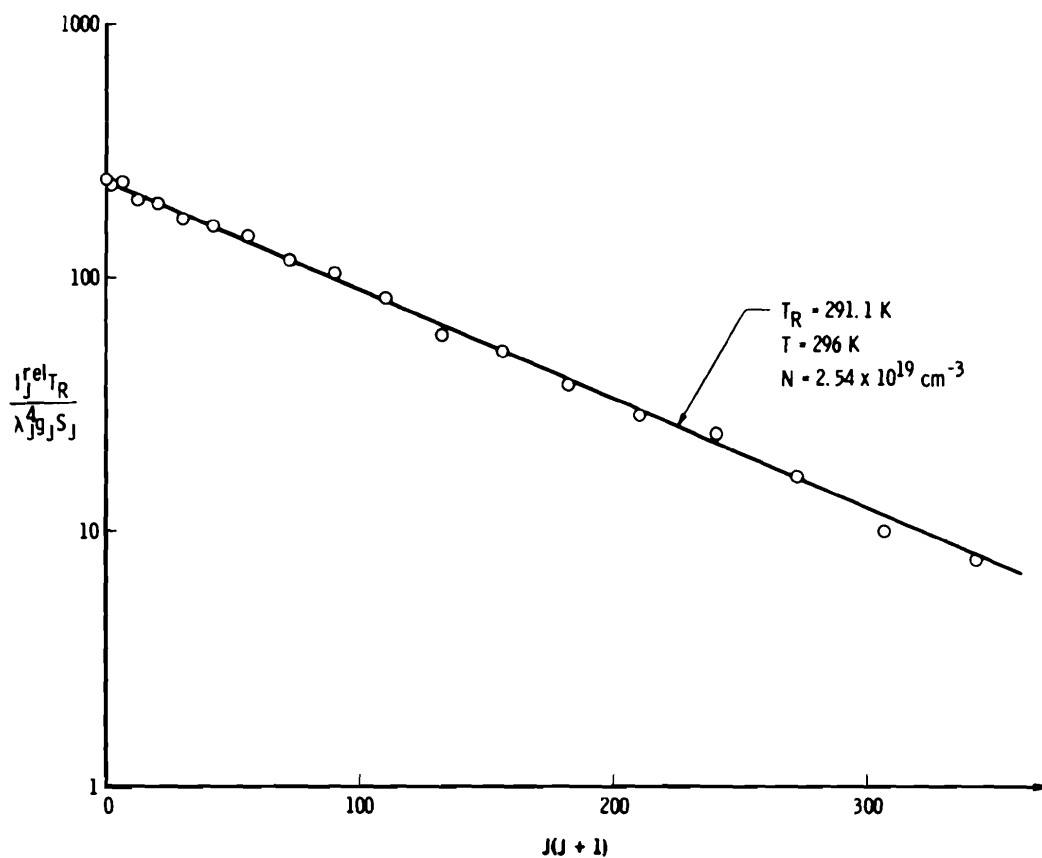


Figure 17. Boltzmann plot of pure rotational Raman line intensities from Fig. 16.

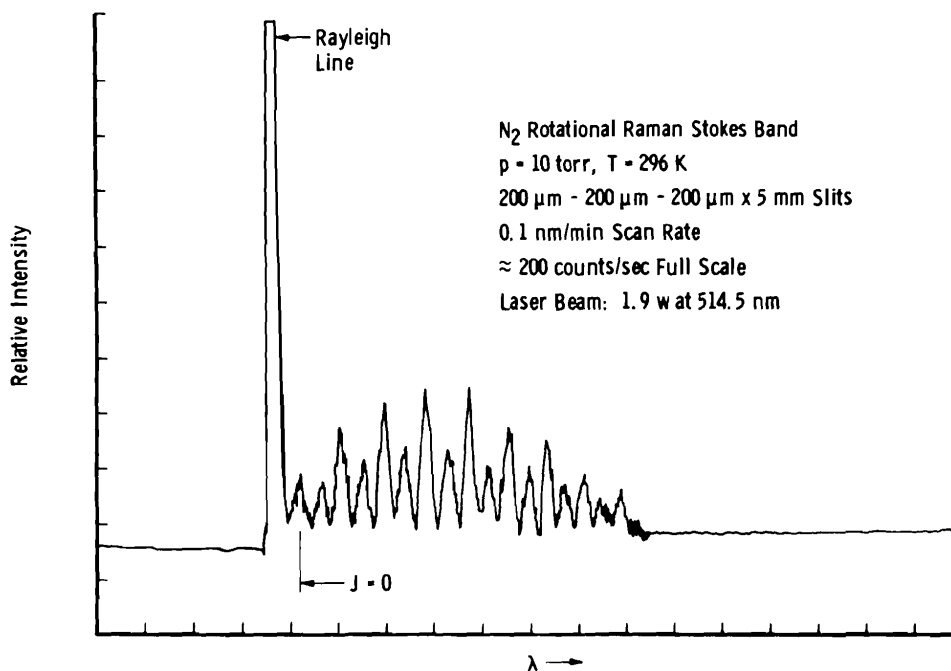


Figure 18. Pure rotational Raman spectrum of nitrogen at 10-torr pressure and room temperature.

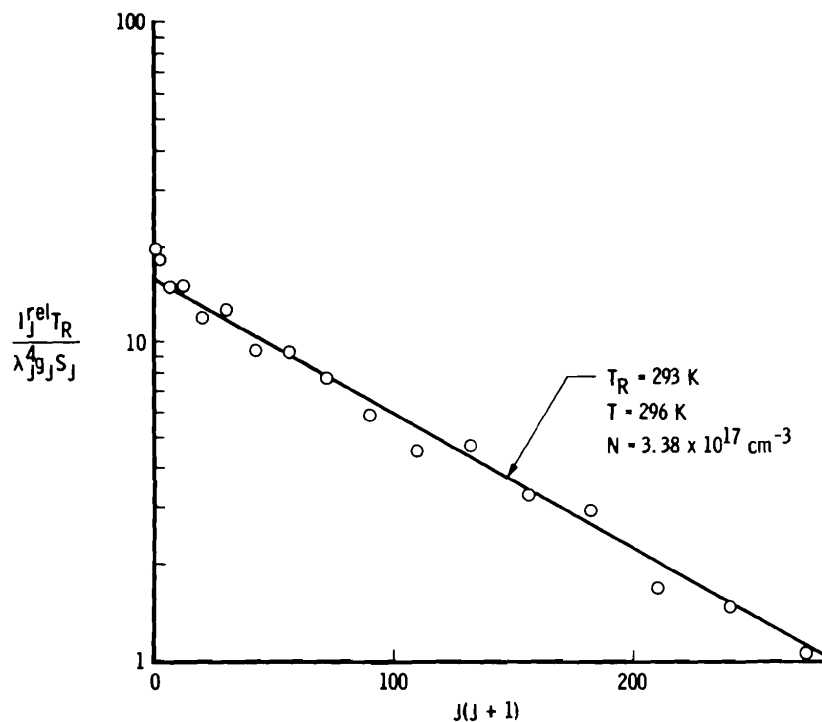


Figure 19. Boltzmann plot of pure rotational Raman line intensities from Fig. 18.

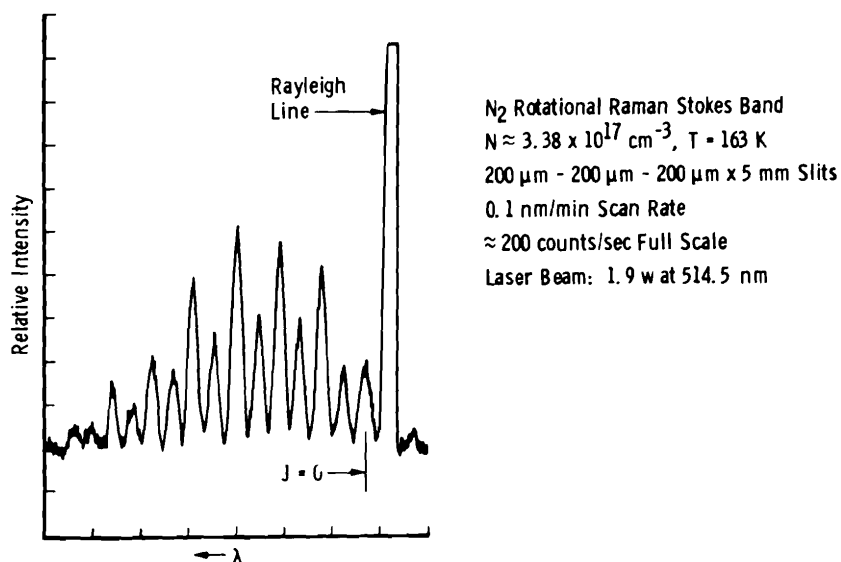


Figure 20. Pure rotational Raman spectrum of nitrogen at an equivalent room temperature pressure of 10 torr and a temperature of 163 K.

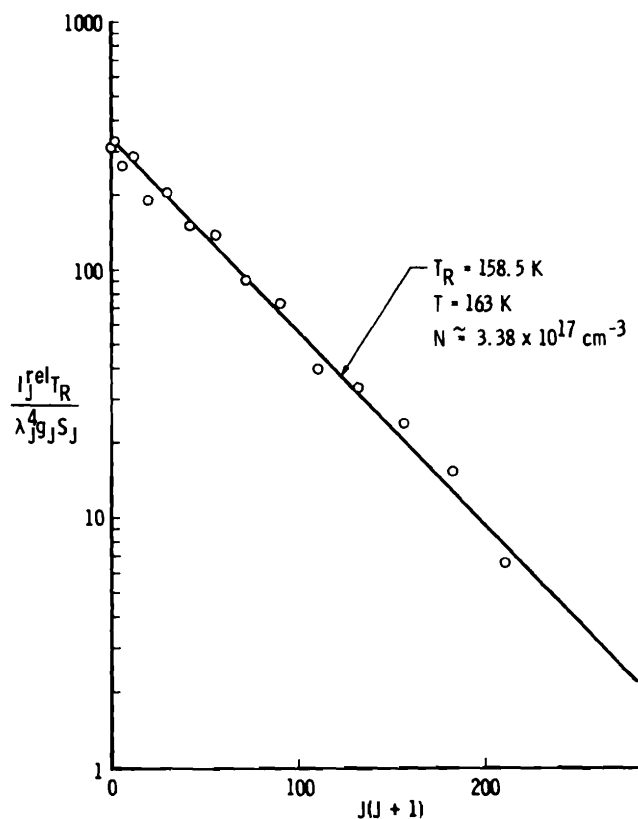


Figure 21. Boltzmann plot of pure rotational Raman line intensities from Fig. 20.

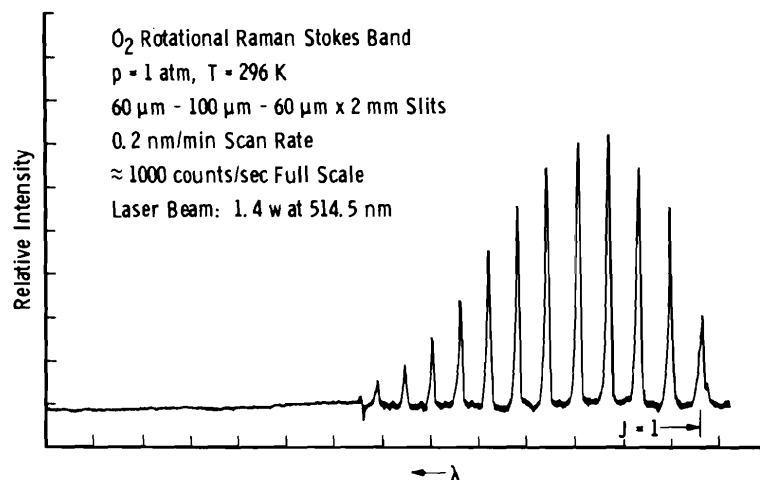


Figure 22. Pure rotational Raman spectrum of oxygen at atmospheric pressure and room temperature.

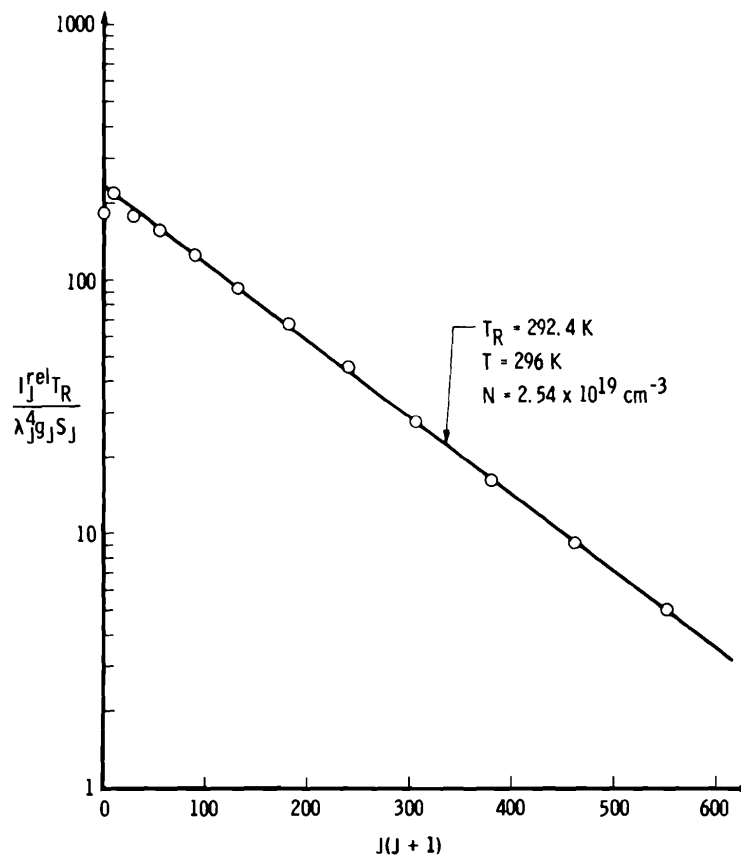


Figure 23. Boltzmann plot of pure rotational Raman line intensities from Fig. 22.

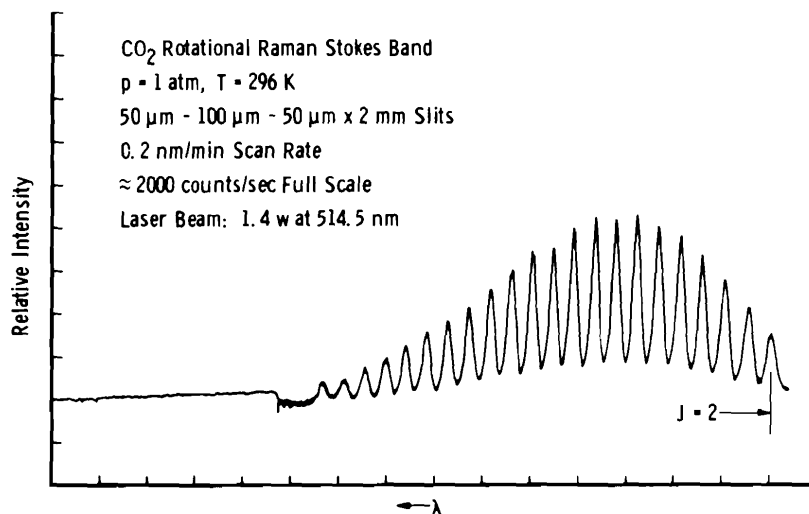


Figure 24. Pure rotational Raman spectrum of carbon dioxide at atmospheric pressure and room temperature.

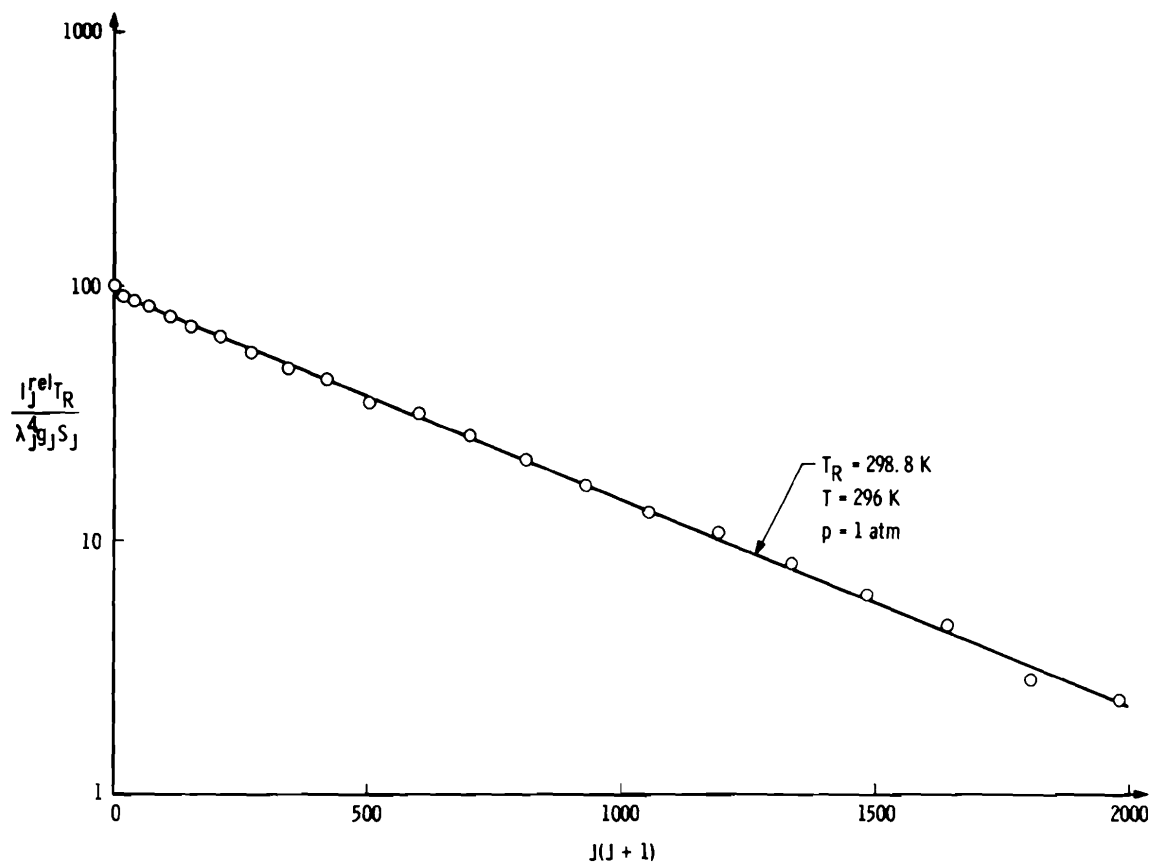


Figure 25. Boltzmann plot of pure rotational Raman line intensities from Fig. 24.

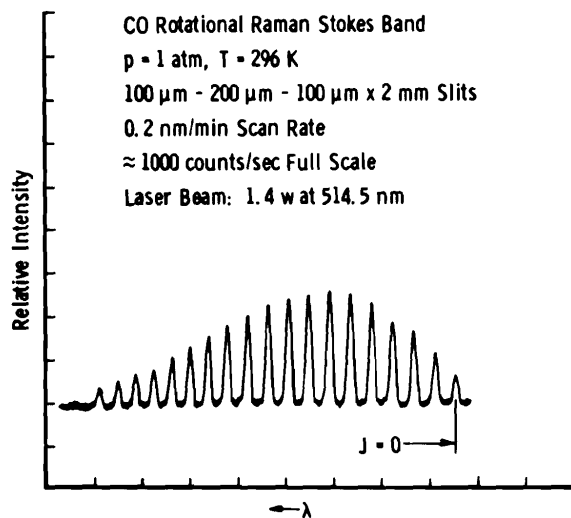


Figure 26. Pure rotational Raman spectrum of carbon monoxide at atmospheric pressure and room temperature.

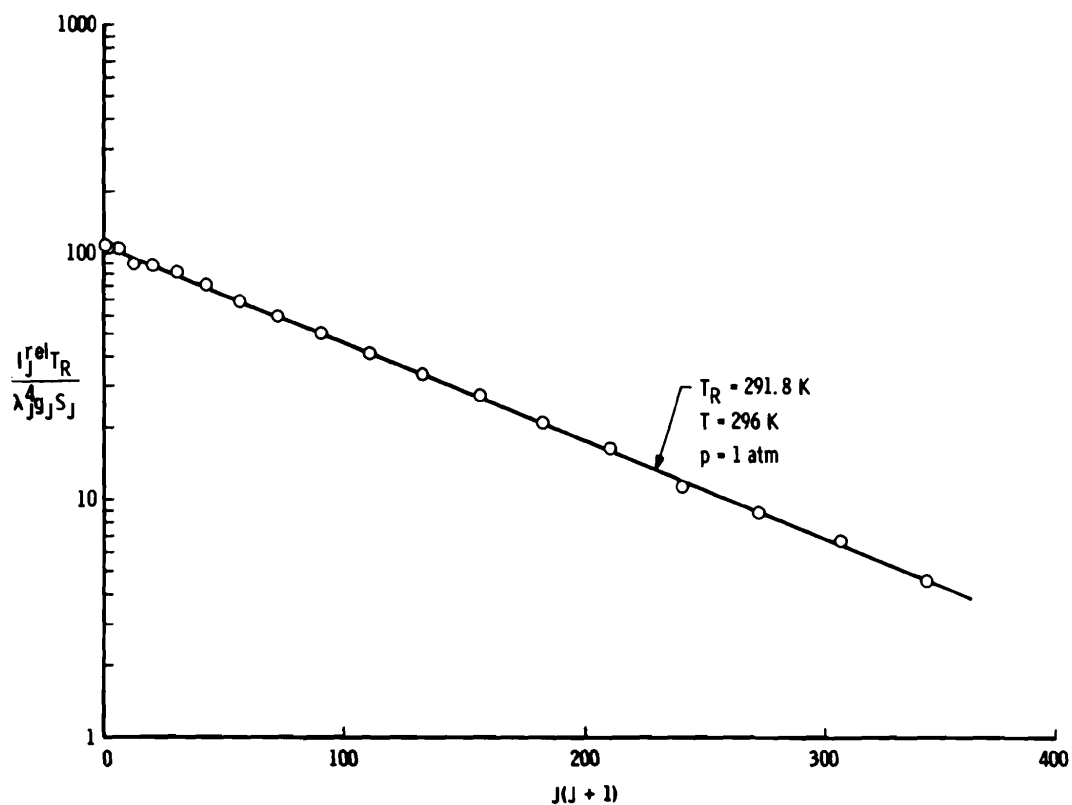


Figure 27. Boltzmann plot of pure rotational Raman line intensities from Fig. 26.

It became obvious that minor improvements in the laser and collection optics could decrease the minimum number density from  $3.38 \times 10^{17} \text{ cm}^{-3}$  (equivalent room temperature, 10 torr) to nearly  $3.38 \times 10^{16} \text{ cm}^{-3}$  (equivalent room temperature, 1 torr). Furthermore, the measurements had been made with relative ease, and sufficient accuracy was attained in the rotational temperature determination; therefore, rotational temperature measurements in hypersonic flow fields were initiated.

### 3.2 FLOW-FIELD MEASUREMENTS

For the flow-field measurements in the 4 by 10 Research Chamber, not only was a careful alignment of the scattering volume with the spectrometer slit required, but a very accurate measurement of the position of the scattering volume relative to the free jet or nozzle exit plane was necessary. With the laser operating at moderate power and focused into the approximate center of the chamber, a small, flat-faced, incandescent light with frosted bulb was placed opposite the scattering volume from the collection lens with the front surface of the bulb nearly touching the finely focused laser beam. Collection optics were adjusted in such a manner that the image of the lighted bulb was in focus on the spectrometer entrance slit and centered on the scattering volume defining aperture which was an adjustable iris located just in front of the spectrometer entrance slit. With two strips of black tape placed horizontally across the bulb face separating the desired distance for good spatial resolution, the defining aperture diameter was adjusted to match this restricted bulb image. After removing the bulb, the laser was operated at high power, and the periscope viewer attachment was again used to precisely align the scattering volume image in the spectrometer entrance slit.

A K & E telescope mounted outside the chamber and collinear with the collection optics was focused onto the scattering volume. After partial evacuation of the chamber, the telescope crosshairs were centered on the scattering volume. Axial location of the flow generator exit plane was then readily determined by axially traversing the generator until the edge of the exit plane and the telescope vertical crosshair were aligned. The vertical and radial zero positions were measured by establishing a flow field, making vertical and radial Rayleigh scattering intensity profile measurements, and determining the zero positions from the flow field symmetry.



Initial measurements were performed for sonic orifice expansions for which the source diameter ( $D$ ) was 1.325 mm and the orifice wall thickness ( $t$ ) was such that  $D/t > 25$ . Figures 28 and 29 show typical low temperature  $N_2$  rotational Raman spectra. Spectrometer scan rates were typically 0.1 to 0.2 nm/min with 10- and 5-sec time constants, respectively, and entrance, middle, and exit slit widths were 200-200-200  $\mu\text{m}$ , respectively.

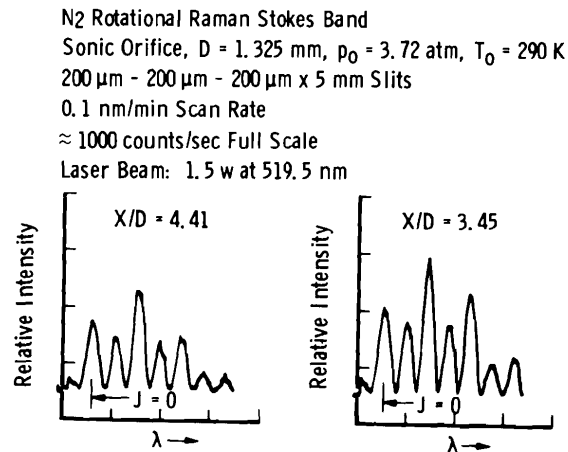


Figure 28. Typical low temperature pure rotational Raman spectrum of nitrogen in a hypersonic flow.

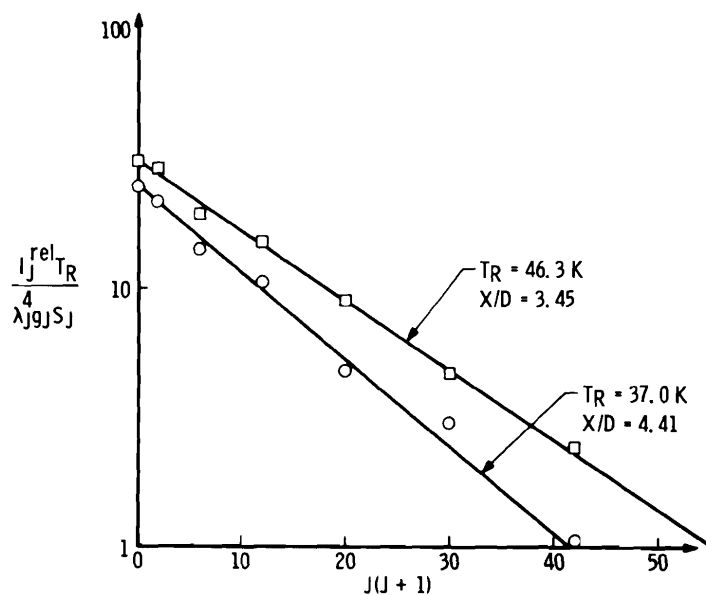


Figure 29. Boltzmann plot of pure rotational Raman line intensities from Fig. 28.

The measured axial variation of the temperatures for N<sub>2</sub> stagnation pressures of 2.8, 3.72, 5.58, and 7.44 atm are shown in Figs. 30 through 33, respectively.

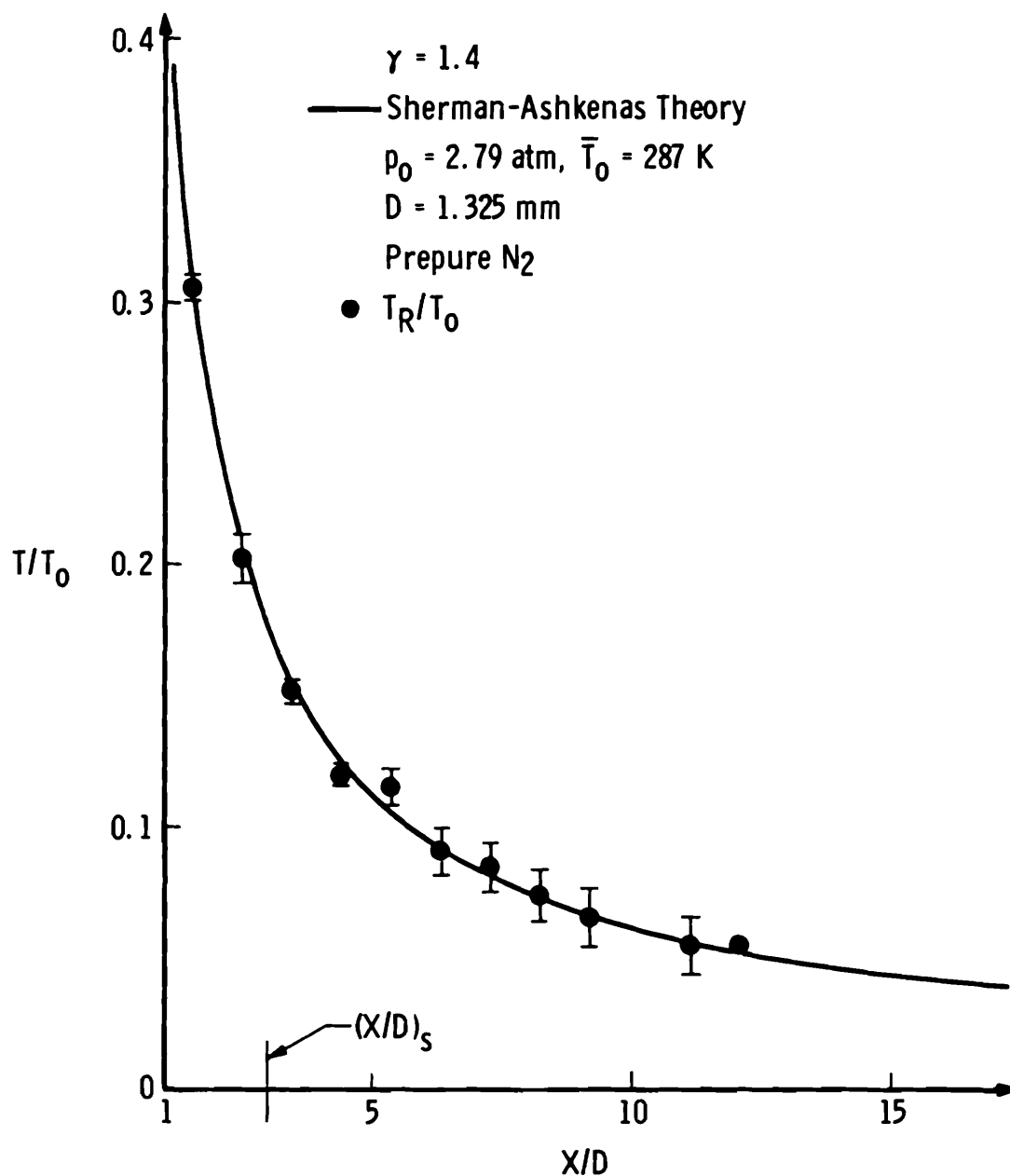


Figure 30. Axial variation of  $T_R/T_0$  for a free-jet nitrogen flow with  $P_0 = 2.79 \text{ atm}$ .

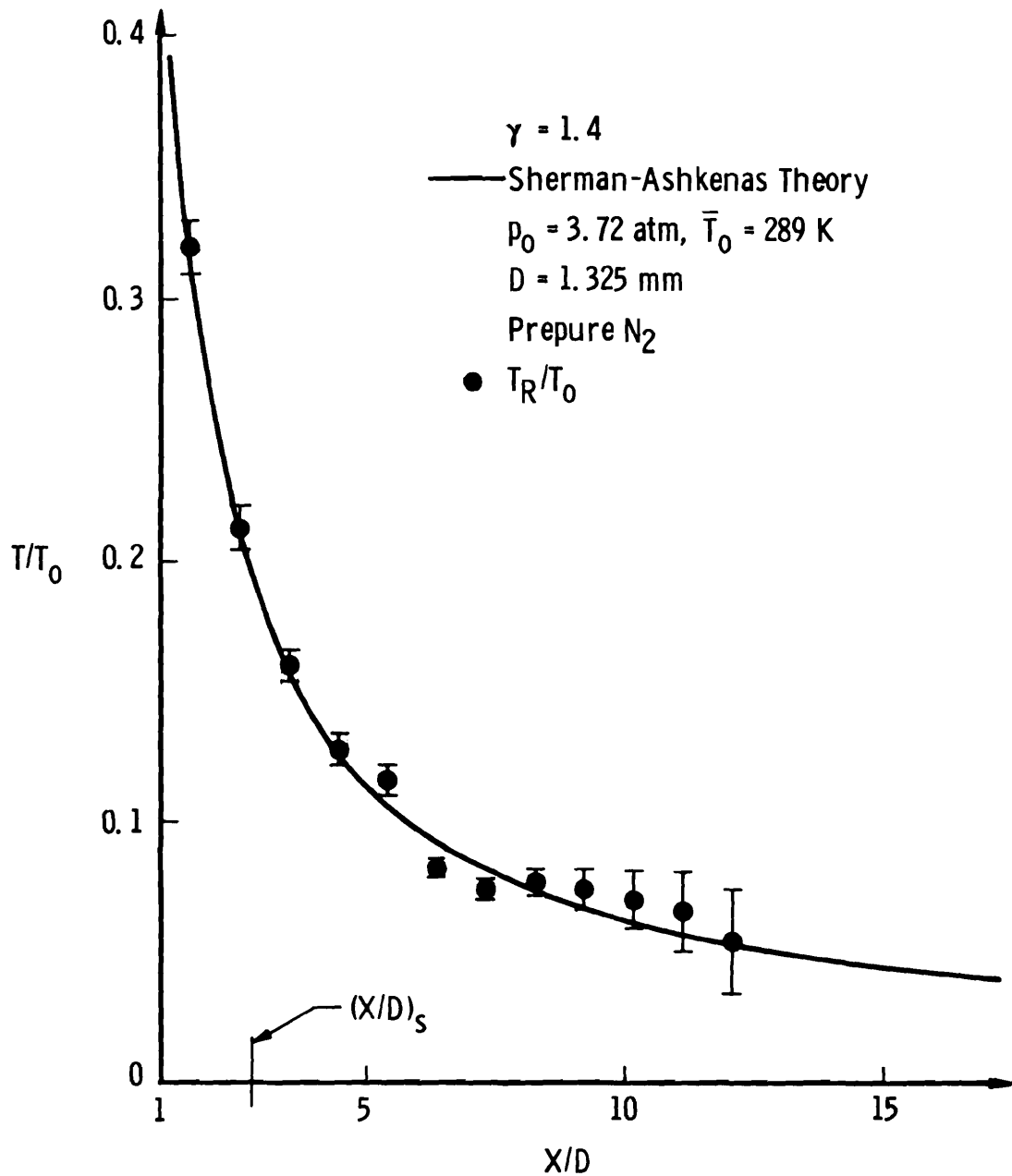


Figure 31. Axial variation of  $T_R/T_0$  for a free-jet nitrogen flow with  $P_0 = 3.72 \text{ atm}$ .

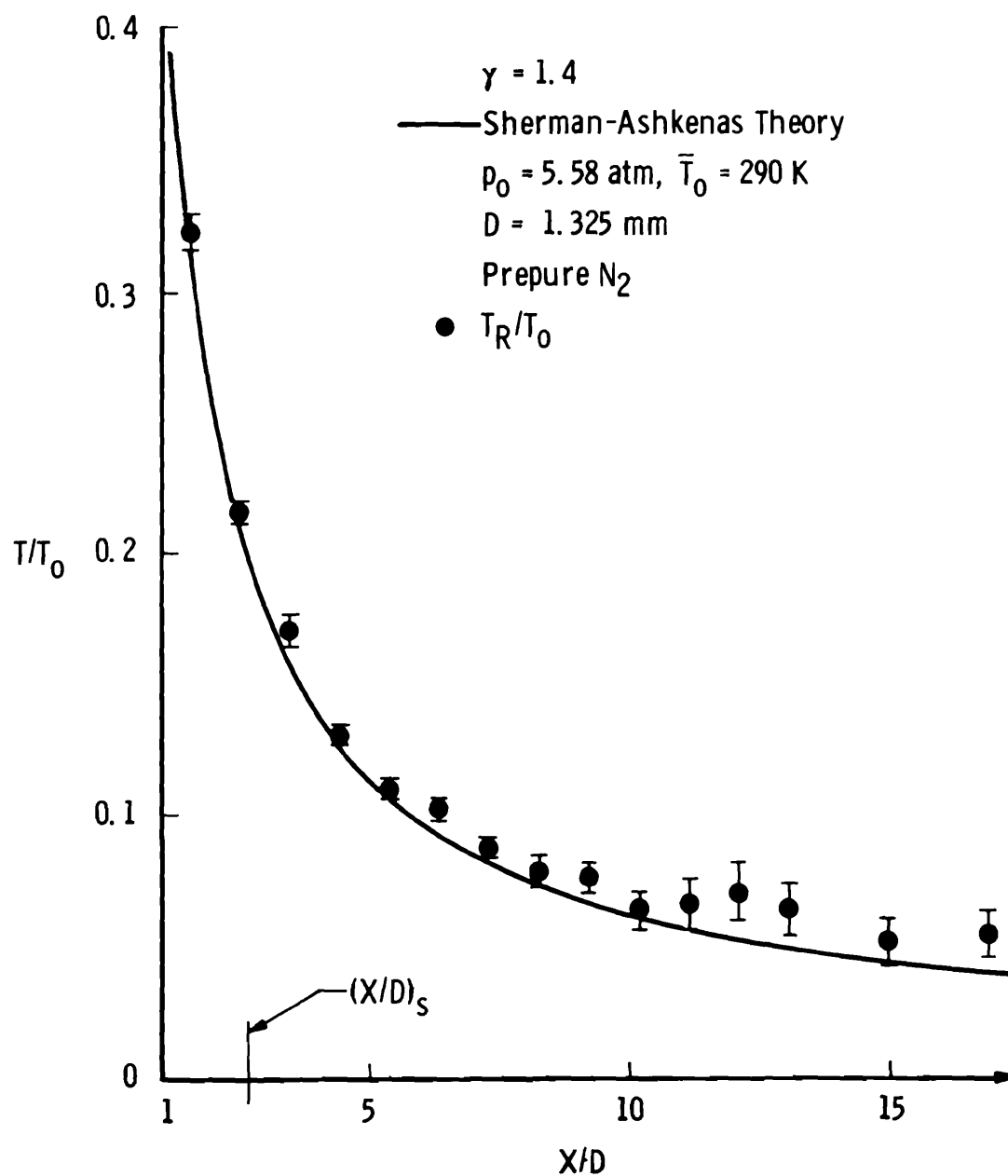


Figure 32. Axial variation of  $T_R/T_0$  for a free-jet nitrogen flow with  $P_0 = 5.58 \text{ atm}$ .

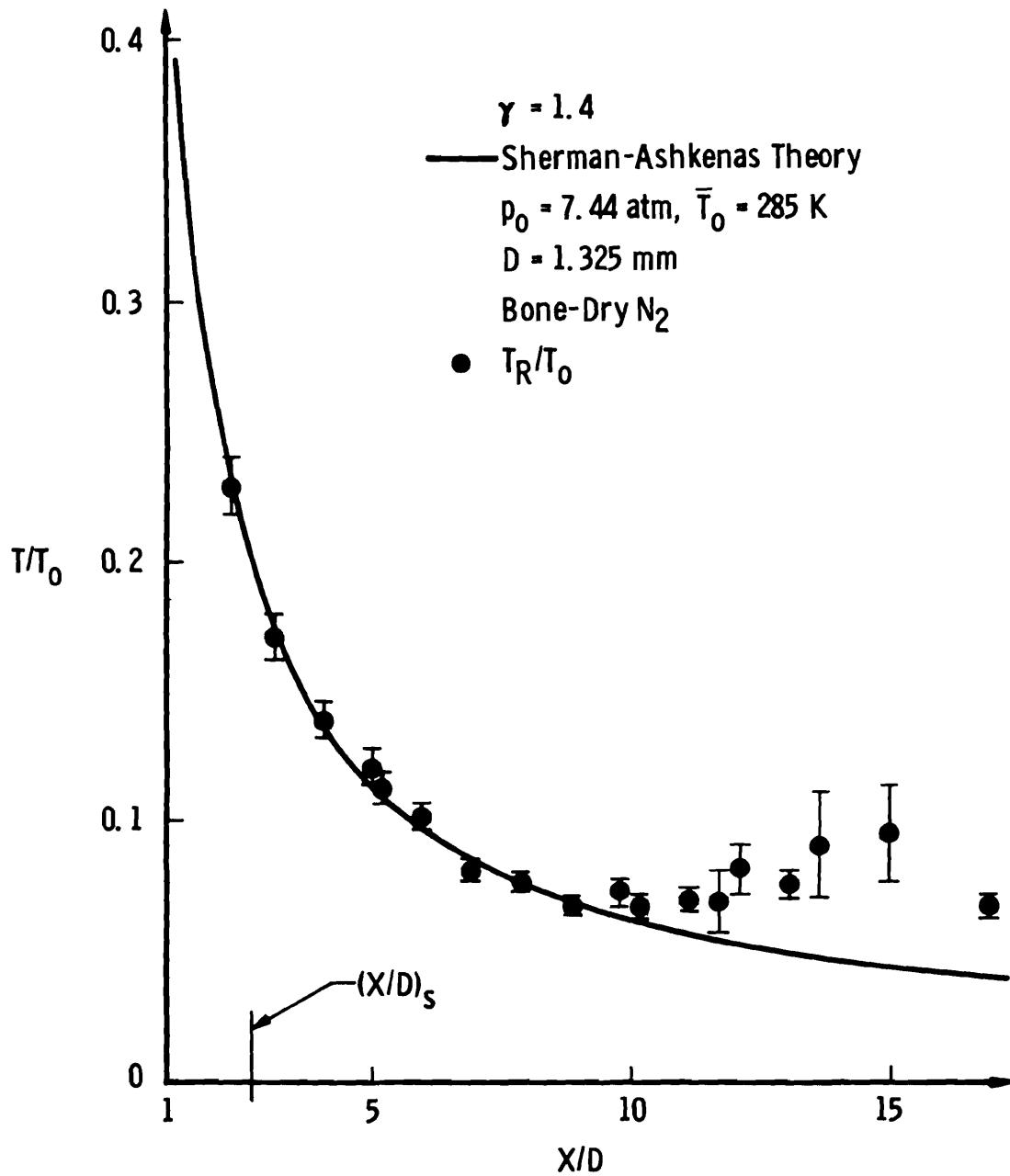


Figure 33. Axial variation of  $T_R/T_0$  for a free-jet nitrogen flow with  $P_0 = 7.44 \text{ atm}$ .

The height of the error bars indicate the 2-sigma error calculated by PROGRAM RATROT, and the width of the error bars indicate possible positional error. For  $X/D$  values less than 9, there is excellent agreement between the measured values and values calculated using the Ashkenas-Sherman equations (Ref. 8). For  $P_0$  values of 5.58 and 7.44 atm, the measured rotational temperatures show a significant increase over the calculated values for  $X/D$  greater than 9. For these high pressures and axial positions, Rayleigh scattering measurements have shown massive condensation taking place (Refs. 9 and 10). The effects of condensation will be discussed in Section 4.0. The lowest number density at which measurements were made was  $4.52 \times 10^{16} \text{ cm}^{-3}$ .

Figures 34 and 35 show typical CO and O<sub>2</sub> rotational Raman spectra taken in the sonic orifice flow field. The spectrometer scan rate for the CO spectra was 0.1 nm/min with a 10-sec time constant, and slit widths were 150-200-150  $\mu\text{m}$ . The axial variation of the CO rotational temperatures for  $P_0 = 3.72$  atm is shown in Fig. 36. The scan rate for the O<sub>2</sub> spectra was 0.2 nm/min with a 5-sec time constant, and slit widths were 200-200-200  $\mu\text{m}$ . Axial variation of O<sub>2</sub> rotational temperature is shown in Fig. 37. Again, there is excellent agreement between measured and calculated temperatures for both CO and O<sub>2</sub> for  $X/D < 7$ . However, for larger values of  $X/D$ , the measured rotational temperatures show a significant increase over the calculated values, and this effect also correlates with massive condensation as observed by Rayleigh scattering (Ref. 10) and discussed briefly in Section 4.0. The lowest number density at which temperature measurements were made was  $4.54 \times 10^{16} \text{ cm}^{-3}$  in O<sub>2</sub> and  $1.34 \times 10^{17} \text{ cm}^{-3}$  in CO.

Figures 38 and 39 show typical low temperature CO<sub>2</sub> rotational Raman spectra taken in the sonic flow. The spectrometer scan rate was 0.05 nm/min with a 5-sec time constant, and slit widths were 50-100-50  $\mu\text{m}$ . A limited axial variation ( $X/D < 4$ ) of the CO<sub>2</sub> rotational temperatures with  $P_0 = 0.7$  atm is shown in Fig. 40. There is no agreement with the predicted theoretical variation in this axial region for either  $\gamma = 7/5$  or  $9/7$ . Agreement was obtained with the electron beam results of Beylich (Ref. 11) using appropriate reservoir scaling laws (Ref. 12). The lowest number density at which CO<sub>2</sub> temperature measurements were made was  $7.97 \times 10^{16} \text{ cm}^{-3}$ .

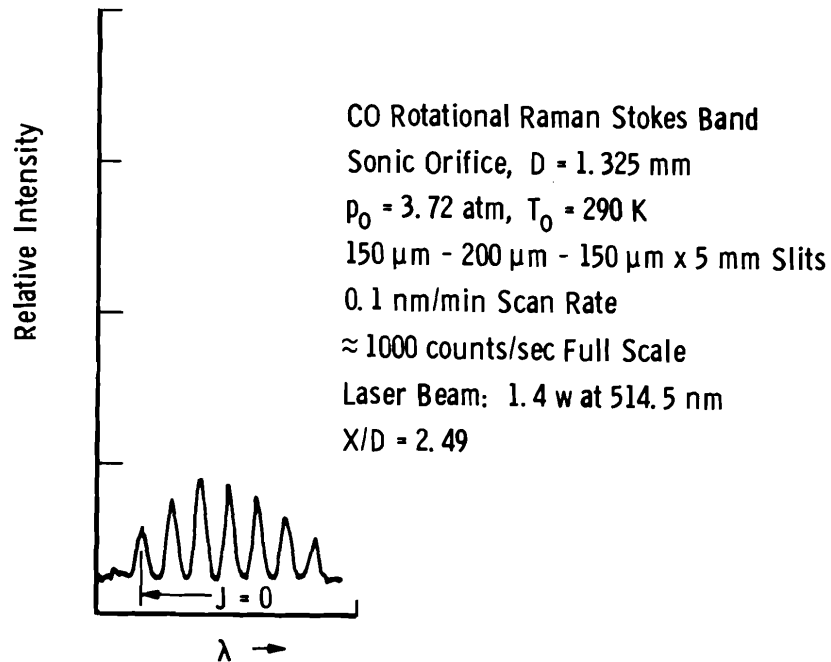


Figure 34. Typical low temperature pure rotational Raman spectrum of carbon monoxide in a hypersonic flow.

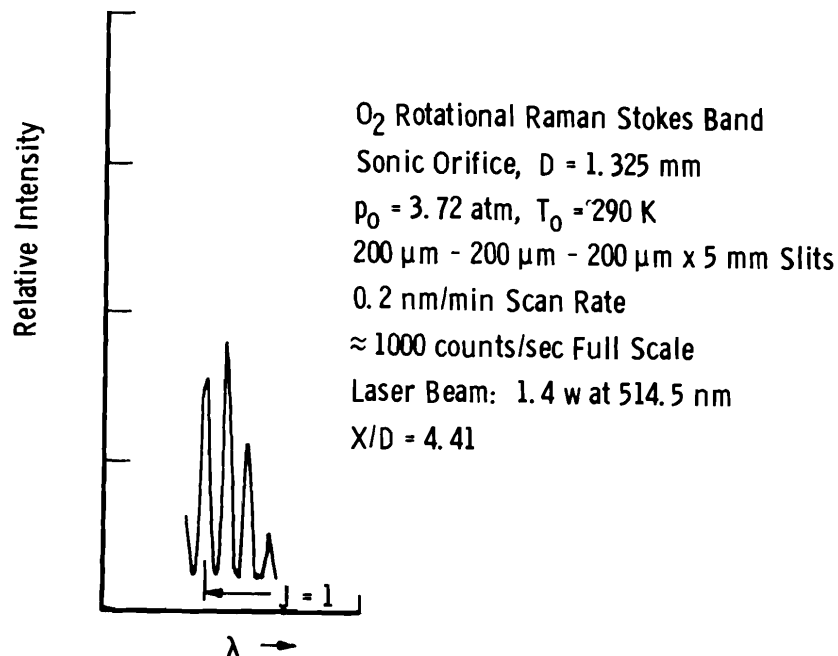


Figure 35. Typical low temperature pure rotational Raman spectrum of oxygen in a hypersonic flow.

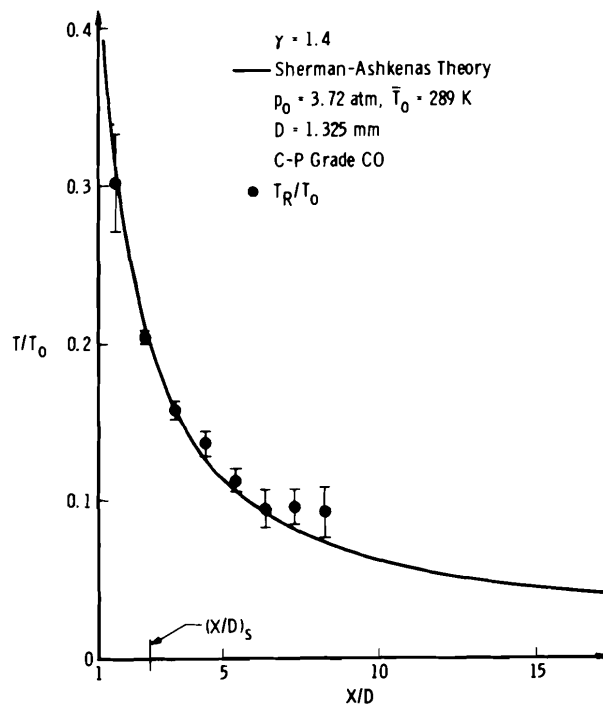


Figure 36. Axial variation of  $T_R/T_0$  for a free-jet carbon monoxide flow with  $P_0 = 3.72 \text{ atm}$ .

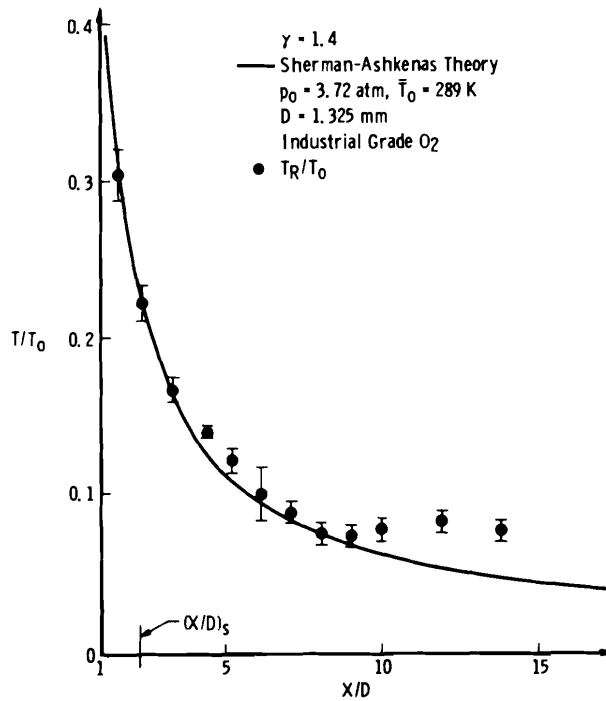


Figure 37. Axial variation of  $T_R/T_0$  for a free-jet oxygen flow with  $P_0 = 3.72 \text{ atm}$ .



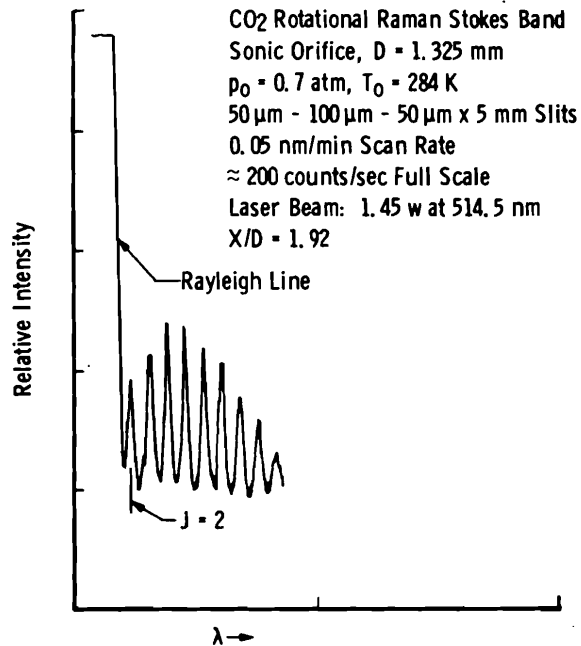


Figure 38. Typical low temperature pure rotational Raman spectrum of carbon dioxide in a hypersonic flow.

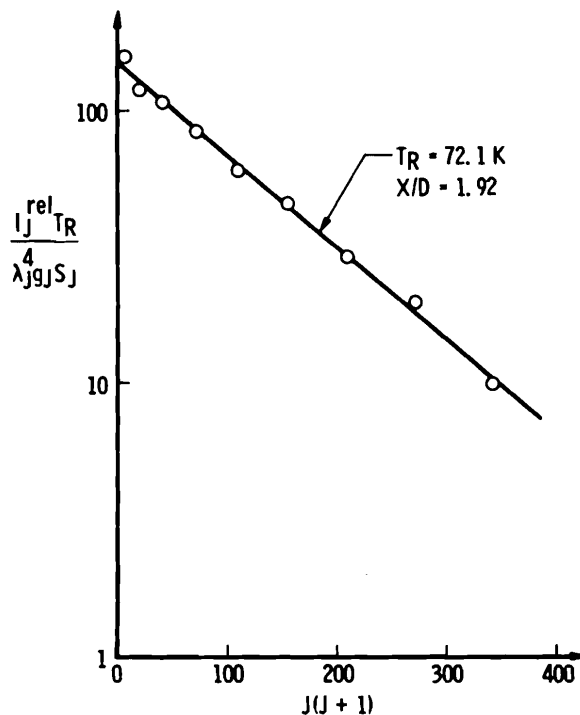


Figure 39. Boltzmann plot of pure rotational Raman line intensities from Fig. 38.

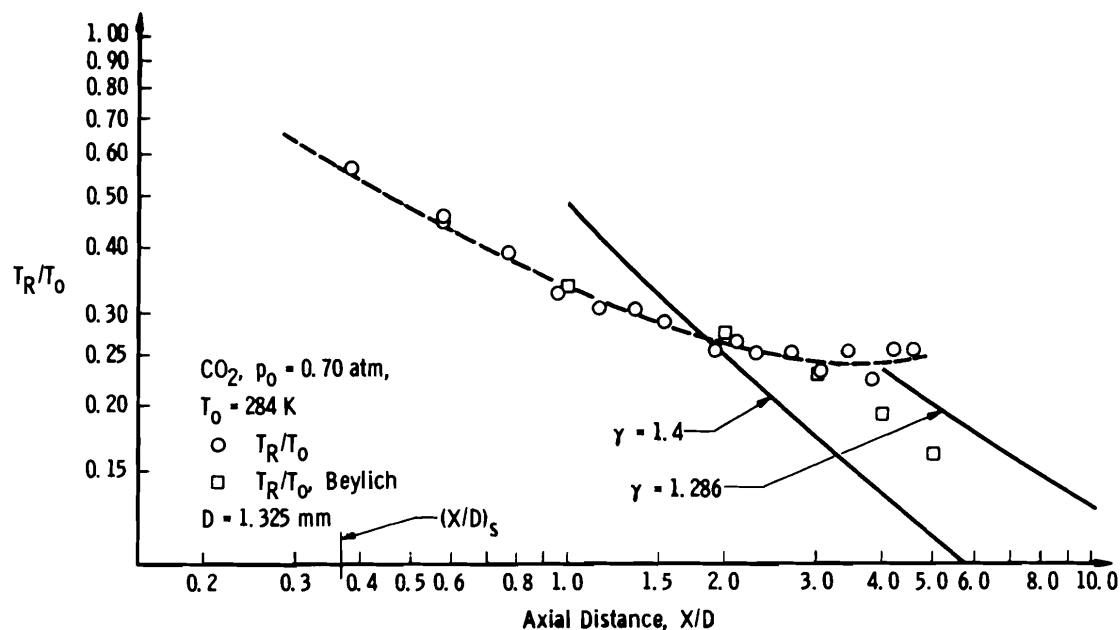


Figure 40. Axial variation of  $T_R/T_0$  for a free-jet carbon dioxide flow with  $P_0 = 0.70 \text{ atm}$ .

Measurements of axial variations of both rotational temperature and molecular number density were made in the  $\text{N}_2$  flow field of the conical nozzle for  $P_0$  values of 3.41, 6.82, and 10.2 atm. The results are shown in Figs. 41 through 46. The number density measurements are in excellent agreement with the MOC calculation of the flow-field density over the entire  $X_t/D_t$  range of measurements. For the  $P_0 = 3.41 \text{ atm}$  condition, the measured rotational temperatures are in good agreement with the MOC calculated temperatures over the entire  $X_t/D_t$  range of measurements. Significant increases of measured rotational temperature over the calculated values are observed in regions of massive condensation as determined from Rayleigh scattering (Refs. 10 and 12) for the  $P_0 = 6.82$  and 10.2 atm conditions. The lowest density at which temperatures were measured was  $2.31 \times 10^{16} \text{ cm}^{-3}$ .

Measurements of radial variations of both rotational temperature and molecular number density were made at axial positions of  $X_t/D_t = 12.47$  and 19.79 for the  $P_0 = 10.2 \text{ atm}$  condition. Results are shown in Figs. 47 through 50. Number density measurements are in good agreement with the calculated radial profiles. However, the rotational temperature radial profiles are in significant disagreement with the calculations. Even though condensation may be only moderate

on the centerline, Rayleigh scattering measurements (Ref. 10) have shown more condensation off the centerline at these axial positions, and this may well explain the higher-than-calculated temperatures at positions off the centerline.

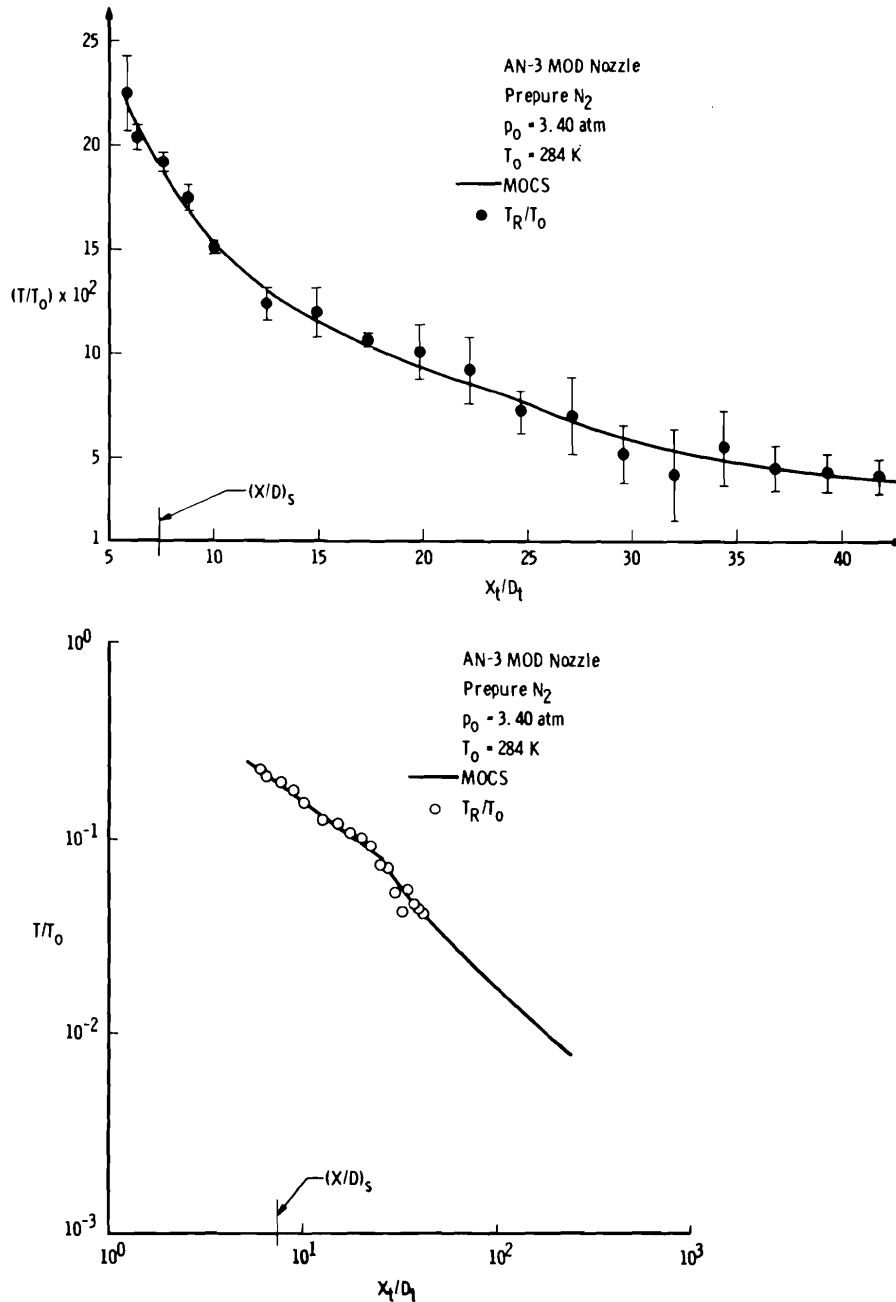


Figure 41. Axial variation of  $T_R/T_0$  for a conical nozzle nitrogen flow with  $P_0 = 3.40$  atm.

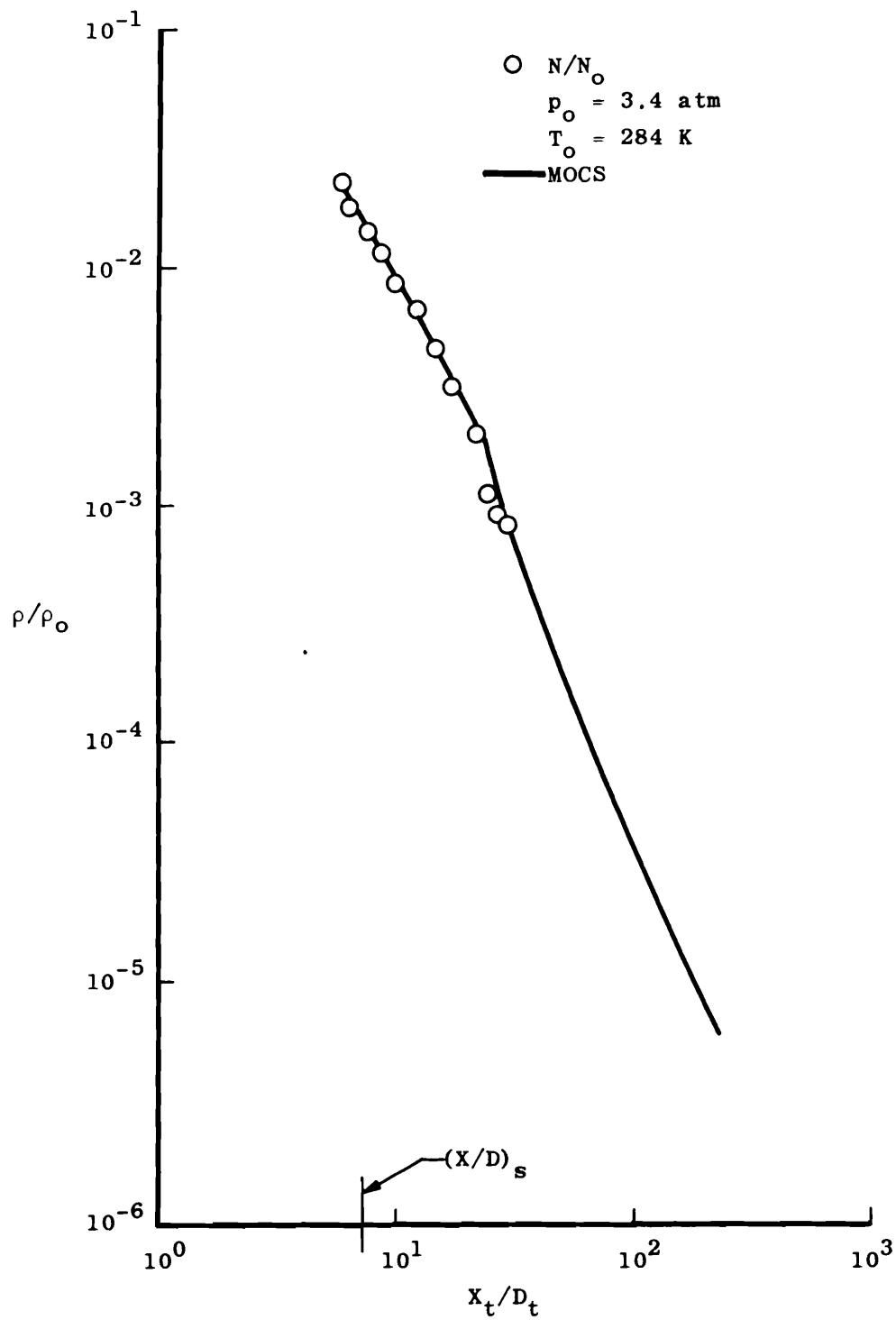


Figure 42. Axial variation of  $\rho/\rho_o$  for a conical nozzle nitrogen flow with  $P_o = 3.40 \text{ atm}$ .

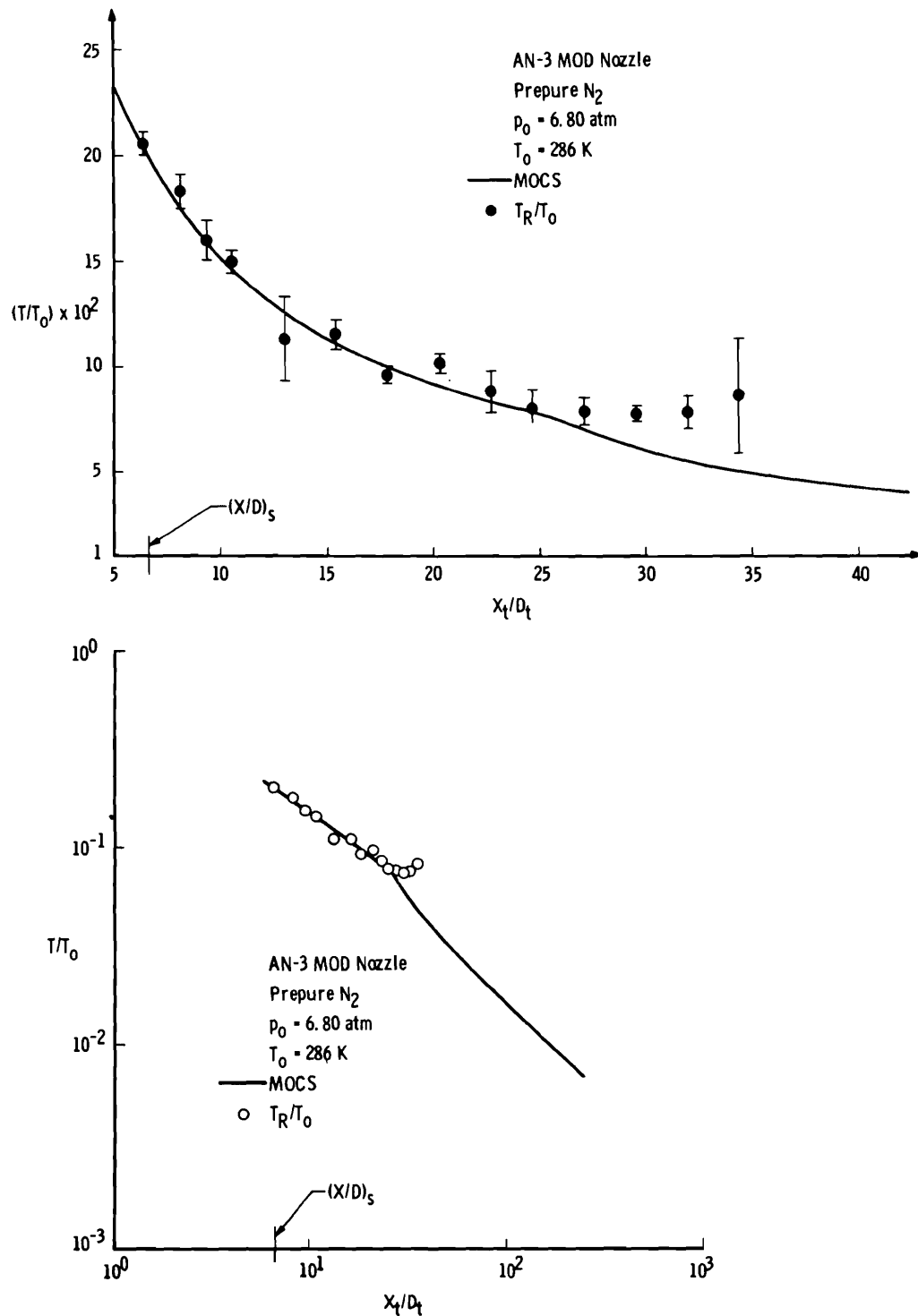


Figure 43. Axial variation of  $T_R/T_0$  for a conical nozzle nitrogen flow with  $P_0 = 6.80$  atm.

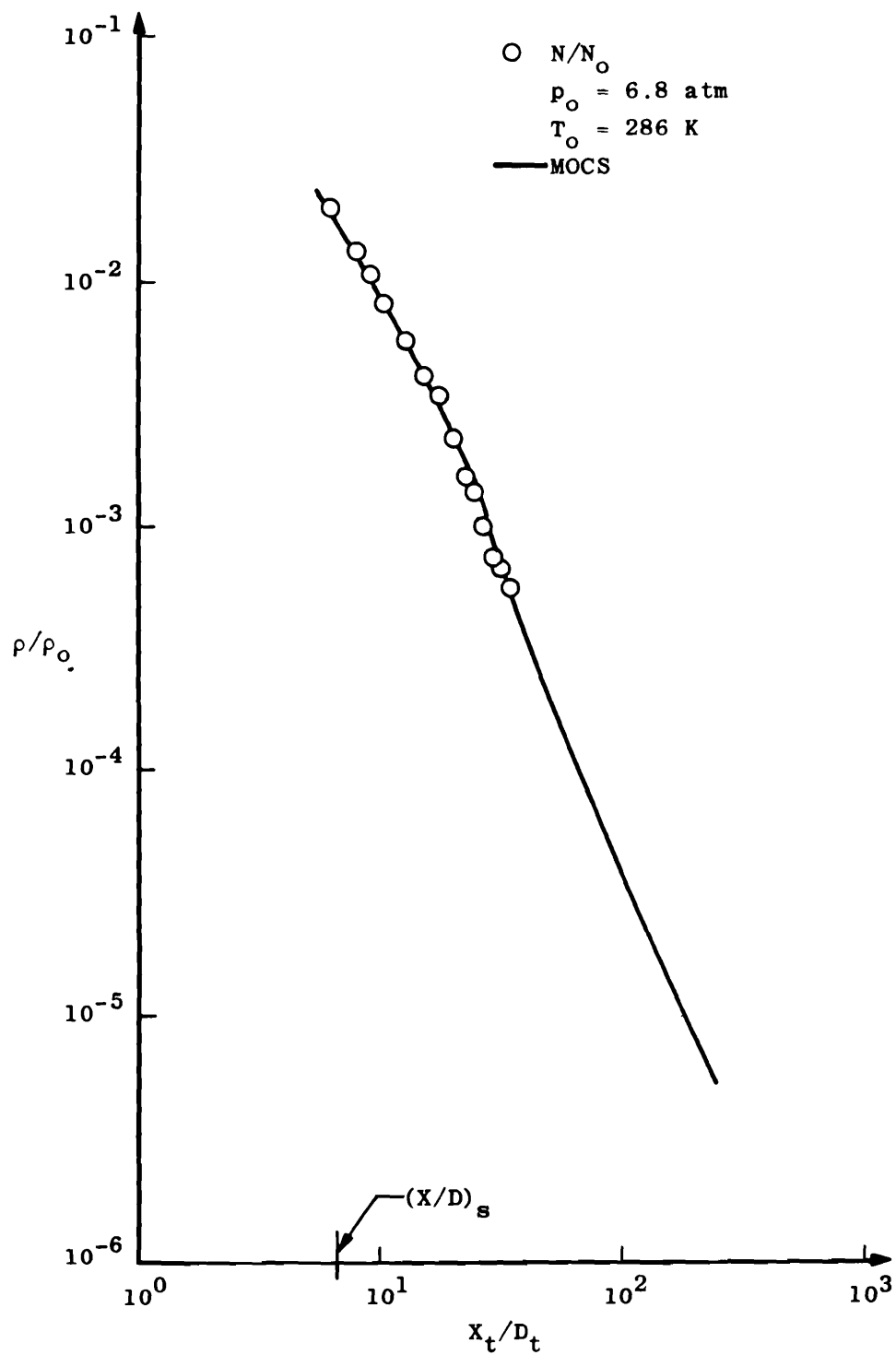


Figure 44. Axial variation of  $\rho/\rho_o$  for a conical nozzle nitrogen flow with  $P_o = 6.80 \text{ atm}$ .

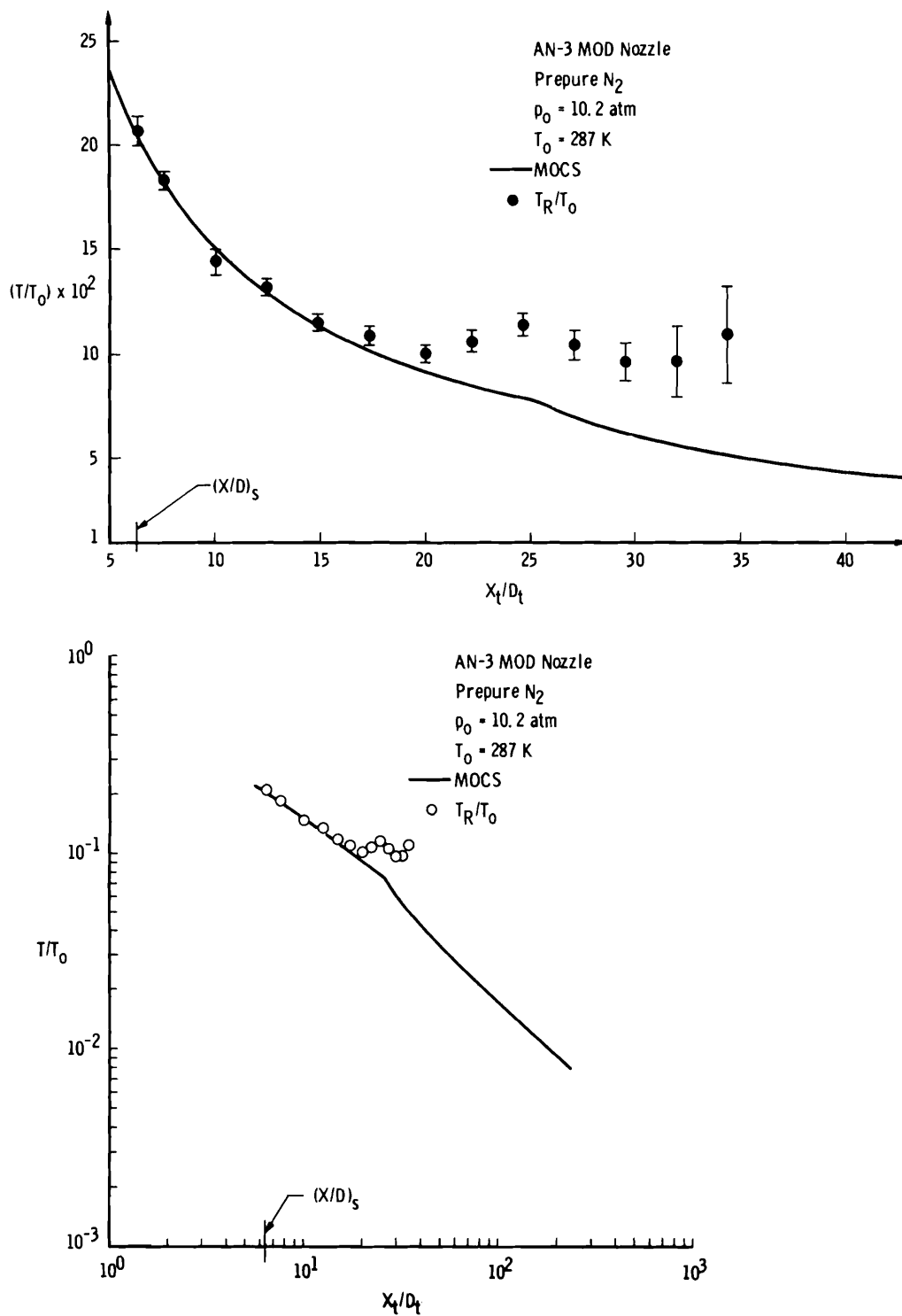


Figure 45. Axial variation of  $T_R/T_0$  for a conical nozzle nitrogen flow with  $P_0 = 10.2$  atm.

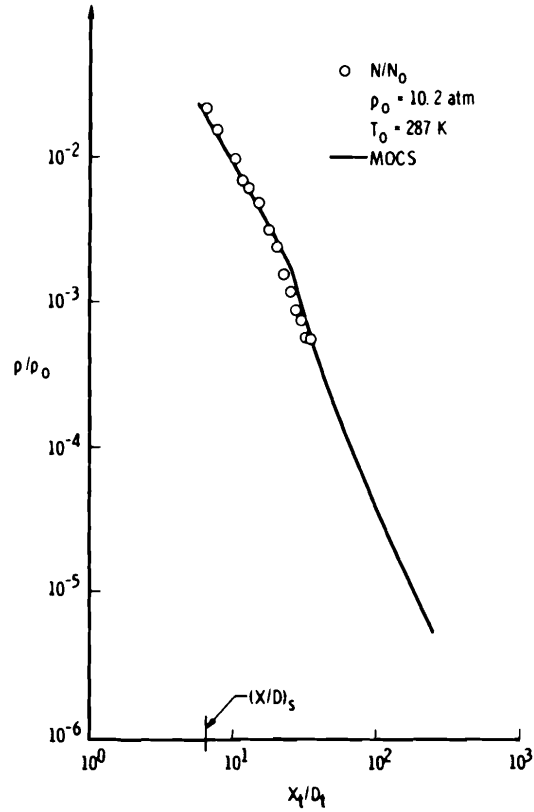


Figure 46. Axial variation of  $\rho/\rho_0$  for a conical nozzle nitrogen flow with  $P_0 = 10.2 \text{ atm}$ .

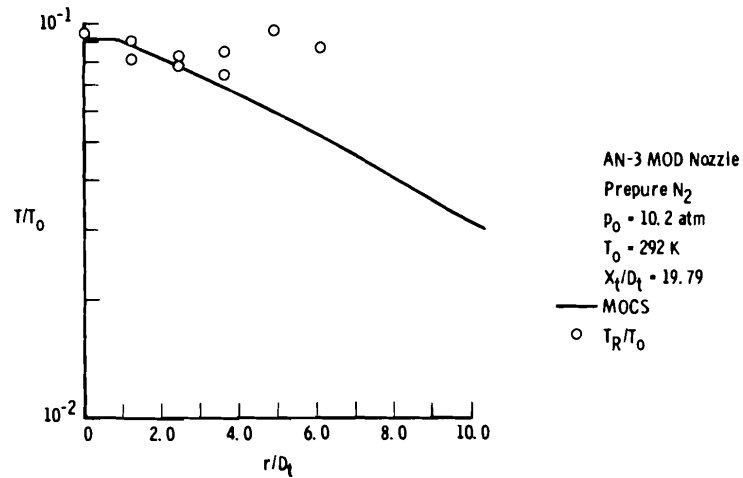
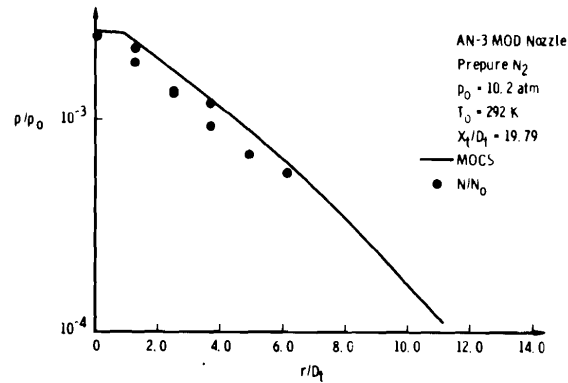
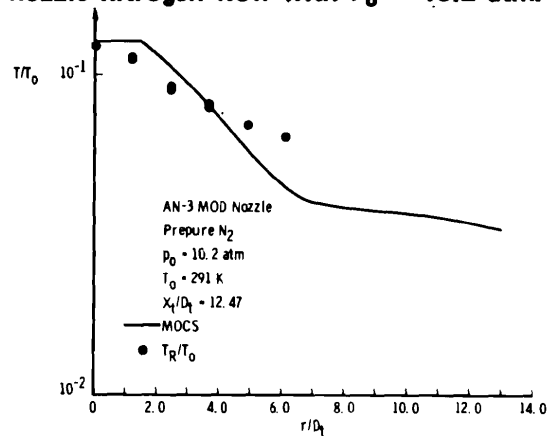


Figure 47. Radial variation of  $T_R/T_0$  at  $X_t/D_t = 19.79$  for a conical nozzle nitrogen flow with  $P_0 = 10.2 \text{ atm}$ .





**Figure 48.** Radial variation of  $\rho/\rho_0$  at  $X_t/D_t = 19.79$  for a conical nozzle nitrogen flow with  $P_0 = 10.2 \text{ atm}$ .



**Figure 49.** Radial variation of  $T_R/T_0$  at  $X_t/D_t = 12.47$  for a conical nozzle nitrogen flow with  $P_0 = 10.2 \text{ atm}$ .

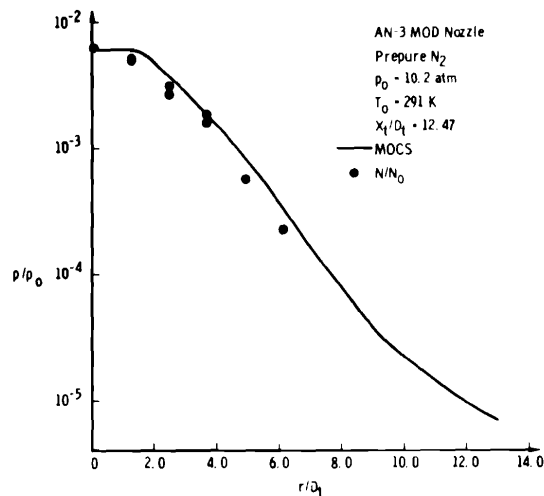


**Figure 50.** Radial variation of  $\rho/\rho_0$  at  $X_t/D_t = 12.47$  for a conical nozzle nitrogen flow with  $P_0 = 10.2 \text{ atm}$ .

## 4.0 ANALYSIS AND DISCUSSION

### 4.1 MOLECULAR PARTITION FUNCTIONS

Preliminary to the analysis and discussion of the results for Raman diagnostics of the flow fields studied, the previously mentioned approximation of replacing  $q_r$  with a function linear in  $T_R$  will be discussed. The approximation of Eq. (7) is actually twofold: the replacement of the summation over the discrete rotational quantum number  $J$  by  $kT_R/(\sigma B_0 hc)$  and, secondly, neglect of nuclear spin degeneracy factors. The first of these two is relevant to both homonuclear and heteronuclear diatomic molecules, while the second is important only for homonuclear species, assuming a nonreacting flow field. For completeness, the spin factors will be included for both types of diatomic species.

First, consider a heteronuclear specie AB for which the atomic constituents A and B have nuclear spins  $I_A$  and  $I_B$ , respectively. Since the spin degeneracy factor is  $(2I_A + 1)(2I_B + 1)$ , the quantum mechanical partition function  $q_r^{QM}$  is given by

$$q_r^{QM} = (2I_A + 1)(2I_B + 1) \sum_J \bar{g}_J \exp[-J(J + 1)\theta_R/T_R] \quad (13)$$

where

$$\theta_R = B_0 hc/k$$

is defined as the characteristic rotational temperature

and

$$\bar{g}_J = 2J + 1$$

Since  $B_0$  varies as the reciprocal of the moment of inertia of the specie,  $\theta_R$  increases as the specie reduced mass decreases. The classical limit C1 of  $q_r^{QM}$  is given by the limit at  $T_R/\theta_R \rightarrow \infty$ , or

$$q_r^{C1} = (2I_A + 1)(2I_B + 1) \times T_R/\theta_R \quad (14)$$

It is to be noted that molecular rotation-vibration interactions have been neglected so as to allow writing  $B_0$  for the molecular rotational constant. This neglect is not serious. Since

$$N_J/N_g = (2I_A + 1)(2I_B + 1) \times \bar{g}_J \exp[-J(J + 1)\theta_R/T_R]/q_r^{QM} \quad (15)$$

the classical limit is given by

$$\lim_{T_R/\theta_R \rightarrow \infty} (N_J/N_g) = \bar{g}_J \exp[-J(J + 1)\theta_R/T_R]/(T_R/\theta_R) \quad (16)$$

Therefore, as expected, the nuclear spin factors are eliminated for a nonreacting sample, and one can effectively use  $T_R/\theta_R$  as the partition function for relative number density calculations, as was done in Eq. (7).

For homonuclear species, the same considerations will apply insofar as replacing the summation of  $q_r^{QM}$  by a simple function of  $T_R$ , but nuclear spin statistics assumes a much more important and visible role. Since the high temperature ratio of ortho- to para-molecular species is assumed to be retained during the expansion process, one must regard the gas as a mixture of two inconvertible species. The partition functions for the ortho-specie  $q_r^{QM(o)}$  and the para-specie  $q_r^{QM(p)}$  are given by

$$q_r^{QM(o)} = (2I_A + 1)(I_A + 1) \Sigma' \bar{g}_J \exp[-J(J + 1)\theta_R/T_R] \quad (17)$$

and

$$q_r^{QM(p)} = (2I_A + 1)(I_A) \Sigma'' \bar{g}_J \exp[-J(J + 1)\theta_R/T_R] \quad (18)$$

where  $\Sigma'$  designates summing over (even  $J$ ; odd  $J$ ) integers if  $(-1)^{a\bar{P}}$  is  $(+1; -1)$  and  $a$  is the nucleon number of the atomic constituent and  $\bar{P}$ , the electronic parity eigenvalue, is  $\pm 1$ . Then,  $\Sigma''$  denotes summing over the remaining integer set. Since the following are true,

$$\lim_{T_R/\theta_R \rightarrow \infty} \Sigma' \bar{g}_J \exp[-J(J + 1)\theta_R/T_R] = \lim_{T_R/\theta_R \rightarrow \infty} \Sigma'' \bar{g}_J \exp[-J(J + 1)\theta_R/T_R] = T_R/2\theta_R \quad (19)$$

the high temperature equilibrium partition function  $q_r^{QM}(E)$  is

$$q_r^{QM}(E) = \left\{ (2I_A + 1)^2 \sum_J \bar{g}_J \exp [-J(J + 1)\theta_R/T_R] \right\}^{1/2} \quad (20)$$

and

$$\lim_{T_R/\theta_R \rightarrow \infty} q_r^{QM(o)} = (2I_A + 1)(I_A + 1)(T_R/2\theta_R) \quad (21)$$

$$\lim_{T_R/\theta_R \rightarrow \infty} q_r^{QM(p)} = (2I_A + 1)I_A(T_R/2\theta_R) \quad (22)$$

one finds the high temperature ortho- and para-number density distributions to be

$$\lim_{T_R/\theta_R \rightarrow \infty} [N_J(o)/N_g] = 2\theta_R \left( \frac{I_A + 1}{2I_A + 1} \right) \bar{g}_J \exp [-J(J + 1)\theta_R/T_R]/T_R \quad (23)$$

and

$$\lim_{T_R/\theta_R \rightarrow \infty} [N_J(p)/N_g] = 2\theta_R \left( \frac{I_A}{2I_A + 1} \right) \bar{g}_J \exp [-J(J + 1)\theta_R/T_R]/T_R \quad (24)$$

respectively. Obviously, the factor  $2\theta_R/(2I_A + 1)$  of the preceding equations is of no consequence for calculation of the relative number density or intensity distribution, but the spin-dependent factors do influence the observed scattered intensity distribution. For  $N_2$ ,  $(-1)^{a\bar{P}}$  is +1 so even  $J$  molecules are ortho species and odd  $J$  are para.  $I_A$  is 1 so even  $J$  states are twice as prevalent as odd  $J$  species, and the observed intensity data for odd  $J$  scattering have been multiplied by  $(I_A + 1)/I_A = 2$  to allow for spin statistics. For  $O_2$ , since  $I_A$  is zero and  $\bar{P}$  is -1, only ortho species exist and scattering from even  $J$  is absent. Similar considerations apply for  $CO_2$  as for  $O_2$ .

After having determined the high temperature limit of the number density distribution, it now remains only to define what constitutes for practical purposes a high-temperature limit.

Figure 51 shows the temperature variation of the ratio  $Q_{EO}$  of the summation of  $\bar{g}_J \exp [-J(J + 1)\theta_R/T_R]$  over even and odd  $J$  values; obviously, the approach of this ratio to within the experimental precision

value of unity defines the high-temperature limit of the particular measurement. It is seen that, for  $T_R/\theta_R \approx 4$ ,  $Q_{EO}$  deviates from unity by less than 1 part per thousand. Therefore, by defining the high-temperature limit as  $T_R/\theta_R = 4$ , the molecular constants of Table 1 show that the approximation of Eq. (7) is valid for  $N_2$ ,  $O_2$ ,  $CO_2$ , and  $CO$ , so long as  $T_R > 11.4$ ,  $8.3$ ,  $2.2$ , and  $11.1$  K, respectively. These restrictions are satisfied for the present study. It should be noted that for  $H_2$ , although not included in this work,  $\theta_R = 85.4$  K so  $T_R$  must be greater than  $341.6$  K to use the classical value of  $q_r$ . Since isotopic species  $A^{a_1}A^{a_2}$ ,  $a_1 \neq a_2$ , are heteronuclear, the ortho-para distinction disappears and the even-odd  $J$  ratio assumed previously is no longer valid. However, since both the  $O^{16}:O^{18}$  ratio and the  $N^{14}:N^{15}$  ratio exceed 100:1 no isotopic specie correction is applied to the previously derived intensity equations.

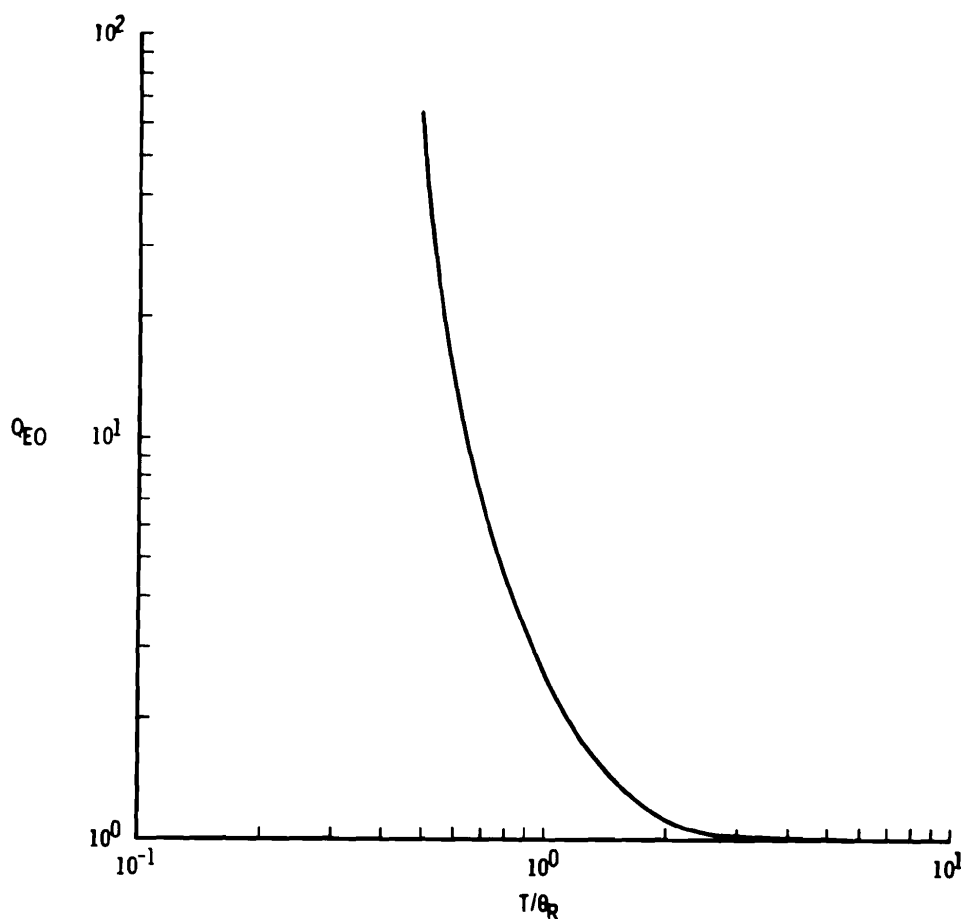


Figure 51. Temperature variation of the ratio  $Q_{EO}$ .

## 4.2 CONDENSATION, RELAXATION, AND THEIR EFFECTS

Excluding at present vibrational relaxation processes, the only significant source of free-stream anisotropy is that of condensation. Obviously, for a gas expanding from a source of unsaturated reservoir parameters, some region of the flow field must be unsaturated and, hence, uncondensed. The task at hand is to determine the spatial regions of the flow field for which condensation is not possible and for which the calculated flow parameters should agree with the measured values. For an isentropic expansion, it is known that the static pressure  $P$  varies as

$$P = P_o(T/T_o)^{\gamma/(\gamma-1)} \quad (25)$$

and  $\gamma$  is assumed constant. Consequently, as Fig. 52 shows, the expansion definitely proceeds isentropically in the  $P$ - $T$  plane until intersection of the vapor pressure curve. The saturation temperature  $T_s$  is then used, in the form of  $T_s/T_o$ , with the results of either Ashkenas-Sherman or the MOCS to determine the axial location of saturation  $(X/D)_s$ , prior to which point the flow field is definitely uncondensed and beyond which point the flow field is supersaturated but not necessarily condensed. The vapor pressure-temperature data of Hilsenrath, et al. (Ref. 13), were used for all species studied except  $\text{CO}_2$  for which the data of Honig and Hook (Ref. 14) were used. The saturation locations  $(X/D)_s$  so obtained are shown on the appropriate figures displaying the experimental results of this work.

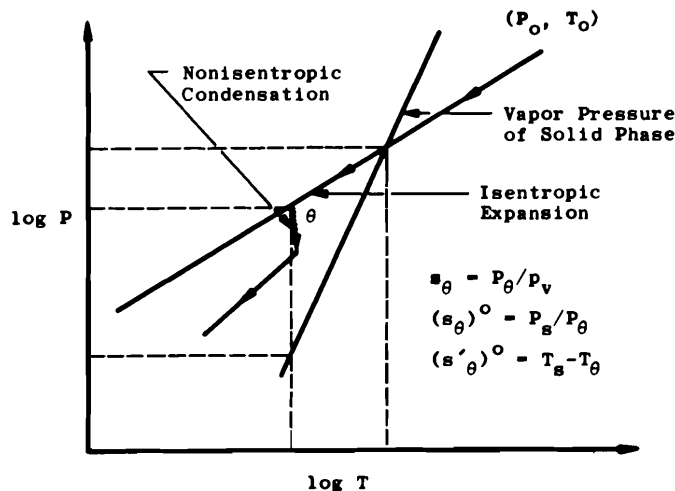


Figure 52. Diagram of expansion process in  $P$ - $T$  plane.

Since the condensation process itself is not the subject of this work and is discussed elsewhere (Refs. 9 and 12), only the manifestation of the phenomenon as it influences this work will be considered. The axial profiles of the  $T_R/T_O$  results for  $N_2$  sonic orifice expansions, as shown in Figs. 30 through 33, exhibit varying degrees of agreement with the theoretical predictions. It is seen that, for  $X/D < (X/D)_S$ , the agreement of the data with the prediction of Ref. 8 is excellent. For  $X/D > (X/D)_S$ , the agreement with theory of the  $P_O = 2.7$  atm expansion results of Fig. 30 is good, but, as Figs. 31 through 33 show, the deviation of measured and predicted values increases as  $P_O$  increases, and this increase in the measured values of  $T_R/T_O$  obviously results from the heat release to the gas due to the exothermic combination of molecules in the condensation process, and the magnitude of this increase is dependent on condensate mass fraction. Previous Rayleigh scattering results (Ref. 9) have shown that condensation onset and cluster growth have indeed occurred for the flow fields of Figs. 30 through 33 prior to detection of increases in  $T_R$ . This is not unexpected since it has been found that the Rayleigh scattering measurements are, in general, at least an order of magnitude more sensitive with respect to condensate mass fraction than is the rotational temperature measurement. Identical considerations apply to the  $O_2$  and  $CO$  results of Figs. 36 and 37.

Although the sonic orifice  $CO_2$  results of Fig. 40 have been presented previously (Ref. 12), the  $T_R$  data are included here for completeness and additional analysis. From Fig. 40, it is seen that  $T_R$  of  $CO_2$  was measured over the axial distance range  $0.38 \leq X/D \leq 4.6$ . The agreement with the electron beam results of Beylich is to be noted.

Also shown in Fig. 40 are the predictions of Ref. 8 for the self-similar axial dependence of expansions for gases of  $\gamma = 7/5$  and  $9/7$ . It is noted that the axial region of validity of the predictions for  $\gamma = 7/5$  and  $9/7$  is  $X/D \geq 1.0$  and  $4.0$ , respectively. Obviously, our data show no agreement with these predictions. To determine if condensation exists for this particular sonic orifice expansion, we have used unpublished isentropic  $CO_2$  density data using Rayleigh scattering for both 3.0- and 1.325-mm orifice diameter expansions, and Fig. 53 shows these results when plotted in the  $N$ - $T$  plane. It is seen that  $\gamma = 1.44$  fits the isentropic portion of the expansion and that deviation from the  $\gamma = 1.44$  curve occurs for  $T_R/T_O \approx 0.33$ . This indication of condensation occurs at the spatial location of  $X/D \approx 1.0$ , as shown in Fig. 40, beyond which elevated  $CO_2$  temperatures may be expected.

Now, using  $\gamma = 1.44$ , the  $\text{CO}_2$  expansion is plotted in the P-T plane along with its vapor pressure data, and saturation is found to occur at  $T_R/T_0 = 0.57$  which is estimated from Fig. 40 to occur at  $(X/D)_S = 0.38$ . Consequently,  $\text{CO}_2$  expands isentropically from  $X/D \approx 0.4$  until reaching an  $X/D \approx 1$  before condensation onset occurs, and, assuming a constant value for  $\gamma$  and isentropic flow for the axial region  $0.4 \lesssim X/D \lesssim 1$ , one may calculate the axial dependence of the Mach number  $M$  using the well-known relation:

$$T/T_0 = \{1 + [(\gamma - 1)/2]M^2\}^{-1} \quad (26)$$

and the result is shown in Fig. 54.

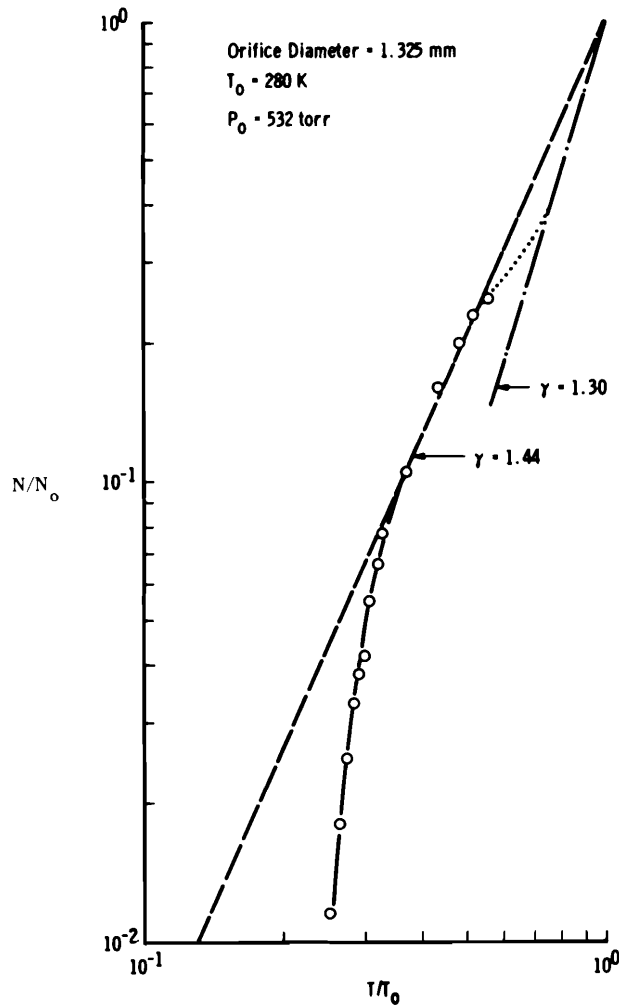


Figure 53.  $\text{CO}_2$  Rayleigh scattering in the N-T plane,  $\gamma = 1.44$ .



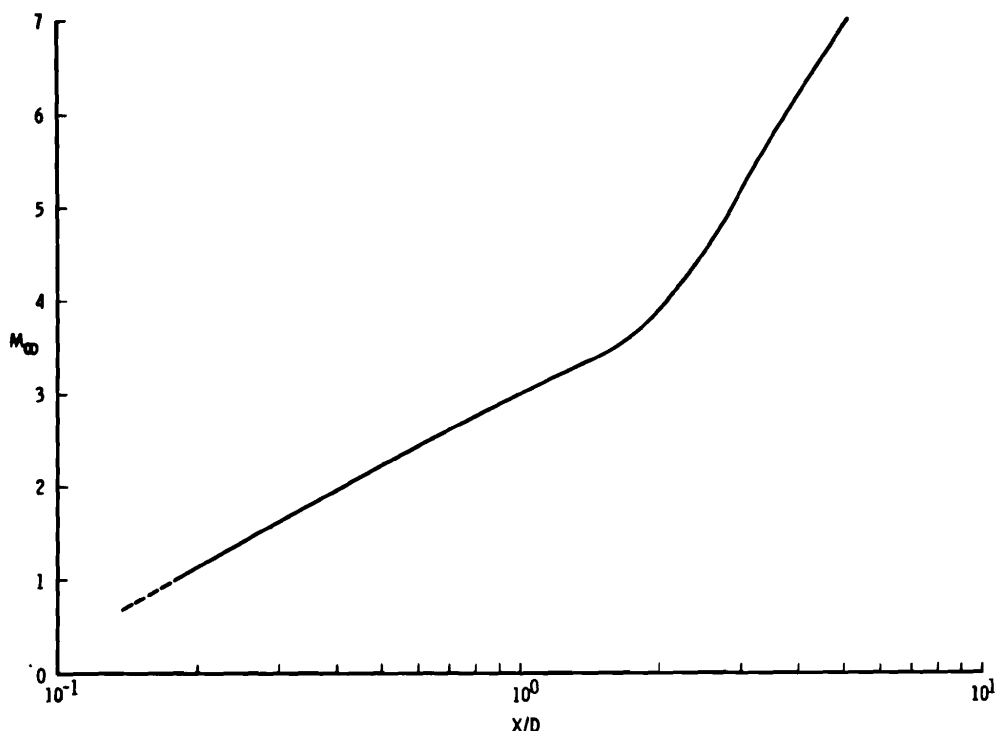


Figure 54. Axial variation of Mach number for CO<sub>2</sub>.

It is interesting to compare the measured value of  $\gamma = 1.44$  with the value of the specific heat ratio of CO<sub>2</sub> if equilibrium flow occurred. Since CO<sub>2</sub> has four vibrational modes, one of which is twofold degenerate, and these modes, particularly the deformation mode, are partially excited at 284 K, one finds  $\gamma$  of CO<sub>2</sub> for this reservoir temperature to be 1.295. Figure 55 shows the variation with temperature of  $\gamma$  of CO<sub>2</sub> where, for this calculation, it has been assumed that the vibrational modes are in equilibrium with themselves and the translational and rotational degrees of freedom. It is seen that  $\gamma = 1.4$  is the equilibrium value for the temperature region  $T \lesssim 110$  K.

The effects of nonideality of CO<sub>2</sub> on the equilibrium specific heat ratio can be obtained using the equation of state of the gas. For this purpose, the axial profile of the static pressure ratio for the CO<sub>2</sub> expansion was calculated using the results of Fig. 53, and using the corresponding values of temperature and the virial coefficient data for the Lennard-Jones (6-12) potential (Ref. 15), one finds non-ideal gas corrections to  $\gamma$  for the CO<sub>2</sub> expansion whose results are shown in

Fig. 40 to be on the order of 0.5 percent; the calculated values are shown in Fig. 55. It should be noted that the ideal gas values of  $\gamma$  for  $\text{CO}_2$  for  $T \geq 200$  K were obtained from Ref. 15 and the values for  $T < 200$  K were calculated using a simple harmonic oscillator model for each  $\text{CO}_2$  vibrational mode.

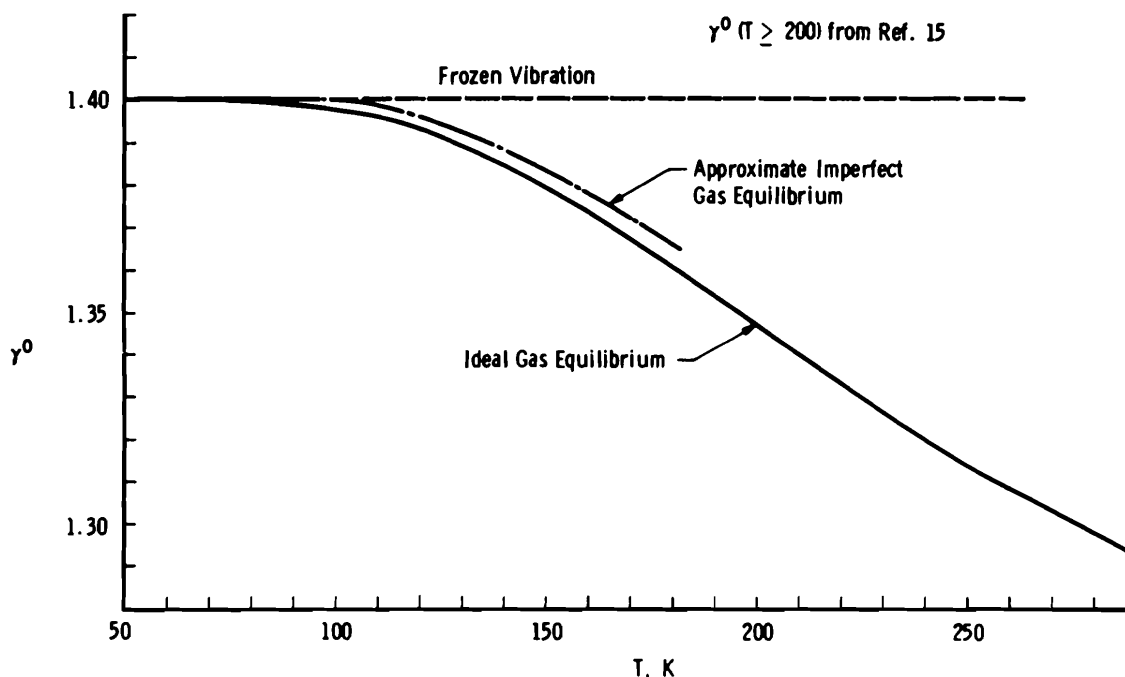


Figure 55. Variation of  $\gamma$  with temperature for  $\text{CO}_2$ .

Since the measured value of  $\gamma$  exceeds the equilibrium value for  $X/D < 1.0$ , as shown by Figs. 53 and 55, it is reasonable to expect that vibrational freezing has occurred. Further, since a constant  $\gamma = 1.44$  describes the expansion from  $X/D \geq 0.4$  to condensation onset, the vibrational freezing must have occurred prior to  $X/D \approx 0.4$ . To demonstrate analytically that this inference is reasonable would be reassuring. For such a demonstration,  $\Delta E_v(12)$  is defined as the vibrational energy of  $\text{CO}_2$  which must be transferred to the translational and rotational modes between axial positions  $(X/D)_1$  and  $(X/D)_2$  if the vibrational modes are to remain in equilibrium. Since the vibrational energy is concentrated in the deformation modes of  $\text{CO}_2$  for the temperatures of interest, the calculation of  $\Delta E_v(12)$  can neglect the symmetric and anti-symmetric valence modes of vibration. If  $\hbar\omega$  is the quantum energy of the deformation mode,  $\Delta E_v(12)/\hbar\omega$  can be interpreted by classical collision mechanics as the probability for transfer of a vibrational quantum between points  $(X/D)_1$  and  $(X/D)_2$ , subject to the restriction that  $\Delta E_v(12)/\hbar\omega \ll 1$ . The initial point  $(X/D)_1$  is chosen to be the reservoir,

and  $(X/D)_2$  is chosen to be 0.3. The vibrational energy for each position is calculated using the simple harmonic oscillator model of the deformation mode, and it is found that, between the reservoir and  $X/D = 0.3$ ,

$$\Delta E_v(12)/\hbar\omega = 2 \times 10^{-2} = p_v(12)$$

Next, one must calculate the probability  $p_v(12)$  of transfer of a vibrational quantum to occur between the axial points  $(X/D)_1$  and  $(X/D)_2$ . If  $Z_T(12)$  is the average total number of collisions which a molecule experiences between points  $(X/D)_1$  and  $(X/D)_2$  and  $Z_{10}$  is the number of collisions required for transfer of one vibrational quantum from vibrational levels 1 to level 0, the calculated probability of transfer  $p_{vc}(12)$  is

$$p_{vc}(12) \approx Z_T(12)/Z_{10} \quad (27)$$

If the molecule is described insofar as elastic collisions are concerned as a hard sphere of collision cross section  $(\sigma^2)$ , one can easily show that

$$Z_T(12) = 4N_o\sigma^2D\sqrt{\pi/\gamma} \int_{(X/D)_1}^{(X/D)_2} d(X/D)/M \{1 + [(\gamma - 1)/2]M^2\}^{-1/(\gamma-1)} \quad (28)$$

where all symbols have the usual meaning. One sees that  $M$  must be known as a function of  $X/D$ , but since this is essentially the problem being investigated, for order of magnitude purposes the axial variation of  $M$  for a  $\gamma = 1.4$  expansion is to be used. By using the sonic orifice density data for isentropic  $N_2$  expansions (Ref. 9), shown in Fig. 56, the axial variation of the Mach number was calculated assuming  $\gamma = 1.4$ , and Fig. 57 shows the results. With these results, the integrand ( $I_M$ ) and the integral of Eq. (28), defined as  $Z_T(12)$ , were determined and are shown in Fig. 58. By using the appropriate values of  $N_o$ ,  $\gamma$ ,  $\sigma^2$ , and  $D$ , it was found that  $Z_T(0, 0.3)$  was on the order of 4000 collisions.

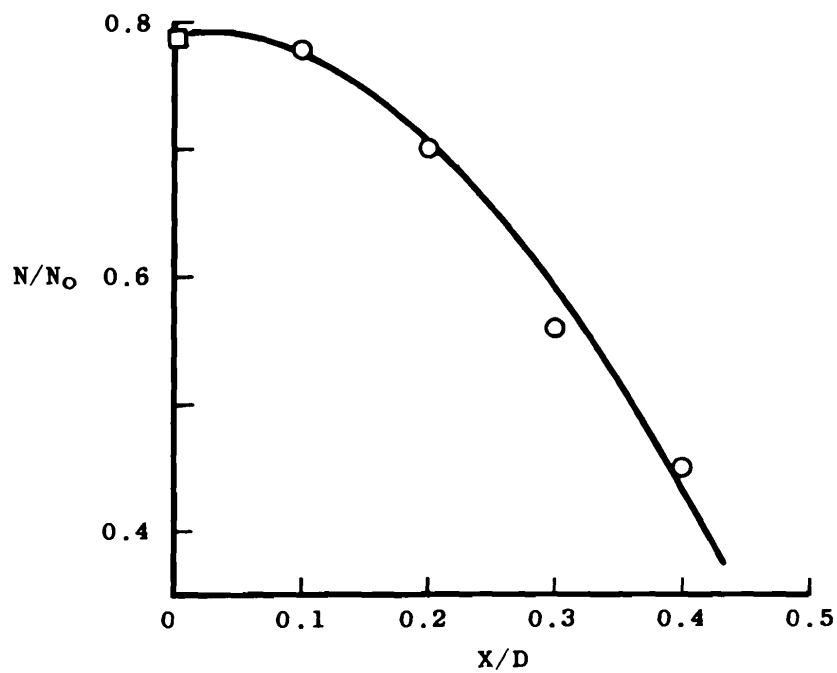


Figure 56. Axial variation of number density for  $\gamma = 1.4$  ( $N_2$ ).

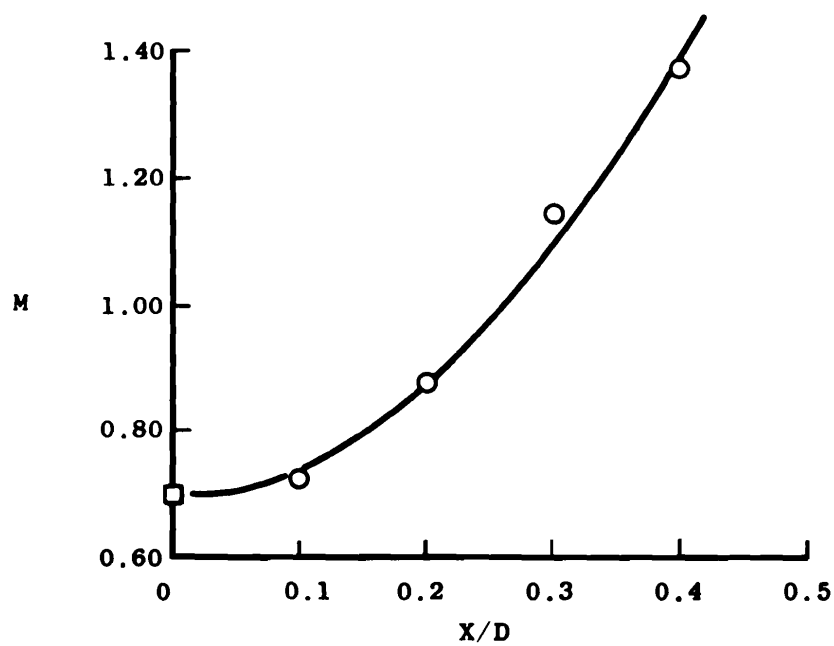


Figure 57. Axial variation of Mach number for  $\gamma = 1.4$  ( $N_2$ ).

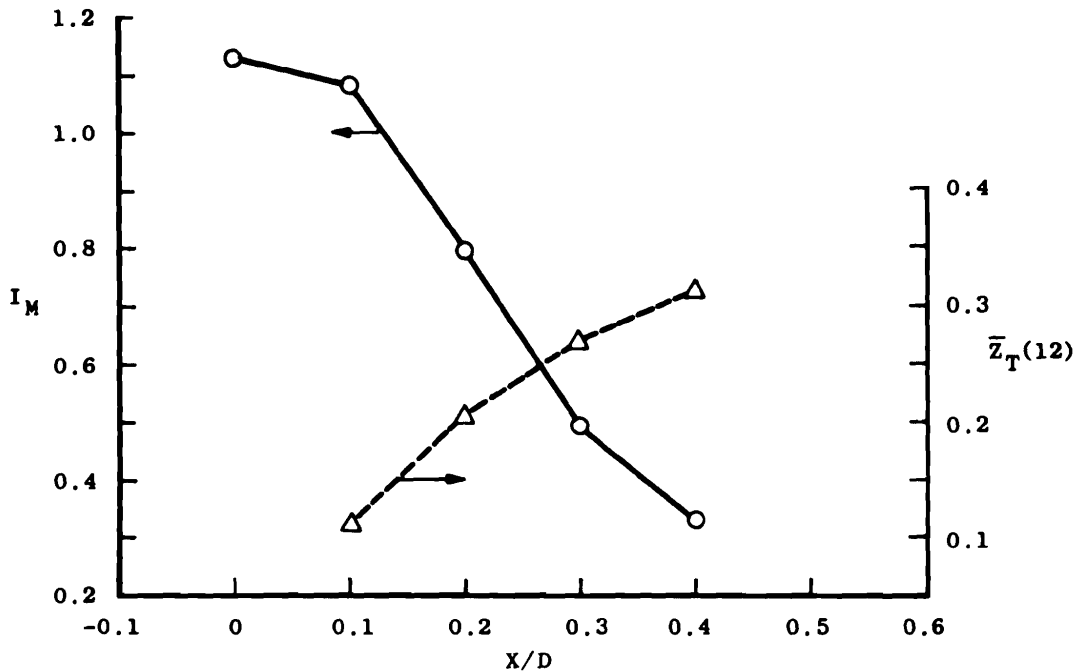


Figure 58. Axial variation of collision number integrand,  $I_M$ , and accumulative collision number function,  $\bar{Z}_T(12)$ ,  $\gamma = 1.4(N_2)$ .

To determine  $Z_{10}$ , the data of Cottrell and McCoubrey (Ref. 16) were used, as well as the Landau-Teller vibrational transfer theory (Ref. 16), to justify the use of an average value of  $Z_{10}$  of  $10^5$  over the axial distance range of interest. Therefore,

$$p_{VC}(12) \approx 4 \times 10^{-2}$$

and one sees that  $p_V(12)/p_{VC}(12) \sim 1$ . Consequently, it is expected that vibrational equilibrium may be maintained for the axial region  $0 \leq X/D \leq 0.3$ . It is most reasonable to believe that vibrational freezing does not occur at the orifice as the flow develops, but rather equilibrium or near-equilibrium is maintained to  $X/D \approx 0.2$  to  $0.3$ . Extending point 2 farther along the flow direction does not substantially increase the value of  $Z_T(X/D = 0, X/D)$ ; however, the average value of  $Z_{10}$ , which varies as  $\exp[-T^{-1/3}]$ , increases significantly, thereby decreasing  $p_{VC}(12)$ . Furthermore,  $\Delta E_V(12)$  increases as  $T$  as point 2 decreases, so the ratio  $p_V(12)/p_{VC}(12)$  which equals  $[\Delta E_V(12)/\hbar\omega]/[Z_T(12)/Z_{10}]$  increases significantly. Obviously, the meaning is that the inherent probability of transfer, as denoted by  $p_{VC}(12)$ , is inadequate to maintain equilibrium. Further discussion of  $CO_2$  expansions and condensation must await additional analysis.

From the sonic orifice expansion results for  $N_2$  (Figs. 30 through 33), CO (Fig. 36), and  $O_2$  (Fig. 37), it is seen that the Ashkenas-Sherman prediction for  $\gamma = 1.4$  is in excellent agreement with the experimental measurements for the unsaturated flow-field regions, and the onset of condensation as manifested by an increase in  $T_R$  due to the recombination heat release is obvious. Since the condensation is the subject of future reports, no further discussion is presented regarding this phenomenon. However, it is noted that the rotational Raman spectra exhibited a Boltzmann number density distribution for the rotational energy levels for both the uncondensed and condensed regions of the flow field, thereby demonstrating that local thermal equilibrium existed for the rotational mode of motion.

As Figs. 41 through 50 show, the conical nozzle expansion results for  $N_2$  density and rotational temperature along the centerline are in excellent agreement with the MOCS predictions as the flow is unsaturated. Once again, condensation onset is evidenced by an increase in  $T_R$  relative to the MOCS prediction, and Boltzmann distributions were observed to adequately characterize the rotational mode of  $N_2$ . It is to be noted in all the axial profile results that the expansion characteristics from the nozzle lip intersect the centerline at approximately  $X_t/D_t = 25$ . Figure 59 shows the two-dimensional axial-radial locus of the expansion characteristic, and obviously the gas exterior to the so-called "testing region" of the nozzle expands faster than that interior to the region, thereby resulting in an earlier saturation of the gas in the exterior region. Consequently, the spatial locus of saturation is three dimensional in nature and of cylindrical symmetry for the nozzle flow studied. Rayleigh scattering measurements (Ref. 10) support this assertion and the previously mentioned inference that excessively high off-axis values of  $T_R$  are possibly a manifestation of condensation even though no condensation is observed along the centerline. Finally, the radial profiles of both the measured density and temperature (Figs. 47 through 50) show that significant deviations exist between the measured and MOC predicted values of density and temperature for off-axis points interior to the testing region. Using these results, the experimentally determined ratio of the unit length Reynolds number ( $Re_x$ ) and Mach number ( $M$ ) as a function of radial position for  $X_t/D_t = 12.47$  and 19.79 was found and is shown in Fig. 60. The application of similar measurements and flow field calibrations for larger flow-field simulation facilities is evident.

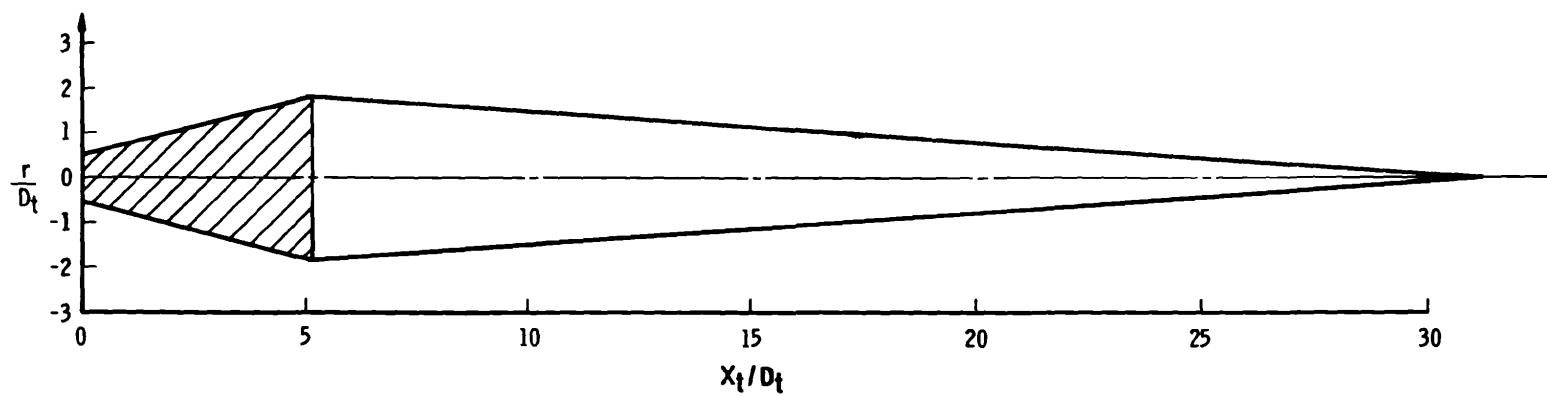


Figure 59. Two-dimensional axial-radial locus of the expansion characteristic.

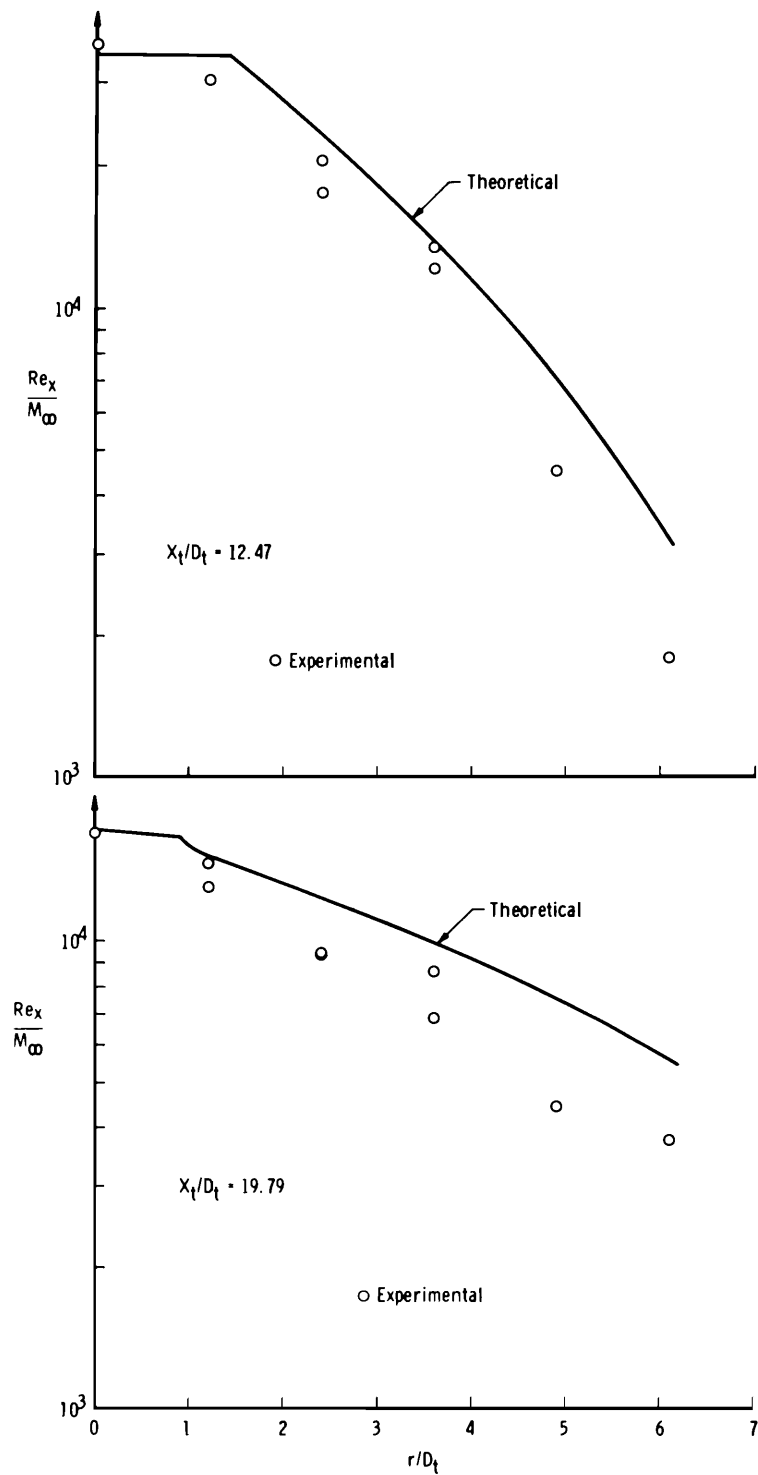


Figure 60. Ratio of the unit length Reynolds number ( $Re_x$ ) and Mach number ( $M$ ) as a function of radial position.



## 5.0 SUMMARY AND RECOMMENDATIONS FOR FUTURE WORK

### 5.1 REVIEW OF MEASUREMENTS

A summary of the experimental flow-field measurements is shown in Table 4. The measured values of the rotational temperature ranged from 300 to 11 K, and the range of gas number density at which the temperatures were measured was from  $2.54 \times 10^{19}$  to  $2.31 \times 10^{16}$  molecules/cc. At these respective number densities, the experimental uncertainty in  $T_R$  was  $\pm 2$  and  $\pm 20$  percent. Accurate measurements of the gas number density were performed over the number density range of from  $5.7 \times 10^{18}$  to  $6.0 \times 10^{16}$  molecules/cc, corresponding to approximately 190 to 2 torr, respectively, at 300 K.

Table 4. Summary of Measurements

Gas	Source	$P_{O'}$ atm	$T_{O'}$ K	X/D	$T_R$	N	r/D	$T_R$	N
N <sub>2</sub>	Sonic Orifice D = 1.325 mm	7.44	285	2.11 to 16.87	x				
		5.58	290	1.53 to 16.87	x				
		3.72	289	1.53 to 12.08	x				
		2.79	287	1.53 to 12.08	x				
O <sub>2</sub>		3.72	289	1.53 to 13.80	x				
CO	Conical Nozzle D <sub>t</sub> = 0.041 in.	3.72	289	1.53 to 8.24	x				
CO <sub>2</sub>		0.7	284	0.575 to 4.60	x				
N <sub>2</sub>		10.2	287	6.37 to 34.42	x	x	-3.66 to +6.10 X/D = 12.47	x	x
		6.80	286	6.37 to 34.42	x	x	-3.66 to +6.10 X/D = 19.19	x	x
		3.40	284	5.88 to 41.74	x	x			

These measurements are the first application at AEDC of Raman scattering diagnostics of supersonic and hypersonic flow-field temperatures and number density, and the first application of Raman diagnostics to a two-phase flow field. The quality of these results is indicative of the flow diagnostics capability of the Raman technique.

## 5.2 SYSTEMS IMPROVEMENTS

Optical system improvements can readily increase measurement accuracy and decrease the lowest density at which temperature measurements can be made. Figures 61a and b show two modifications which can be made to the present optical system. Figure 61a schematically shows a concave front surface mirror replacing the laser dump system and refocusing the expanding laser beam back to the original focal volume; i.e., a multiple-pass laser beam system. The spherical mirror must have a focal length half that of the laser focusing lens, and it must be placed a distance twice its focal length from the scattering or focal volume. Obviously the problem here will be the precise alignment of the concave mirror and will require precision translation of the mirror in three dimensions and tilting about the optical axis. Figure 61a also shows a concave front surface mirror replacing the viewing dump and placed in the same manner as the laser beam concave mirror. Thus a bilateral collection optics system is created, and precise alignment of the mirror is also required here. The beam double pass and bilateral collection optics can increase the scattered radiation detected by a factor of 4 (a conservative estimate), and by using a lower f/number collection optics system than the one used in these experiments, an additional factor of 4 improvement can be realized. Hence, by using the improvements shown in Fig. 61, scattered radiation detected can be increased by a factor of 16, which would decrease the imprecision of the measurements of these experiments by a factor of 4. Furthermore, while maintaining the precision of the present measurements the lower density limit could be decreased by a factor of 16 to  $1.76 \times 10^{15} \text{ cm}^{-3}$ . From another viewpoint, the measurements reported herein could have been made four times faster while maintaining the same precision.

Figure 61b shows a more difficult to achieve optical system improvement. By removing the laser output mirror and placing it beyond the flow field, as shown, the observed scattering volume is inside the laser cavity. This arrangement requires precise alignment and excellent stability of the mirror, but offers the possibility of a two order of magnitude increase in detected scattered radiation as shown by Hickman and Liang (Ref. 17). Another possible problem for this arrangement is the effect of flow-field gradients on the cavity stability. However, the arrangement of Fig. 61 offers a possible increase of a factor of 400 in the detected radiation which would decrease the measurement imprecision of these experiments by a factor of 20 and decrease the lower density limit by a factor of 400 to  $7.03 \times 10^{13} \text{ cm}^{-3}$ .

can be determined. However, for a mixture of such species as  $N_2$  and CO or  $CO_2$ , very high resolution will be necessary to separate the spectral lines. Since the centrifugal distortion constant of molecules such as  $N_2$ ,  $O_2$ , CO, and  $CO_2$  is very small, the separation of the rotational lines of a specie in terms of wave number is practically constant. Therefore, a Fabry-Perot interferometer may be used as the spectroscopic element, as shown in Fig. 61, to pass all the rotational lines of a given specie and reject the Rayleigh scattered radiation and the rotational lines of the other molecular species (Ref. 18). The total intensity of the passed lines can give the specie number density, and a small, moderate resolution, single spectrometer can spectrally analyze the output of the interferometer to give the rotational temperature of the specie.

Laboratory measurements of rotational temperatures and densities of single species at elevated temperatures ( $>300$  K) will be conducted, and the effects of both continuum and discrete background radiation in the spectral region of the pure rotational lines on the accuracy of the temperature and density measurements will be evaluated. These experiments will be extremely important in determining the feasibility of Raman scattering diagnostics for radiating flow fields and the low-density limits for high-temperature measurements. Flow-field measurements for reservoir temperatures up to 1200 K will also be made.

## REFERENCES

1. Williams, W. D., Hornkohl, J. O., and Lewis, J. W. L. "Electron Beam Probe for a Low Density Hypersonic Tunnel." AEDC-TR-71-61 (AD727004), July 1971.
2. Placzek, G. "The Rayleigh and Raman Scattering." Translated from a publication of the Akademische Verlags Gesellschaft G.m.b.H., Leipzig, 1934, Handbuch der Radiologie, Heft 6, Teil 2, pp. 209-374.
3. Placzek, G. and Teller, E. "Die Rotationsstruktur der Ramanbanden mehratomiger Molekule." Z. Phys., 31, 209, March 1933.
4. Sushchinskii, M. M. Raman Spectra of Molecules and Crystals. Israel Program for Scientific Translations, New York, 1972.
5. Anderson, A., Ed. The Raman Effect. Vol. 2, Marcel Dekker, Inc., New York, 1973.

6. Schwiesow, R. L. "Optimum Illumination Geometry for Laser Raman Spectroscopy." Journal of the Optical Society of America, Vol. 59, No. 10, October 1969, pp. 1285-1287.
7. Gerry, E. T. and Rose, D. J. "Plasma Diagnostics by Thomson Scattering of a Laser Beam." Journal of Applied Physics, Vol. 37, No. 7, June 1966, pp. 2715-2724.
8. Ashkenas, H. and Sherman, F. S. Rarefied Gas Dynamics, Edited by J. H. de Leeuw, Fourth Symposium, Vol. II, Academic Press, New York, N. Y., 1966, pp. 84-105.
9. Lewis, J. W. L., Williams, W. D., Price, L. L., and Powell, H. M. "Nitrogen Condensation in a Sonic Orifice Expansion Flow." AEDC-TR-74-36 (AD783254), July 1974.
10. Lewis, J. W. L., and Williams, W. D. "Profile of an Anisotropic Nitrogen Nozzle Expansion." AEDC-TR-74-114 (ADA004764), February 1975.
11. Beylich, A. E. "Experimental Investigation of Carbon Dioxide Jet Plumes." The Physics of Fluids, Vol. 14, No. 5, May 1971, pp. 898-905.
12. Lewis, J. W. L., Williams, W. D., and Powell, H. M. "Laser Diagnostics of a Condensing Binary Mixture Expansion Flow Field." Proceedings of Ninth International Rarefied Gas Dynamic Symposium, Edited by M. Becker and M. Fiebig, Vol. II, DFVLR Press, Porz Wahn, Germany, 1974, pp. F7.1-F7.8.
13. Hilsenrath, J., Beckett, C. W., Benedict, W. S., Fano, L., Hoge, H. J., Masi, J. F., Nuttall, R. L., Touloukian, J. S., and Woolley, H. W. Tables of Thermal Properties of Gases. NBS Circular 564, Washington, D. C., November 1955.
14. Honig, R. E. and Hook, H. O. "Vapor Pressure Data for Some Common Gases." RCA Review, Vol. XXI, No. 3, September 1960, p. 360.
15. Hirschfelder, J. O., Curtiss, C. F. and Bird, R. B. Molecular Theory of Gases and Liquids. John Wiley and Sons, New York, 1954.
16. Cottrell, T. L. and McCoubrey, J. C. Molecular Energy Transfer in Gases, Butterworths, London, 1961.

17. Hickman, R. L. and Liang, Louis. "Intra-Cavity Laser Raman Spectroscopy Using a Commercial Laser." Applied Spectroscopy, Nov/Dec 1973.
18. Barrett, J. J. and Myers, S. A. "A New Interferometric Method for Studying Periodic Spectra using a Fabry-Perot Interferometer." Journal of the Optical Society of America, Vol. 61, 1971, pp. 1246-1251.
19. Beers, Y. Introduction to the Theory of Error. Addison-Wesley Publishing Company, Inc., Reading, Massachusetts, 1953.

## APPENDIX A DETAILS OF TEMPERATURE DETERMINATION

Rotational temperatures are determined using Eq. (9) and measured rotational line relative intensity values. If we set

$$a = \ln C \quad (29)$$

$$x = J(J + 1) \quad (30)$$

$$b = \frac{B_o h c}{k T_R} \quad (31)$$

and

$$y = \ln \left\{ \frac{I_J^{\text{rel}} T_R}{\left[ \frac{\bar{\nu}_o - 4B_o(J + 3/2)}{\bar{\nu}_o} \right]^4 g_J \left[ \frac{3}{2} \frac{(J + 1)(J + 2)}{(2J + 3)} \right]} \right\} \quad (32)$$

Then Eq. (9) becomes

$$y = a + bx \quad (33)$$

For a least-squares fit of a straight line to the data,  $a$  and  $b$  must be chosen in such a way that the weighted sum of the squares of deviations of  $y$  from the desired straight line of best fit is a minimum (Ref. 19).

$$\delta y_K = y_K - (a + bx_K) \quad (34)$$

Let

$$W_1 \sigma_{y_1}^2 = W_2 \sigma_{y_2}^2 = \dots = W_K \sigma_{y_K}^2 = \sigma^2 \quad (35)$$

The  $W$ 's are the weighing factors, and  $\sigma$  denotes standard deviation. If  $\sigma^2 = 1$ , then

$$W_K = \frac{1}{\sigma_{y_K}^2} \quad (36)$$

Therefore, one must minimize

$$\sum_{K=1}^{K_{\max}} \left( \frac{\delta y_K}{\sigma_{y_K}} \right)^2 = \sum_{K=1}^{K_{\max}} W_K \delta y_K^2 \quad (37)$$

$$\delta y_K^2 = y_K^2 + a^2 + b^2 x_K^2 - 2ay_K + 2abx_K - 2bx_K y_K \quad (38)$$

$$\begin{aligned} \sum_{K=1}^{K_{\max}} W_K \delta y_K^2 &= \sum_{K=1}^{K_{\max}} W_K y_K^2 + a^2 \sum_{K=1}^{K_{\max}} W_K + b^2 \sum_{K=1}^{K_{\max}} W_K x_K^2 \\ &\quad - 2a \sum_{K=1}^{K_{\max}} W_K (y_K - bx_K) - 2b \sum_{K=1}^{K_{\max}} W_K x_K y_K \end{aligned} \quad (39)$$

$$\frac{\partial}{\partial a} \left( \sum_{K=1}^{K_{\max}} W_K \delta y_K^2 \right) = 2a \sum_{K=1}^{K_{\max}} W_K - 2 \sum_{K=1}^{K_{\max}} W_K y_K + 2b \sum_{K=1}^{K_{\max}} W_K x_K \stackrel{\text{SET}}{=} 0 \quad (40)$$

$$\frac{\partial}{\partial b} \left( \sum_{K=1}^{K_{\max}} W_K \delta y_K^2 \right) = 2b \sum_{K=1}^{K_{\max}} W_K x_K^2 + 2a \sum_{K=1}^{K_{\max}} W_K x_K - 2 \sum_{K=1}^{K_{\max}} W_K x_K y_K \stackrel{\text{SET}}{=} 0 \quad (41)$$

$$a = \frac{\sum_{K=1}^{K_{\max}} W_K y_K \sum_{K=1}^{K_{\max}} W_K x_K^2 - \sum_{K=1}^{K_{\max}} W_K x_K \sum_{K=1}^{K_{\max}} W_K x_K y_K}{\sum_{K=1}^{K_{\max}} W_K \sum_{K=1}^{K_{\max}} W_K x_K^2 - \left( \sum_{K=1}^{K_{\max}} W_K x_K \right)^2} \quad (42)$$

$$b = \frac{\sum_{K=1}^{K_{\max}} W_K \sum_{K=1}^{K_{\max}} W_K x_K y_K - \sum_{K=1}^{K_{\max}} W_K x_K \sum_{K=1}^{K_{\max}} W_K y_K}{\sum_{K=1}^{K_{\max}} W_K \sum_{K=1}^{K_{\max}} W_K x_K^2 - \left( \sum_{K=1}^{K_{\max}} W_K x_K \right)^2} \quad (43)$$

Let

$$y_K = \ell_n(\mathbf{I}_K^{\text{ref}})_o$$

From Beer's

$$\sigma_{y_K} = \frac{\sigma(I_K^{rel})_o}{(I_K^{rel})_o} = S_{I_R} \equiv \text{fractional standard deviation} \quad (44)$$

$$\sigma(I_K^{rel})_o = \left[ (I_K^{rel})_o \right]^{1/2} \quad (45)$$

$$S_{I_R} = \left[ (I_K^{rel})_o \right]^{-1/2} \quad (46)$$

Then

$$\sigma_{y_K} = \left[ (I_K^{rel})_o \right]^{-1/2} \quad (47)$$

and results in

$$W_K = (I_K^{rel})_o \quad (48)$$

Let  $S_y$  be defined as the standard deviation of  $y$  about the line.

From Beer's

$$S_y = \left[ \frac{\sum_{K=1}^{K_{max}} \delta y_K^2}{K_{max} - 2} \right]^{1/2} \quad (49)$$

For

$$T_R = \frac{-hcB/k}{b} \quad (50)$$

$$dT_R = \frac{hcB/k}{b^2} db \quad (51)$$

Therefore,

$$S_{T_R} = \frac{hcB/k}{b^2} S_b \quad (52)$$



$$S_b = S_y \left[ \sum_{i=1}^{K_{\max}} \left( \frac{\partial b}{\partial y_i} \right)^2 \right]^{\frac{1}{2}} \quad (53)$$

$$\frac{\partial b}{\partial y_i} = \frac{\sum_{K=1}^{K_{\max}} w_K (w_i x_i) - \sum_{K=1}^{K_{\max}} w_K x_K (w_i)}{\sum_{K=1}^{K_{\max}} w_K \sum_{K=1}^{K_{\max}} w_K x_K^2 - \left( \sum_{K=1}^{K_{\max}} w_K x_K \right)^2} \quad (54)$$

$$\left( \frac{\partial b}{\partial y_i} \right)^2 = \frac{\left( \sum_{K=1}^{K_{\max}} w_K \right)^2 (w_i x_i)^2 - 2 \sum_{K=1}^{K_{\max}} w_K \sum_{K=1}^{K_{\max}} w_K x_K \sum_{K=1}^{K_{\max}} w_K^2 x_K + \left( \sum_{K=1}^{K_{\max}} w_K x_K \right)^2 w_i^2}{\left[ \sum_{K=1}^{K_{\max}} w_K \sum_{K=1}^{K_{\max}} w_K x_K^2 - \left( \sum_{K=1}^{K_{\max}} w_K x_K \right)^2 \right]^2} \quad (55)$$

$$\sum_{i=1}^{K_{\max}} \left( \frac{\partial b}{\partial y_i} \right)^2 = \frac{\left( \sum_{K=1}^{K_{\max}} w_K \right)^2 \sum_{K=1}^{K_{\max}} (w_K x_K)^2 - 2 \sum_{K=1}^{K_{\max}} w_K \left( \sum_{K=1}^{K_{\max}} w_K x_K \right) \sum_{K=1}^{K_{\max}} w_K^2 x_K + \left( \sum_{K=1}^{K_{\max}} w_K x_K \right)^2 \sum_{K=1}^{K_{\max}} w_K^2}{\left[ \sum_{K=1}^{K_{\max}} w_K \sum_{K=1}^{K_{\max}} w_K x_K^2 - \left( \sum_{K=1}^{K_{\max}} w_K x_K \right)^2 \right]^2} \quad (56)$$

Then

$$S_b = S_y \left[ \frac{\left( \sum_{K=1}^{K_{\max}} w_K \right)^2 \sum_{K=1}^{K_{\max}} (w_K x_K)^2 - 2 \sum_{K=1}^{K_{\max}} w_K \left( \sum_{K=1}^{K_{\max}} w_K x_K \right) \sum_{K=1}^{K_{\max}} w_K^2 x_K + \left( \sum_{K=1}^{K_{\max}} w_K x_K \right)^2 \sum_{K=1}^{K_{\max}} w_K^2}{\sum_{K=1}^{K_{\max}} w_K \sum_{K=1}^{K_{\max}} w_K x_K^2 - \left( \sum_{K=1}^{K_{\max}} w_K x_K \right)^2} \right]^{1/2} \quad (57)$$

As stated previously, Eq. (9) is solved by iterative machine calculation using Eqs. (30), (31), (32), (42), (43), and (48). The iteration process continues to calculate a temperature until consecutive calculated values are within 0.01 percent.

A temperature defined by the maximum number of spectral lines is first calculated. Then a temperature value for  $K_{\max} - 1$  lines is calculated. This process is repeated  $i$  times through  $K_{\max} - i = 2, i = 0, 1, 2, \dots$ . However, no more than 12 iterations for each  $(K_{\max} - i)$  number of lines is allowed.

The standard deviation of the temperature ( $S_{T_R}$ ) is computed for each  $(K_{\max} - i)$  number of lines. This value is computed using Eqs. (49), (52), and (57).

For a given flow condition and flow-field position, more than one spectral scan may be taken. Therefore, it is necessary to "average" these data by some process. A portion of PROGRAM RATROT calculates an average  $T_R/T_O$ ,  $\bar{T}_R/T_O$ , and an average standard deviation ( $\bar{\sigma}_{T_R}$ ) for a given number of spectral lines used in calculating a  $T_R$  in a fixed set of data. The  $\bar{T}_R/T_O$  and  $\bar{\sigma}_{T_R}$  values are weighted according to their own precision.

$$\left(\frac{\bar{T}_R}{T_O}\right)_K \equiv \bar{y}_K = \left(\sum_{j=1}^s \frac{y_j}{\sigma_j^2}\right) / \sum_{j=1}^s \left(\frac{1}{\sigma_j^2}\right) \quad (58)$$

by definition of a weighted average (Ref. 19).

$$\sigma_j \equiv (S_{T_R})_j / (T_O)_j \quad (59)$$

$$y_j \equiv (T_R)_j / (T_O)_j \quad (60)$$

s = the total number of data points to be used, usually the number of spectral scans for a given condition

$$(\bar{\sigma}_{T_R})_K = \left[ \sum_{j=1}^s (W_j \sigma_j)^2 / \left( \sum_{j=1}^s W_j \right)^2 \right]^{1/2} \quad (61)$$

by definition of a standard deviation of an average (Ref. 16),

$$W_j = \left(\frac{\sigma_1}{\sigma_j}\right)^2 \quad (62)$$

For a given number of scans (s) for a particular flow condition and position, PROGRAM RATROT has computed  $(\bar{T}_R/T_O)_K$  and  $(\bar{\sigma}_{T_R})_K$  for each number of spectral lines used. To avoid the decision as to which particular  $(\bar{T}_R/T_O)_K$  is the best to use, PROGRAM RATROT performs another weighted average calculation to determine  $\bar{T}_R$  and  $\bar{\sigma}_{T_R}$ .

$$\bar{T}_R = T_O \left[ \frac{\sum_{K=2}^{K_{\max}} \left(\frac{\bar{T}_R}{T_O}\right)_K}{\sum_{K=2}^{K_{\max}} (\bar{\sigma}_{T_R})_K^2} / \frac{1}{\sum_{K=2}^{K_{\max}} (\bar{\sigma}_{T_R})_K^2} \right] \quad (63)$$

and

$$\bar{S}_{T_R} = 2T_o \left\{ \sum_{K=2}^{K_{max}} \left[ W'_K (\bar{\sigma}_{T_R})_K \right]^2 \left[ \sum_{K=2}^{K_{max}} W'_K \right]^2 \right\}^{1/2} \quad (64)$$

where

$$W'_K = \left[ \frac{(\bar{\sigma}_{T_R})_{K_{max}}}{(\bar{\sigma}_{T_R})_K} \right]^2 \quad (65)$$

## APPENDIX B

### OPTIMUM ILLUMINATION GEOMETRY FOR RAMAN SCATTERING MEASUREMENTS

For the determination of the optimum illumination geometry for the laser-Raman technique for flow fields, the general treatment of this subject by Schwiesow (Ref. 6) will be used.

Assume the laser beam to be plane-parallel of wave number  $\bar{\nu}_0 = 1/\lambda_0$  and diameter  $D_L$ . A diffraction limited lens of focal length  $F_L$  focuses the laser beam in the flow field. An axially symmetric irradiance distribution will exist at the focus, and approximately 80 percent of the total power in the incident beam will be contained in a cylinder of diameter

$$d' = (2/\bar{\nu}_0)(F_L/D_L) \quad (66)$$

and length

$$\ell' = (14/\bar{\nu}_0)(F_L/D_L)^2 \quad (67)$$

The relative intensity of the laser beam at the focus is

$$I_o^{rel} = \frac{I_o'}{I_o} = \frac{\bar{\nu}_0^2 D_L^2}{4} \left( \frac{D_L}{F_L} \right)^2 \quad (68)$$

The relative number of scattered photons collected per unit time is

$$R_s = \sigma_R I_o^{rel} N_g V \Omega' \quad (69)$$

This can be rewritten as

$$R_s = \sigma_R \frac{\bar{\nu}_0^2 D_L^2}{4} \left( \frac{D_L}{F_L} \right)^2 N_g V \Omega' \quad (70)$$

The sample volume (cylinder of diameter  $d'$  and length  $\ell'$ ) is imaged onto the defining slit of the spectrometer by the collecting optics. If the collection optics have linear magnification ( $M$ ), the sample volume at the slit will have dimensions ( $d = Md'$ ,  $\ell = M\ell'$ ) with the inherent acceptance angle of the spectrometer enlarged from  $\Omega$  to  $\Omega' = M^2\Omega$  at

the scattering volume. For a slit of width  $w$  and height  $h$ , the volume of the imaged cylinder is approximately that of a rectangular prism  $d$  deep, the lesser of  $d$  and  $w$  wide, and the lesser of  $\ell$  and  $h$  high.

For cases in which  $h/w > \ell/d$  over the possible range of  $F_L/D_L$  values (the narrow slit case), the function  $R_s$  is considered over three regions:

$$(1) \quad d < w, \ell < h$$

$$(2) \quad w < d, \ell < h$$

$$(3) \quad w < d, h < \ell$$

$$R_{s_1} = \sigma_R \frac{\bar{\nu}_o^2 D_L^2}{4} N_g \left[ 56 \left( \frac{F_L}{D_L} \right)^2 \frac{M^3 \Omega}{\bar{\nu}_o^3} \right] \quad (71)$$

$$R_{s_2} = \sigma_R \frac{\bar{\nu}_o^2 D_L^2}{4} N_g \left[ 28 \left( \frac{F_L}{D_L} \right)^2 \frac{M^2 \Omega}{\bar{\nu}_o^2} \right] \quad (72)$$

$$R_{s_3} = \sigma_R \frac{\bar{\nu}_o^2 D_L^2}{4} N_g \left[ 2 \left( \frac{F_L}{D_L} \right)^{-1} \frac{M w h \Omega}{\bar{\nu}_o} \right] \quad (73)$$

From Eqs. (71), (72), and (73), it is observed that the maximum value of  $R_s$  occurs at the boundary between region 2 and region 3 where  $\ell = h = M\ell'$ . At this point, the optimum  $F_L/D_L$  is

$$\left( \frac{F_L}{D_L} \right)_{\text{opt}} = \left[ \frac{\bar{\nu}_o h}{14M} \right]^{1/2} \quad (74)$$

For a wide slit case,  $\ell/d > h/w$ , the three regions become

$$(1) \quad d < w, \ell < h$$

$$(2) \quad d < w, h < \ell$$

$$(3) \quad w < d, h < \ell$$

Regions 1 and 3 of the wide slit case are identical to regions 1 and 3 of the narrow slit case. In region 2,

$$R_{s_2} = \sigma_R \frac{\bar{\nu}_o^2 D_L^2}{4} N_g \left[ \frac{4}{\bar{\nu}_o^2} M^2 h \Omega \right] \quad (75)$$

which is independent of  $F_L/D_L$ . Hence, the optimum values of  $F_L/D_L$  may be anywhere within the range defined by the boundary of region 2 with region 1 where  $h = \ell = M\ell'$  and the boundary of region 2 with region 3 where  $w = d = Md'$ .

$$\left[ \frac{\bar{\nu}_o h}{14M} \right]^{1/2} \leq \left( \frac{F_L}{D_L} \right)_{opt} \leq \frac{\bar{\nu}_o w}{2M} \quad (76)$$

With a truncated Gaussian laser beam and  $D_L$  defined by the  $1/e^2$  points, 2 changes to 2.4 and 14 changes to 16 in Eqs. (74) and (76).

For the laboratory system,

$$\frac{F_L}{D_L} = 178.6$$

and

$$24.6 \leq \left( \frac{F_L}{D_L} \right)_{opt} \leq 194.4$$

for nominal 200  $\mu\text{m}$  by 5 mm slits. The diameter of the scattering volume was 220.5  $\mu\text{m}$ . For the 4 by 10 Research Chamber,

$$\frac{F_L}{D_L} = 25.5$$

and

$$17.4 \leq \left( \frac{F_L}{D_L} \right)_{opt} \leq 97.2$$

for nominal 200  $\mu\text{m}$  by 5 mm slits. The diameter of the scattering volume was 31.5  $\mu\text{m}$  with a length of 5.35 cm.

## NOMENCLATURE

$a$	Nucleon number of the atomic constituent
$B_0$	Rotational constant of the ground vibrational level
$b$	Defined by Eq. (31) as the slope of the rotational Boltzmann plot
$C$	A constant defined by Eq. (5)
$C_F$	A calibration factor for number density measurement and defined by Eq. (12)
$C_{RR}$	A constant as defined in Eq. (2)
$c$	Speed of light in vacuum
$D$	Sonic orifice diameter
$D_L$	Diameter of laser beam before focusing
$D_t$	Throat diameter of conical nozzle
$d', d$	Diameter of the scattering volume and the diameter of the scattering volume as imaged on the spectrometer slit, respectively
$F_L$	Focal length of the laser beam focusing lens
$g_J$	Nuclear spin statistics weighting factor
$h, \hbar$	Planck's constant or spectrometer slit height; $\hbar = h/2\pi$
$I_A, I_B$	Nuclear spins for species A and B, respectively
$I_J, I_J^{rel}$	Absolute and relative intensity (photons/sec) of a pure rotational Raman line
$I_M$	Collision number integrand
$I_0, I'_0$	Laser beam intensity (photons/sec-cm <sup>2</sup> ) before and after focus, respectively
$I_T, I_T^{rel}$	Absolute total and relative total intensity of the rotational Raman Stokes' band
$J$	Rotational quantum number
$K, K_{max}$	A summation index (1, 2, 3, . . .) indicating the rotational spectral line number and the maximum number of spectral lines used in a rotational temperature determination, respectively

$k$	Boltzmann's constant
$l', l$	Length of the scattering volume and the length of the scattering volume as imaged on the spectrometer slit, respectively
$M$	Magnification of the collection optics system or Mach number
MOC	Method of characteristics
$N, N_g, N_c$	Molecular species number density, $\text{cm}^{-3}$
$N_o$	Reservoir gas number density, $\text{cm}^{-3}$
$o$	Ortho modification
$\bar{P}$	Electronic parity eigenvalue
$P_o, P$	Reservoir pressure and gas static pressure, respectively
$p$	Para modification
$p_v(12)$	Probability of transfer of a vibrational quantum between $(X/D)_1$ and $(X/D)_2$
$q_r$	Molecular rotational partition function
$q_r^{QM}, q_r^{Cl}$	Quantum mechanical and classical molecular rotational partition function, respectively
$Re_x$	Unit length Reynolds number
$R_s$	Relative number of scattered photons collected per unit time
$r/D_t$	Nondimensional radial distance from flow centerline
$S_{IR}$	Fractional standard deviation of the relative intensity of a spectral line
$S_J$	Rotational Raman line strength factor
$ST_R, \bar{S}T_R$	Standard deviation of the determined rotational temperature as defined by Eq. (52) and average standard deviation of the determined rotational temperature as defined by Eq. (64), respectively
$S_b$	Standard deviation of the slope of the straight line fitted to the data
$S_y$	Standard deviation of the data about the fitted straight line



$T, T_c$	Molecular species temperature, K
$T_o$	Reservoir gas temperature, K
$T_R, \bar{T}_R$	Rotational temperature and average rotational temperature as defined by Eq. (63), respectively
$T_r(J)$	Sensitivity factor of optics, spectrometer, and detector
$T_s$	Static temperature at saturation
$V$	Scattering volume
$W_j$	A weighting factor as defined by Eq. (62)
$W_K$	Rotational line intensity weighting factor
$W'_K$	A weighting factor as defined by Eq. (65)
$w$	Spectrometer slit width
$X/D, X_t/D_t$	Nondimensional axial distance from sonic orifice and conical nozzle throat, respectively
$(X/D)_s$	Axial location of saturation
$x$	$J(J + 1)$
$y, y_k$	Defined by Eq. (32)
$y_j$	Defined by Eq. (60)
$\bar{y}_k$	Defined by Eq. (58)
$Z_{10}$	Number of collisions required for transfer of one vibrational quantum from vibrational level 1 to level 0
$Z_T(12)$	Average total number of collisions which a molecule experiences between $(X/D)_1$ and $(X/D)_2$
$\bar{Z}_T(12)$	Accumulative collision number function
$\gamma$	Ratio of specific heats
$\Delta E_v(12)$	Vibrational energy of CO <sub>2</sub> transferred to the translational and rotational modes between $(X/D)_1$ and $(X/D)_2$
$\theta_R$	Characteristic rotational temperature
$\lambda_J$	Wavelength of rotational Raman line
$\nu_o$	Laser line frequency
$\bar{\nu}_o$	Laser line wave number

$\rho, \rho_0$	Gas density and reservoir gas density, respectively
$\sigma$	Hard sphere collision cross section
$\sigma(I_K^{\text{rel}})$	Standard deviation of the relative intensity of a rotational Raman line
$\sigma_j$	Defined by Eq. (59)
$\sigma_R$	Total rotational Raman scattering cross section
$\sigma_{RR_J}$	Rotational Raman line cross section, $\text{cm}^2/\text{ster}$
$(\overline{\sigma}T_R)_K$	Standard deviation of the average $T_R$ determined using $K$ spectral lines
$\tau$	Time
$\Omega', \Omega$	Collection optics solid angle and spectrometer solid angle, respectively
$\omega$	Vibrational frequency of $\text{CO}_2$